



## 저작자표시-비영리-동일조건변경허락 2.0 대한민국

이용자는 아래의 조건을 따르는 경우에 한하여 자유롭게

- 이 저작물을 복제, 배포, 전송, 전시, 공연 및 방송할 수 있습니다.
- 이차적 저작물을 작성할 수 있습니다.

다음과 같은 조건을 따라야 합니다:



저작자표시. 귀하는 원저작자를 표시하여야 합니다.



비영리. 귀하는 이 저작물을 영리 목적으로 이용할 수 없습니다.



동일조건변경허락. 귀하가 이 저작물을 개작, 변형 또는 가공했을 경우에는, 이 저작물과 동일한 이용허락조건하에서만 배포할 수 있습니다.

- 귀하는, 이 저작물의 재이용이나 배포의 경우, 이 저작물에 적용된 이용허락조건을 명확하게 나타내어야 합니다.
- 저작권자로부터 별도의 허가를 받으면 이러한 조건들은 적용되지 않습니다.

저작권법에 따른 이용자의 권리는 위의 내용에 의하여 영향을 받지 않습니다.

이것은 [이용허락규약\(Legal Code\)](#)을 이해하기 쉽게 요약한 것입니다.

[Disclaimer](#)

공학박사 학위논문

**Dynamic Interaction between  
Patterned Vortex-State  
Ferromagnetic Structures**

패터닝된 자기 소용돌이 형태의  
강자성 구조 간의 동적 상호 작용

2012 년 8 월

서울대학교 대학원

공과 대학 재료공학부

정 현 성



**Dynamic Interaction between  
Patterned Vortex-State  
Ferromagnetic Structures**

**A THESIS  
SUBMITTED TO THE FACULTY OF SEOUL  
NATIONAL UNIVERSITY  
BY**

**Hyunsung Jung**

Supervised by  
**Prof. Sang-Koog Kim**

**IN PARTIAL FULFILLMENT OF THE  
REQUIREMENTS FOR THE DEGREE OF  
DOCTOR OF PHILOSOPHY**

**August 2012**

*Department of Materials Science and Engineering  
Graduate School  
Seoul National University*

# **Abstract**

In a sub-micrometer-size patterned ferromagnetic structure, the magnetic vortex is in a strongly stable ground state characterized by an in-plane curling magnetization around and an out-of-plane magnetization in the central region. In isolated disks, applied external forces induce vortex excitations, among which a translational mode exists in which the vortex core rotates around its equilibrium position at a characteristic eigenfrequency.

This work focused on dynamic interaction between vortex-state ferromagnetic structures, utilizing micromagnetic simulations, analytical calculations, and experiments. Coupled vortex-core gyration in separated disks was observed by employing time and space resolved full-field magnetic transmission soft x-ray microscopy. We found that the vortex gyration of one disk affects that of the other through their respective dynamically rotating stray fields.

In addition, energy/signal transfer based on the transfer mechanism having been provided, the details including the fundamentals of the dynamic interaction between magnetic vortices were investigated. This robust mechanism for energy transfer offers the advantages of a fast and tunable transfer rate, which is a function of disk interdistance and interaction strength. The energy loss during gyration-mediated signal transfer is reduced by using magnetic material that has a low damping constant.

Based on a fundamental understanding of that dynamic interaction, a logic operation using vortex gyration was demonstrated. Remarkably, the excitation of vortex gyrations and signal transfer between neighboring disks were as fast as a few ns.

This work provides a fruitful fundamental understanding of dynamic interaction between magnetic vortices and a robust means of information-signal transport between physically separated magnetic disks.

**Keywords: Magnetic vortex, Dynamic interaction, Energy transfer, Spin dynamics, Gyrotropic motion, Translational mode**

**Student number:** 2002-12440

## 국문초록

자기 소용돌이는 마이크로미터 이하의 패터닝된 강자성 구조체에서 안정한 자화 구조로 박막 면에 평행하며 소용돌이와 같은 형태로 배열된 수평 자화 성분과 구조체 중심부에 박막 면에 수직한 방향의 자화 성분(소용돌이 핵)으로 이루어져 있다. 독립된 원판형 박막에서, 외부의 힘이 인가되면 소용돌이 핵이 평형상태의 위치를 중심으로 특정 주파수로 회전하는 자기 소용돌이의 움직임이 여기 된다.

본 학위 논문에서는 자기 소용돌이 상태의 강자성 구조체 간의 동적 상호작용을 미소자기 전산모사, 이론 계산, 실험을 통해 살펴보았다. 물리적으로 분리된 원판형 박막 사이에서 자기 소용돌이 중심의 결합 거동을 시공간 분해 자기 투과 연 X-선 현미경을 이용해 관찰하였다. 하나의 원판에서의 자기소용돌이 회전운동에 의해 회전 표유 자계가 형성되어 다른 원판에 영향을 끼침을 밝혀냈다.

더불어 그와 같은 상호 작용을 바탕으로 에너지/신호 전달 방법을 제안하였고 동적 상호작용의 물리적 원인을 탐사하였다. 이 메커니즘은 빠르고 조절 가능한 에너지 전달을 가능하게 한다. 원판간의 거리 및 상호작용 세기에 따라 에너지 전달 속도의 조절이 가능하며 낮은 자기 감쇠 상수를 갖는 물질을 사용함으로써 신호 전달 시의 에너지 손실을 줄일 수 있다.

또한 동적 상호작용에 대한 근본적 이해를 바탕으로 자기 소용돌이 회전운동을 이용한 논리 연산을 제시, 구현하였다. 인접한 원판 간의 자기 소용돌이의 회전운동에 의한 정보는 수 나노초 이하의 빠른 시간에 전달된다.

본 학위 논문은 자기 소용돌이 간의 동적 상호 작용에 대한 기초적인 이해와 원판형 자성 박막 간의 통제 가능한 정보 전달 및 처리 방법을 제공한다.

# Contents

Abstract.....	i
List of Tables .....	viii
List of Figures.....	ix
<b>1. Introduction .....</b>	<b>1</b>
<b>2. Research Background .....</b>	<b>8</b>
2.1 Micromagnetics.....	8
2.2 Translational mode of magnetic vortex.....	13
2.3 Interaction between mangnetic vortices.....	15
<b>3. Sample Design and Fabrication .....</b>	<b>19</b>
3.1 Thin film deposition.....	20
3.2 Lithography.....	25
3.3 Magnetic field strength and distribution .....	28

<b>4. Magnetic Imaging using Transmission Soft X-ray Microscopy .</b>	<b>30</b>
4.1 Magnetic imaging techniques .....	31
4.2 X-ray magnetic circular dichroism .....	35
4.3 Full-field magnetic transmission soft x-ray microscopy (MTXM)....	38
4.4 Time resolved imaging using pump and probe technique.....	41
 <b>5. Coupled Vortex Cores Oscillation .....</b>	 <b>43</b>
5.1 Sample preparation and experimental setup .....	45
5.2 Imaging of vortex core oscillation .....	48
5.3 Dipolar induced vortex core oscillation .....	53
 <b>6. Energy Transfer through Vortex Core Gyration .....</b>	 <b>56</b>
6.1 Coupled oscillator .....	57
6.2 Experimental observation of dipolar induced vortex gyrations .....	61
6.3 Energy transfer between two dipolar-coupled vortex oscillators .....	68
6.4 Normal modes representation of coupled vortex oscillations .....	74
6.5 Micromagnetic simulation procedure and results .....	79
6.6 Frequency splitting and energy transfer rate .....	82
6.7 Dependence on interdistance .....	83
6.8 Dependence on relative vortex polarization.....	86

6.9 Energy attenuation .....	89
6.10 Propagation of gyration in longer chain.....	92
<b>7. Logic Operation using Vortex State Structures .....</b>	<b>96</b>
7.1 Design of archetypal XOR logic by simulations .....	98
7.2 Experimental verification using soft X-ray microscopy .....	105
7.3 Differential XMCD images of individual disks' vortex gyrations ...	109
7.4 Programmable logic operations .....	114
7.5 Limitation.....	118
<b>8. Summary .....</b>	<b>122</b>

Bibliography

Publication List

Patent List

Presentations in Conferences



## **List of Tables**

6.1 Dependence of exchange time and attenuation on variables.....	91
7.1 Truth table for possible logical inputs and resultant outputs.....	116

# List of Figures

1.1 Examples of spintronic devices.....	5
1.2 Magnetic vortex configuration in variable confined structures.....	6
1.3 Schematic illustration of the translational mode .....	7
2.1 Schematic representation of the precession of magnetization.....	12
2.2 Collective mode in two coupled disks.....	18
3.1 A clustering deposition system.....	22
3.2 Low angle X-ray diffraction for Py thin film. ....	23
3.3 Hysteresis loops of Py measured by the longitudinal configurations.....	24
3.4 E-beam lithography processes.....	27
3.5 Microscopy images of patterned structures.....	27
3.6 Schematic geometry for the magnetic field calculation. ....	29
3.7 Spatial distribution of the magnitude of magnetic fields .....	29
4.1 Magnetic vortex core observed by magnetic force microscopy .....	33
4.2 Magnetic domain nucleation and growth observed by Kerr microscopy ..	34
4.3 Illustration of X-ray magnetic circular dichroism (XMCD) .....	37
4.4 Magnetic X-ray transmission microscopy (MTXM).....	40
4.5 Schematic illustrations of optical setup.....	40
4.6 Pump-and-probe setup.....	42
5.1 Schematic illustration and chemical contrast of sample .....	47
5.2 XMCD images of dynamic evolution of vortex gyrotropic motions .....	50

5.3 Spatial distribution of the magnitude of magnetic fields generated from the Cu stripline .....	51
5.4 Distribution of stray field emitted from a Py disk during gyration .....	52
5.5 Oscillations of the $x$ and $y$ components of both vortex-core positions as function of time .....	55
6.1 A system of coupled mass oscillators in one dimension.....	59
6.2 Energy transfer between 1D two coupled harmonic oscillators. ....	60
6.3 Sample geometry of pairs of two vortex-state disks and initial states .....	63
6.4 XMCD images and simulation results on the vortex gyrations in the two disks in both pairs: $d_{\text{int}}/(2R) = 1.05$ .....	66
6.5 XMCD images and simulation results on the vortex gyrations in the two disks in both pairs: $d_{\text{int}}/(2R) = 1.10$ .....	67
6.6 Comparison of vortex-core displacement variations versus time in both disks for $d_{\text{int}}/(2R) = 1.05$ and $1.10$ . ....	69
6.7 Normal-mode representations of vortex-core gyrations in dipolar-coupled oscillators for $d_{\text{int}}/(2R) = 1.05$ . ....	77
6.8 Normal-mode representation of vortex-core gyrations in a real sample of $d_{\text{int}}/(2R) = 1.10$ . ....	78
6.9 Simulation results of vortex gyrations in dipolar-coupled vortex-state disks during the free relaxation. ....	81
6.10 Dependence on interdistance.....	84
6.11 Frequency splitting and exchange time .....	85

6.12 Comparisons of different polarization configuration.....	87
6.13 vortex-core displacements versus time for Py and NiMnSb .....	90
6.14 Propagation of stimulated vortex gyrations in 1D disk arrays .....	94
7.1 Model geometry of three Py disks.....	101
7.2 Vortex core gyration and stray field distribution under different inputs .	104
7.3 Schematic layout and XMCD contrast of sample. ....	108
7.4 Differential images obtained from calculation.....	111
7.5 Differential images for different inputs.....	112
7.6 Serial differential images for different inputs. ....	113
7.7 Vortex core gyration and stray field distribution in assymmetric polarization configuration .....	117
7.8 Dependence on phase delay of inputs .....	120

# **Chapter 1**

## **Introduction**

Patterned ferromagnetic structures are an integral part of the development of spintronics and nanomagnetism as candidates for future non-volatile memory and information devices [1-5]. In a broad sense spintronics includes electronic devices that use the magnetic properties of materials such as the magneto-resistive head in hard disk drives, magnetic random-access memory, proposed domain wall storage devices [6, 7], and the spin-torque-oscillator [8, 9], as shown in Fig 1.1. Recently, signal processing using magneto-resistive devices has been intensively studied for its low dissipation and nonvolatility. A significant number of logic circuits based on magneto-resistive devices have been proposed and demonstrated [10-15]. However, these devices had a common disadvantage in that additional electronic devices are needed for intermediate circuitry. In this study, novel conceptual information processing without intermediate circuitry, which is to say, information processing that utilizes vortex-state magnetic disk networks, is proposed.

In some confined ferromagnetic structures, especially low-anisotropy soft magnets such as Ni, Fe, and its alloy, in order to reduce magneto-static energy, an intriguing domain configuration called the magnetic vortex is formed, as illustrated in Fig. 1.2. In the configuration, the

magnetization has a direction parallel to the side of the structure (in the tangential direction in the circular cylinder) in the vicinity of the side surface, and an out-of plane component near the center (vortex core) of the structure. This magnetic vortex structure has aroused intensive interest due to its singularity and high stability. Recently, the development of a technique for *nano*-scale imaging and highly sensitive measurement has made possible the observation of the nanometer-size vortex core [16, 17] and its dynamic properties [18-21]. The magnetization direction of the vortex core (polarization,  $p$ ) can be either up ( $p=1$ ) or down ( $p=-1$ ). The rotation direction of the in-plane magnetization components (chirality,  $C$ ) can be either counterclockwise( $C=1$ ) or clockwise( $C=-1$ ). Each magnetization state in a single disk is energetically degenerated at its ground state. This multistability of magnetic vortices as well as the switching from one state to the other has been intensively studied over the past decade due to their promising applications in, for example, storage and memory devices [17, 20, 22-26] .

In isolated disks, applied magnetic fields or spin-polarized currents induce vortex excitations, among which a translational mode[27-32] exists in which the vortex core rotates around its equilibrium position at a characteristic eigenfrequency [27] ( $\nu_0 = \omega_0/2\pi$ ) typically ranging from several hundred MHz to ~1 GHz. The frequency is linearly proportional to the dot aspect ratio [27], and the rotation sense of the vortex gyration is

determined by the polarization  $p$  [19, 27], where  $p = +1$  ( $-1$ ) corresponds to the upward (downward) orientation of the magnetizations in the core as shown in Fig 1.3. Vortex-core oscillations have been intensively studied for their promising applications as microwave emission sources [27, 31-41].

Most studies have focused on the dynamics of isolated single disks [33, 38-40]. However, the needs for high-power signals and high packing density have spurred further studies, not only on coupled vortex-state disks but also on multiple-disk arrays. In a stable state of magnetic vortex, the interaction between disks can be negligible due to its in-plane-curling magnetization. On the other hand, when the vortex moves from the disk center by external force, the interaction becomes stronger, owing to uncompensated magnetic charges formed on the side surface of the disk. In cases of sufficiently short distances between nearest neighbouring disks, the interaction can alter the dynamics of magnetic vortices [42]. Therefore, complete understanding of the dynamic interaction between magnetic vortices is important to the realization of promised spintronic devices as well as for fundamental interest.

In this thesis, the dynamic interaction between magnetic vortices was investigated utilizing micromagnetic simulation, analytical calculation, and time-resolved observation. A new robust mechanism using resonant vortex gyration was derived for tunable energy transfer and information-signal transport between physically separated magnetic disks. Information

processing based on the mechanism also was investigated and demonstrated. In Chapter 2, the theoretical background and related work are reviewed. In Chapter 3, sample design and fabrication methods are presented. In Chapter 4, the details of the magnetic imaging technique using X-ray microscopy and the observed static properties of the vortex-state disk are discussed. In Chapter 5, data on time- and space-resolved observation of the translational motion of coupled vortices is presented. In Chapter 6, on the basis of the results and an analogy of a coupled oscillator system, energy transfer represented by vortex core gyration is proposed and demonstrated. Additionally, the relation between the eigenmode of the system and the energy transfer is discussed. In Chapter 7, on the principle that vortex gyrations are resonantly excited through coupling between neighboring vortex-state disks, a logic operation using vortex-state disk networks is demonstrated. Finally, Chapter 8 summarizes the findings.



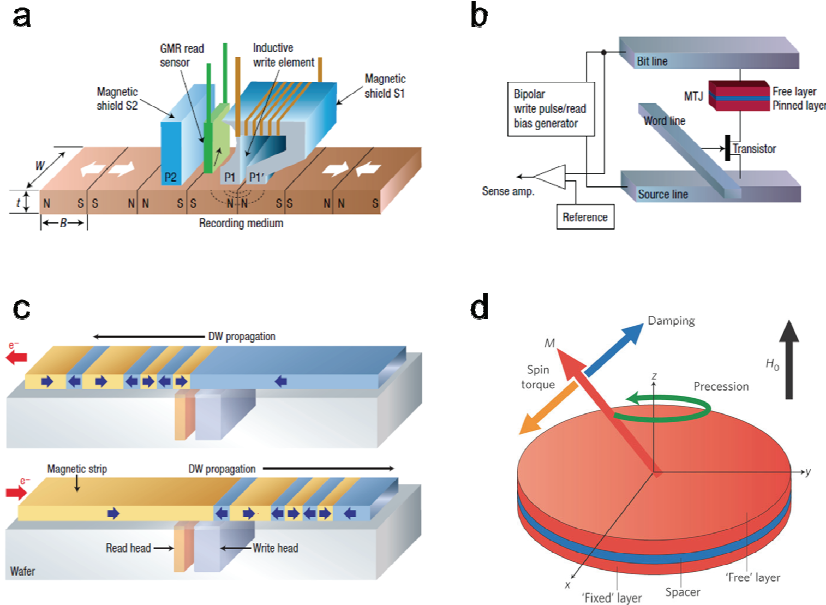


**FIG. 1.1** Examples of spintronic devices: (a) magnetoresistive head for hard-disk recording, (b) spin-transfer torque (STT) magnetic random access memory, (c) Domain wall storage devices, (d) Spin-torque oscillator consisting of a fixed magnetic layer, a non-magnetic spacer and a free magnetic layer ( a, b, and c: modified from [5], d: modified from [43]).

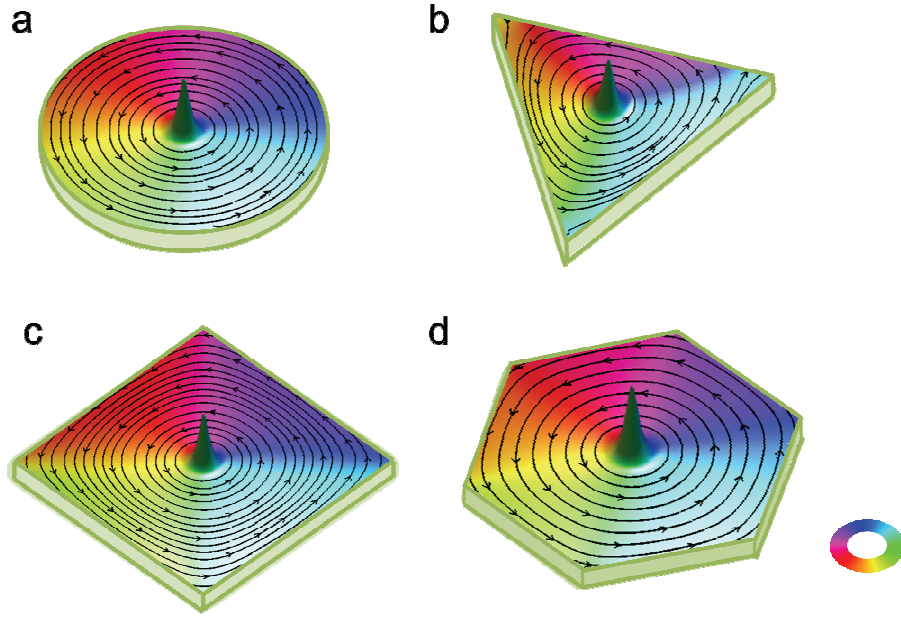


**FIG. 1.2** Magnetic vortex configuration in variable confined structures. (a) circular, (b) triangular, (c) square, (d) hexagonal structure. The color and height indicate the in-plane magnetization direction and relative out-of-plane magnetization, respectively.

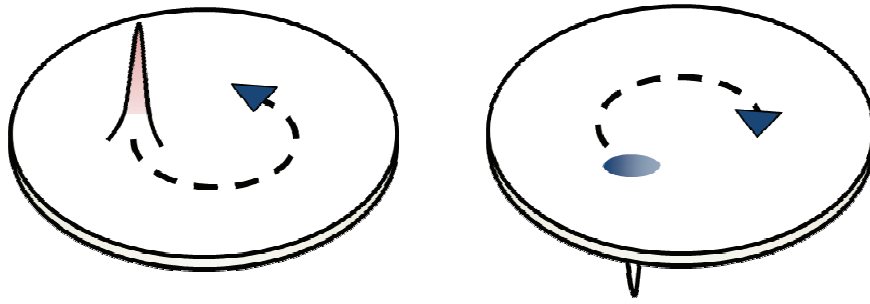


**FIG. 1.3** A schematic illustration of the translational mode. The dashed arrows represent the rotational direction of each vortex core.

## Chapter 2

### Research Background

#### 2.1 Micromagnetics

Some crystals of specific 3d transition metal such as Fe, Ni and Co have spontaneous magnetic moment even in the absence of magnetic field. These materials are called ferromagnets, and the magnetic moment results from the ordered arrangement of electron spins parallel to each other in the crystals. The interaction between the magnetic moments of atomic spins is called exchange interaction. From the Heisenberg model, the energy due to exchange interaction between atomic spins  $S_i$  and  $S_j$  can be expressed as

$$E = -2J_{\text{ex}} S_i \cdot S_j \quad (2.1.1)$$

where  $J_{\text{ex}}$  is an exchange integral related to the overlap of the charge distribution of the atoms  $i, j$ . In ferromagnetic materials,  $J_{\text{ex}}$  is positive, and so a parallel spin alignment is preferred. However, in real material, the alignment is not determined by only the exchange energy. Other energies such as crystalline anisotropy energy, magnetostatic energy, and Zeeman energy also contribute to the alignment of spins. In a crystal, the moment of electron orbits are produced by the crystalline field and coupled with the spin magnetic moment. The coupling is caused by crystalline anisotropy energy, which allows the spins to align along the well-defined axes. The magnetostatic energy is the energy that reduces the field caused by magnetization inside the

ferromagnet. Commonly, this energy is expressed as shape anisotropy. Meanwhile, the origin of Zeeman energy is somewhat different from the others: it does not come from the medium itself but rather is the response to the external magnetic field. Considering these energies, the total energy of a ferromagnet can be written as

$$E = E_{\text{ex}} + E_a + E_m + E_H \quad (2.1.2)$$

where  $E_{\text{ex}}$ ,  $E_a$ ,  $E_m$ ,  $E_H$  is the exchange energy, crystalline anisotropy energy, magneto-static energy, and Zeeman energy, respectively. Because the quantum mechanical approach including all of these energies cannot be solved without rough approximation, a method to describe the magnetization has been developed by using classical physics in a continuous medium. The theory was named *micromagnetics* by W. F. Brown [44, 45]. In this theory, the material is considered as a continuous medium, and the quantum spin numbers are replaced by classical vectors.

In this approach, each energy can be expressed as

$$E_{\text{ex}} = \int \frac{A}{M_s^2} [(\nabla \mathbf{M}_x)^2 + (\nabla \mathbf{M}_y)^2 + (\nabla \mathbf{M}_z)^2] dV \quad (2.1.3)$$

$$E_a = \int w_a dV \quad (2.1.4)$$

$$E_m = \int -\frac{1}{2} \mathbf{M} \cdot \mathbf{H}' dV \quad (2.1.5)$$

$$E_H = \int -\mathbf{M} \cdot \mathbf{H}_{\text{ext}} dV \quad (2.1.6)$$

where  $\mathbf{M}$  is the continuous vector field of magnetization,  $A$  is the exchange constant,  $M_s$  is the saturation magnetization,  $w_a$  is the energy density of

anisotropy energy,  $\mathbf{H}'$  is the demagnetization field due to the dipoles inside the structure, and  $\mathbf{H}_{ext}$  is the external magnetic field applied to the material.

For the case of uniaxial anisotropy, the  $w_a$  is given by

$$w_a = K_1 \sin^2 \theta + K_2 \sin^4 \theta \quad (2.1.7)$$

where  $K_1$  and  $K_2$  are anisotropy constants obtained by experimentation.

Whereas, for the cubic anisotropy, the energy density can be expressed

$$w_a = K_1(m_x^2 m_y^2 + m_y^2 m_z^2 + m_z^2 m_x^2) + K_2 m_x^2 m_y^2 m_z^2 \quad (2.1.8)$$

where  $\mathbf{M}/M_s = (m_x, m_y, m_z)$ .

The time-dependent variation of magnetization  $\mathbf{M}$  can be described by the cross-product of  $\mathbf{M}$  and the effective field  $\mathbf{H}_{eff}$ , which is a negative derivative of total energy[46]

$$\frac{d\mathbf{M}}{dt} = -\gamma_0 \mathbf{M} \times \mathbf{H}_{eff} \quad (2.1.9)$$

where  $t$  is the time,  $\gamma_0 (>0)$  is the gyromagnetic ratio, and the effective field is

$$\mathbf{H}_{eff} = \frac{A}{M_s^2} \nabla^2 \mathbf{M} - \frac{1}{M_s} \frac{\partial w_a}{\partial \mathbf{m}} + \mathbf{H}' + \mathbf{H}_{ext} \quad (2.1.10)$$

Considering the decay in the changes of the magnetization, the equation can be modified with the phenomenological damping term [47],

$$\frac{d\mathbf{M}}{dt} = -\gamma \mathbf{M} \times \left( \mathbf{H}_{eff} - \frac{\alpha}{M_s} \frac{d\mathbf{M}}{dt} \right) \quad (2.1.11)$$

where  $\alpha$  is the dimensionless Gilbert damping constant. Figure 2.1 shows the contribution of each term on the right-hand side of this equation.

In this study, micromagnetic simulation of magnetization dynamics

was conducted on the basis of equation (2.1.11) called the Landau-Lifshitz-Gilbert (LLG) equation. For the purposes of the simulation, most widely used open source code, OOMMF (Object Oriented Micromagnetic Framework, developed by the National Institute of Standards and Technology, USA), was utilized.

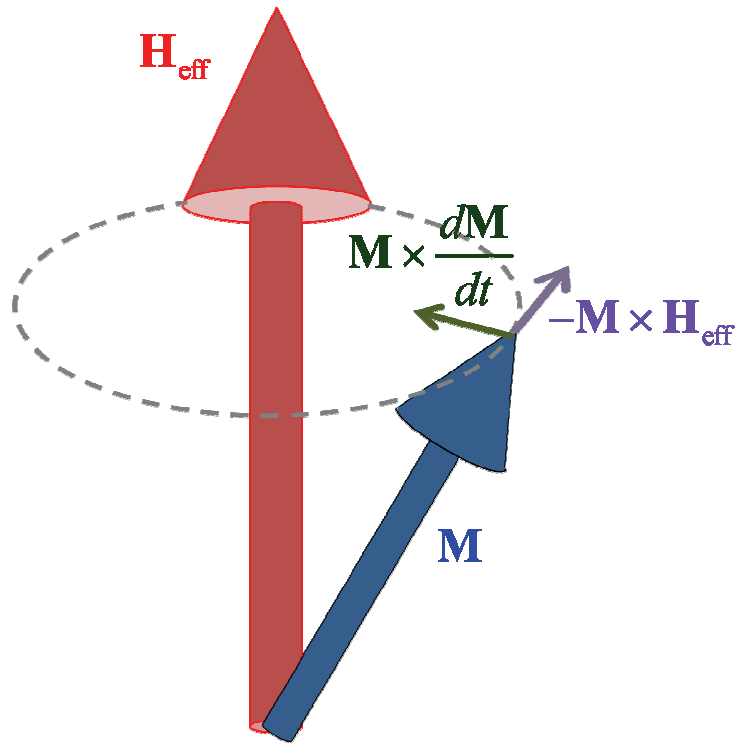


**FIG. 2.1** Schematic representation of the precession of magnetization  $\mathbf{M}$  around effective field  $\mathbf{H}_{\text{eff}}$ .



## 2.2 Translational mode of magnetic vortex

The motion of the magnetic vortex can be determined by a well-known force balance equation – *Thiele's equation*[48, 49], which describes the steady-state motion of magnetic domains by collective coordinates rather than individual magnetization vectors, considering the gyroscopic force, the damping force, and the derivative of potential energy. Assuming invariable  $|\mathbf{M}|$  and a steady state of magnetic domain, the equation (2.1.11) can be written

$$(\gamma / m_0)\mathbf{F} + \mathbf{G} \times \mathbf{V} + \mathbf{D} : \mathbf{V} = 0 \quad (2.2.1)$$

where  $\mathbf{V}$  is the velocity of the structure,  $\mathbf{G}$  is the gyrovector,  $\mathbf{D}$  is the dissipation dyadic, and  $m_0$  is the magnitude of the local magnetic moment per unit area. The vector  $\mathbf{F}$  denoting the static force can be expressed as a position derivative of the potential energy  $W(\mathbf{X})$  of the vortex as shifted from its equilibrium position at  $\mathbf{X}=(x, y)=0$ . The corresponding equation of motion is

$$-\mathbf{G} \times \dot{\mathbf{X}} - \hat{D}\dot{\mathbf{X}} + \partial W(\mathbf{X}) / \partial \mathbf{X} = 0. \quad (2.2.2)$$

In a vortex-state soft magnetic cylindrical dot, for small displacement  $\mathbf{X}$ , the potential energy of the structure considering exchange energy  $W_{exch}$  and magneto-static energy  $W_{demag}$  can be expressed, by a parabolic function of vortex-core position, as

$$W(\mathbf{X}) = W_{exch}(\mathbf{X}) + W_{demag}(\mathbf{X}) = W_0 + \frac{1}{2}\kappa\mathbf{X}^2 \quad (2.2.3),$$

where the stiffness  $\kappa$  is the proportional coefficient of the restoring force to

the vortex core displacement [50]. For the circular motion velocity of the magnetic vortex,  $\dot{\mathbf{X}}$  can be denoted through the angular frequency vector  $\boldsymbol{\omega} = \omega \hat{\mathbf{z}}$  as  $\dot{\mathbf{X}} = \boldsymbol{\omega} \times \mathbf{X}$ . The equation (2.3.2) can then be reformulated as

$$-|G|\omega\mathbf{X} - D\omega\mathbf{X} + \kappa\mathbf{X} = 0 \quad (2.2.4),$$

and accordingly, the frequency of the translational mode can be deduced from the equation

$$\omega = \frac{\kappa}{|G| + D}. \quad (2.2.5)$$

The translational mode was observed by various technique for a variety of structures. Argyle *et al.* [51] observed the gyrotropic mode of a vortex at the intersection between two Néel walls in the garnet film in 1984. Park *et al.* observed vortex gyration during relaxation after excitation by a short pulse field in an isolated circular Permalloy (Py,  $\text{Ni}_{80}\text{Fe}_{20}$ ) disk using time-resolved Kerr microscopy. Choe *et al.* directly observed the dynamic change of a vortex-state magnetic domain using time-resolved X-ray photoemission electron microscopy (X-PEEM). They discerned that the contrary gyration of the vortex core depends on the vortex polarization.

### 2.3 Interaction between magnetic vortices

The magnetostatic interaction between vortex-state ferromagnetic disks has been investigated experimentally and theoretically, focusing on the magnetization reversal due to the nucleation and annihilation of magnetic vortices in a disk array [29, 52-55]. For the static interaction, the vortex chirality is much more important than the polarization of the vortex core. There is a paucity of research on the effect of the interaction on the dynamics of vortices. The above-discussed translational mode also is affected by the interaction between vortices. The collective mode of coupled magnetic vortices in two physically separated circular disks was investigated by Shibata *et al.* in 2003 [42]. In that work, as illustrated in Fig 2.2, they suggested four possible collective modes and eigenfrequencies of vortex core motion for the variable polarization and chirality of each vortex, using analytical calculations based on a rigid vortex model. For the calculation, the coupled Thiele's equations of motion are given by

$$\begin{aligned} -\mathbf{G}_1 \times \dot{\mathbf{X}}_1 - \hat{D}_1 \dot{\mathbf{X}}_1 + \partial W(\mathbf{X}_1, \mathbf{X}_2) / \partial \mathbf{X}_1 &= 0 \\ -\mathbf{G}_2 \times \dot{\mathbf{X}}_2 - \hat{D}_2 \dot{\mathbf{X}}_2 + \partial W(\mathbf{X}_1, \mathbf{X}_2) / \partial \mathbf{X}_2 &= 0 \end{aligned} \quad (2.4.1)$$

Using a rigid vortex model [50] which assumes that the vortex does not deform as the core moves from the disk center, and considering only the side-surface charges of each disk, the total energy  $W$  containing the interaction energy is written as

$$\begin{aligned}
W(\mathbf{X}) &= \sum_{i=1}^2 [W_{exch}(\mathbf{X}_i) + W_{demag}(\mathbf{X}_i)] + W_{int}(\mathbf{X}_1, \mathbf{X}_2) \\
&= W_0 + \frac{1}{2} \kappa_1 \mathbf{X}_1^2 + \frac{1}{2} \kappa_2 \mathbf{X}_2^2 + \frac{C_1 C_2}{R^2} (\eta_x x_1 x_2 - \eta_y y_1 y_2)
\end{aligned} \tag{2.4.2}$$

where  $\eta_x$  and  $\eta_y$  represent the interaction strengths along the  $x$  and  $y$  axes, respectively, and are functions of the interdistance. The interaction originates from the side surface charges produced by external fields.

The first experimental observation of the collective dynamics of two vortices in an elliptic disk was achieved by Buchanan *et al.* [56, 57]. In broadband microwave reflection measurements, the translational eigenmodes characteristic of coupled vortices was detected. Similarly to the case of coupled circular disks, four possible eigenmodes were identified from micromagnetic simulation results. Unlike static interaction, the polarization of vortices dominates the coupled dynamics, because the relative positions of the vortex cores strongly depend on the polarization of each.

Gusliencko *et al.* [58] investigated, *via* analytical and numerical calculation, the dynamics of two interacting vortices for a model system consisting of two cylindrical ferromagnetic layers separated by a nonmagnet spacer. They took notice of the effect of the interaction on the trajectory of each vortex core. In order to elucidate the dynamics, they induced two collective coordinates corresponding to the difference between the vortex cores' displacements and mean displacement. The vortex-core trajectories in the system were explained as the superposition of the fast circular motion of

each core around the disk center and the slow change of the circular orbit position. However, seemingly there is as yet no experimental study on the dynamics of coupled vortices in physically disconnected structures.

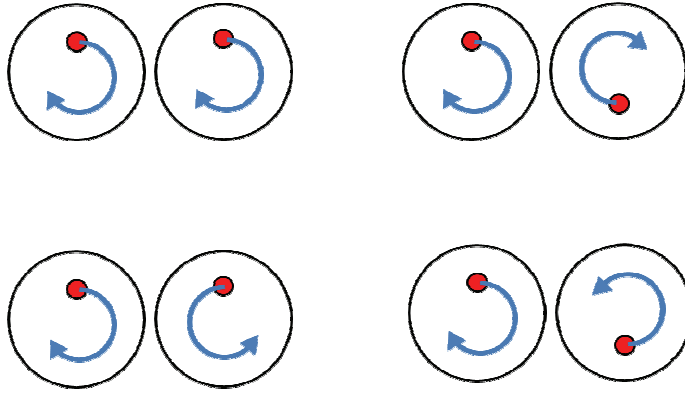


**FIG. 2.2** Four kinds of collective motion. The solid dots represent the initial phases of the vortex cores, and the arrows the represent rotational directions of the vortex cores. Reproduced from [42].

## **Chapter 3**

### **Sample Fabrication**

The samples were fabricated using a sputtering and e-beam evaporator system and e-beam lithography. X-ray diffraction and atomic force microscopy were used for characterization of the physical properties, whereas magneto-optical Kerr measurement and superconducting quantum interference device measurement were utilized for elucidation of the magnetic properties. To obtain sufficient X-ray transmission, an SiN membrane was used as the substrate. E-beam lithography and the lift-off technique were used to construct the microstructures. The magnetic field generated from the patterned electrode was determined by analytical and numerical calculation.

### 3.1. Thin film deposition

The thin film was prepared in a clustering vacuum chamber (see Fig 3.1) consisting of 7 DC sputtering sources (A320, AJA international Inc.), 1 RF sputtering source, 4 e-beam guns (EFM4, Omicron), an *in-situ* magneto-optical Kerr effect measurement system, and a plasma oxidation system. Although a vacuum chamber for pulsed laser deposition also was connected with the clustering system, laser deposition was not used in this study. Two 2-inch wafers and two arbitrary-shaped smaller samples can be loaded onto the chamber at the same time. Using this system, multilayered thin film can be deposited without vacuum braking. Metallic thin films, specifically Py, Co, Ni, and Cu, were prepared using a DC sputtering source under  $5 \times 10^{-9}$  Torr base pressure and Ar pressure of around 1 mTorr. A chimney and gas-injection line through each sputtering gun made it possible to generate plasma even at low working pressure and to make clean film. The deposition time was automatically controlled by a pneumatic shutter and electronic timer. Prior to fabricating the patterned sample, a thin film was deposited on a thermally oxidized p-type Si wafer for characterization. The physical properties of the film were determined by X-ray reflectivity measurement. Figure 3.2 shows examples of the measured data and the simulated result. The thickness, density, and roughness of the film could be estimated from the resultant data, which included the critical angle of total reflection, the periodicity of the fringes, and the depth of the pick. The local flatness was confirmed by atomic force



microscopy. Other features that had to be checked were the magnetic properties of the film, which were *in-situ* measured by a surface magneto-optical Kerr effect measurement system installed on the e-beam evaporator chamber. The Kerr intensity and rotation, shown in Fig.3.3a, were proportional to the magnetization of the films. In our system, the magnetization component parallel and normal to the film surface can be measured under external magnetic fields parallel and normal to the film surface, respectively. The Kerr measurement offers most of the magnetic properties but cannot measure the value of saturation magnetization. In order to acquire an accurate saturation magnetization value therefore, a superconducting quantum interference device (SQUID) measurement was performed as shown in Fig 3.3b. The obtained value for permalloy was consistent with the commonly known value: 860 emu/cm<sup>3</sup>.

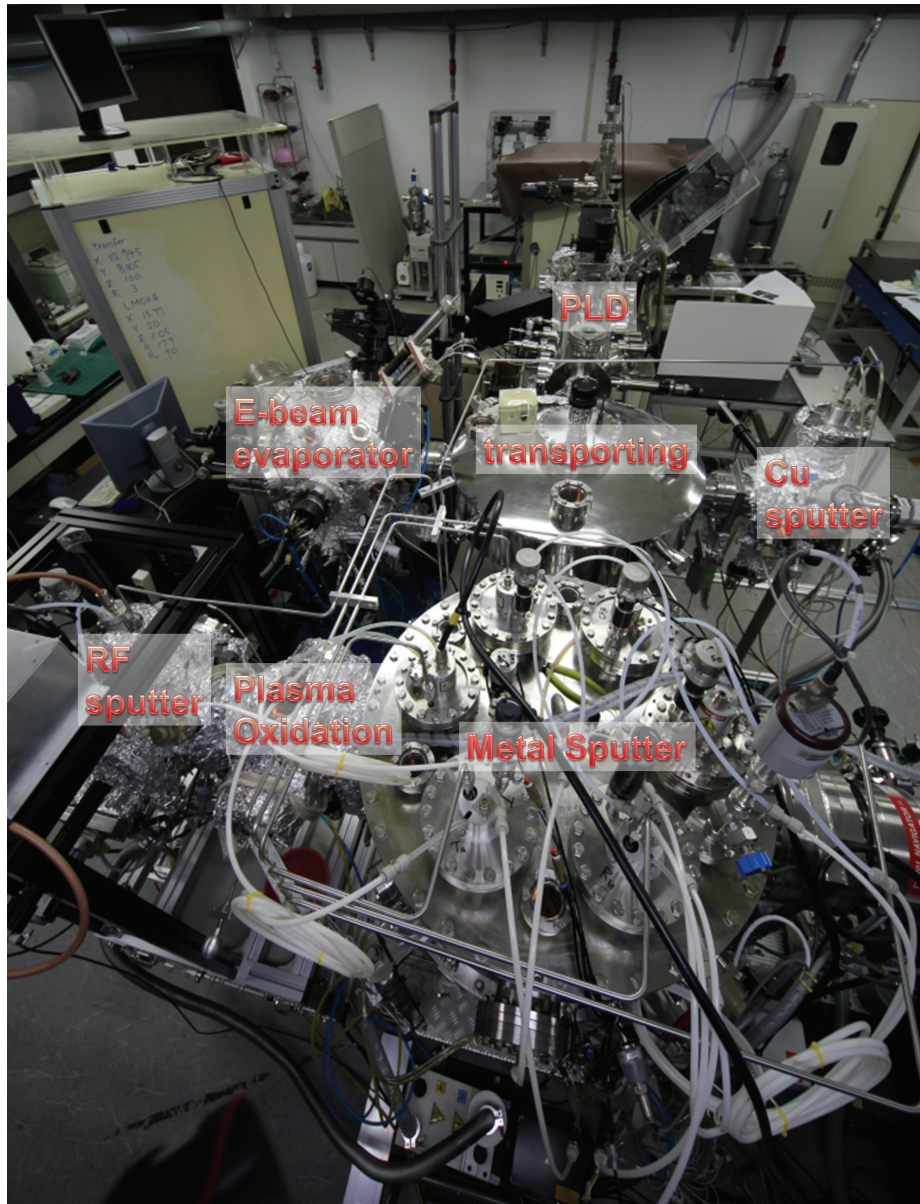


**FIG.3.1** A clustering deposition system.

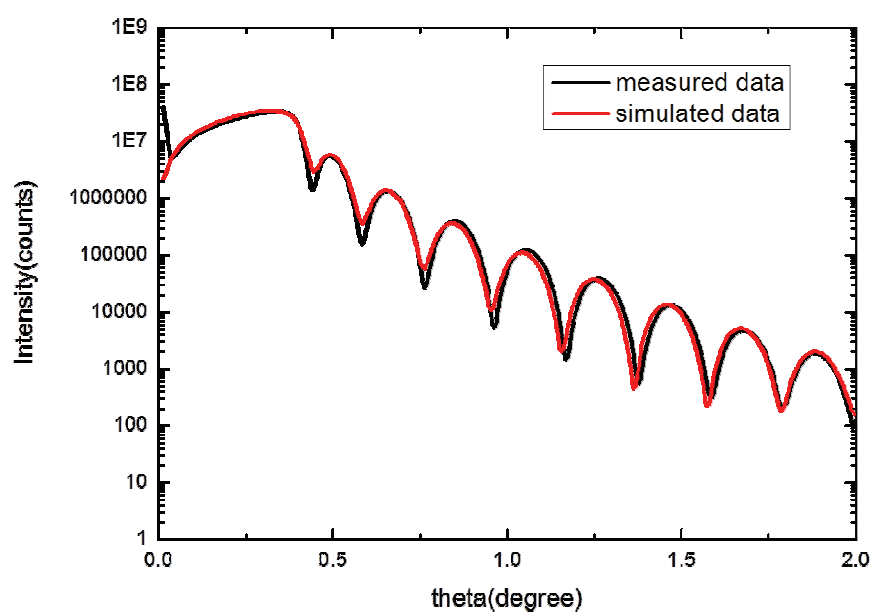


**FIG. 3.2** Low angle X-ray diffraction for Py thin film.

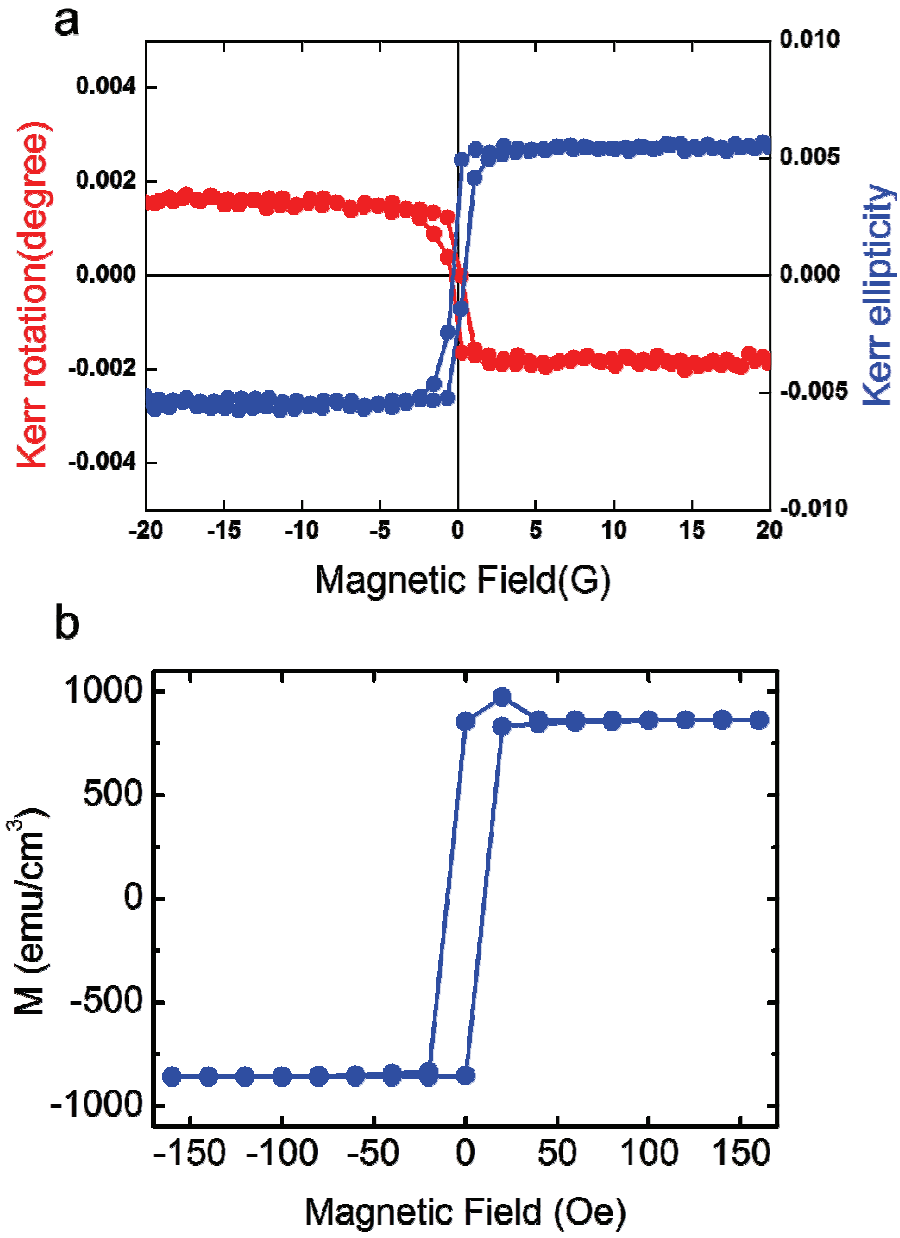


**FIG. 3.3** (a) SMOKE and (b) SQUID hysteresis loops of Py measured by the longitudinal configurations.

### 3.2 Lithography

Most of microstructure fabrication processes were carried out in a cleanroom at the *Korea Advanced Nano Fab Center* (KANC) in Suwon, Gyeonggi, Republic of Korea. The sample was prepared by e-beam lithography and a lift off process. Two types of electron beam lithography instrument (JBX6000FS and JBX9300FS, Jeol) were utilized for patterning, each having an acceleration voltage of 50 keV and 100 keV, respectively.

In order to obtain sufficient soft x-ray transmission, back etched silicon nitride membrane windows (Silson Ltd.) were used as substrates. The silicon nitride membrane windows consisted of  $1.5 \times 1.5 \text{ mm}^2$  square sheets in  $5 \times 5 \text{ mm}^2$  square silicon supporting frames. The resistivity of the substrates was maintained at over 8400 ohm to reduce the possibility of damage. An illustration of the fabrication process is provided in Fig. 3.4. The electron-sensitive positive resist PMMA 950K A3 (3% 950K PMMA in anisole, Micro Chem. Corp.), a LOR1A (Micro Chem. Corp.), and a ZEP520-A (Nippon Zeon Corp.) were used.

After cleaning the substrates, the PMMA 950K A3 was spin-coated onto them at a speed of 3000 rpm. The thickness of the resist was about 150 nm, but had some deviation due to the flexibility of the membrane. Then, the sample was baked on a hotplate at 170°C for 5 minutes. The dosage of e-beam exposure, as determined by a preliminary round of deposition and lift-off, varied from 100 to 400  $\mu\text{C}/\text{cm}^2$ , depending on the patterns. Normally, the

dosage for JBX9300FS is twice as large as for JBX6000FS. After e-beam exposure, the resist was developed by soaking in MIBK solvent diluted with IPA. Then, the developer was rinsed in IPA, followed by N<sub>2</sub> blowing to dry the IPA.

In a specific case, a bi-layer process was used for clean side wall. LOR1A and ZEP520-A were used as the bottom and top layers of the resists, respectively. ZED-N50 (Nippon Zeon Corp.) and IPA were utilized as a developer and rinser for ZEP520-A, while AZ 300MIF (AZ Electronic Materials Ltd.) and DI water were used for LOR1A. After thin-film deposition using electron-beam evaporation and DC sputtering described in previous section, the excess material on top of the resist was removed by a lift-off process. Warmed Remover-PG (Micro Chem. Corp.) was used to remove the resist. For the bi-layer process, the sample was soaked in ZDMAC (Nippon Zeon Corp.) to dissolve the ZEP520-A before soaked in Remover-PG. Sequentially, the sample was rinsed and cleaned by IPA and DI water.

Phased inspection by optical microscopy and SEM was performed to confirm the patterned resist and film. It is important to note that SEM inspection can damage a sample. To prevent this, a clone was used for the inspection. Figure 3.5 shows examples of the patterned structure and resists.

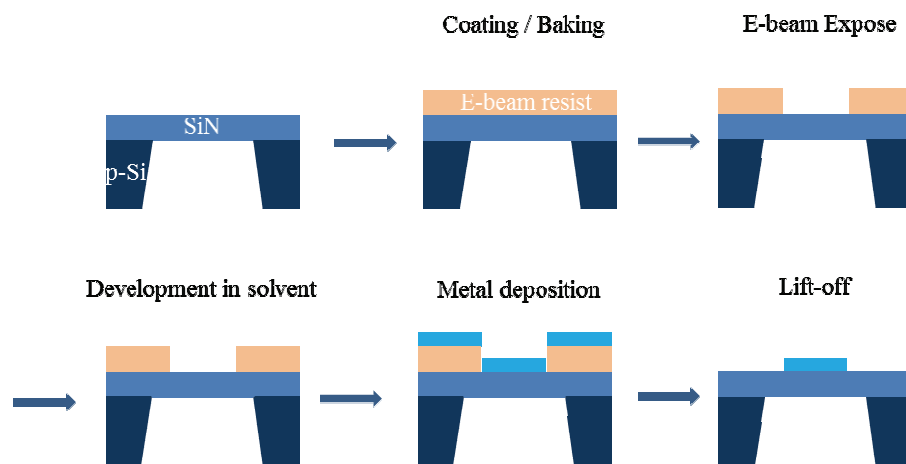


**FIG. 3.4** E-beam lithography processes.

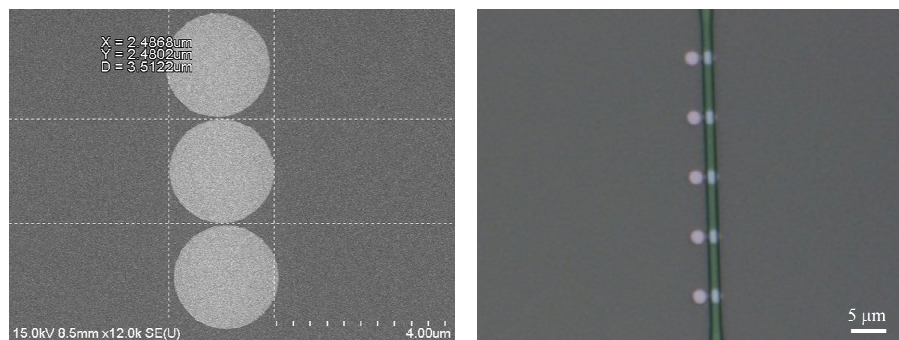


**FIG. 3.5** SEM image of  $2.5\mu\text{m}$  Py disks after patterning (left). Optical microscopy image of electrode pattern (right).

### 3.3 Magnetic field strength and distribution

A stripline to generate the Oersted fields should be designed considering the field strength and spatial distribution. Based on Ampere's law with the value of current ( $I$ ), flowing through the Cu stripline with width  $2a$  and thickness  $2b$ , calculated by using Ohm's Law  $I = V_{\text{out}}/Z$  with the measured output voltage  $V_{\text{out}}$  and the impedance of the used oscilloscope of  $Z = 50 \Omega$ , the local Oersted field at the  $(x, z)$  in [59] is given as

$$\begin{aligned} H_x &= \frac{-I}{8\pi ab} \left[ \begin{aligned} &u \left[ \frac{1}{2} \ln \left( \frac{g^2 + u^2}{h^2 + u^2} \right) + \frac{g}{u} \arctan \left( \frac{u}{g} \right) - \frac{h}{u} \arctan \left( \frac{u}{h} \right) \right] \\ &-v \left[ \frac{1}{2} \ln \left( \frac{g^2 + v^2}{h^2 + v^2} \right) + \frac{g}{v} \arctan \left( \frac{v}{g} \right) - \frac{h}{v} \arctan \left( \frac{v}{h} \right) \right] \end{aligned} \right] \\ H_z &= \frac{I}{8\pi ab} \left[ \begin{aligned} &g \left[ \frac{1}{2} \ln \left( \frac{g^2 + u^2}{v^2 + g^2} \right) + \frac{u}{g} \arctan \left( \frac{u}{g} \right) - \frac{v}{g} \arctan \left( \frac{g}{v} \right) \right] \\ &-h \left[ \frac{1}{2} \ln \left( \frac{u^2 + h^2}{v^2 + h^2} \right) + \frac{u}{h} \arctan \left( \frac{h}{u} \right) - \frac{v}{h} \arctan \left( \frac{h}{v} \right) \right] \end{aligned} \right] \end{aligned} \quad (3.3.1)$$

with  $u=a-x$ ,  $v=-a-x$ ,  $g=b-z$ , and  $h=-b-z$ .

As shown in Fig. 3.7, simulation using finite element method arise almost same results with the equations (3.3.1).



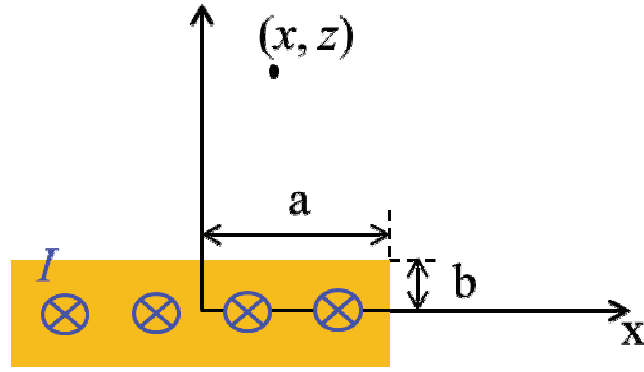


**FIG 3.6** Schematic geometry for the magnetic field calculation.

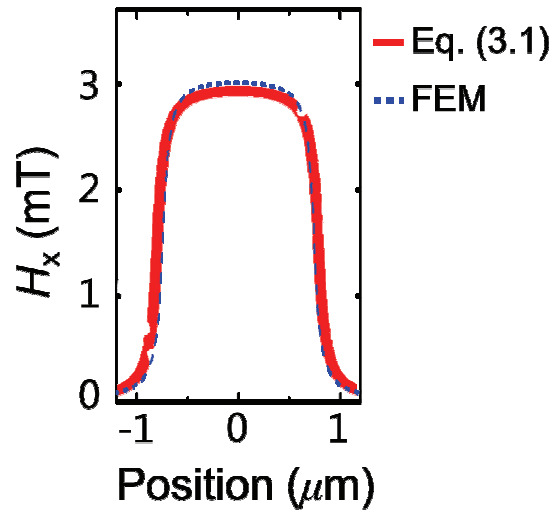


**FIG 3.7** Spatial distribution of magnitude of magnetic fields generated from 1.5  $\mu\text{m}$  wide and 75 nm thick Cu stripline. The field strength was obtained 25 nm below the bottom surface of the stripline.

## **Chapter 4**

### **Magnetic Imaging using Transmission Soft X-ray Microscopy**

In this chapter, several magnetic imaging techniques are introduced. Then, the fundamental theory and experimental setup of magnetic X-ray transmission microscopy are presented. The experimental setup makes it possible to investigate sub-nanosecond and nanometer-scale magnetization dynamics. Prior to observation of the dynamic properties of the magnetic vortex, the static behaviors of the vortex-state magnetic elements were investigated by X-ray microscopy.

#### **4.1 Magnetic imaging techniques**

For magnetic microstructural observation, many techniques have been used. In 1932, F. Bitter decorated the stray fields above a domain pattern using fine magnetic powders [60]. Based on a similar principle, magnetic force microscopy, which records the magneto-static forces or force gradients between a ferromagnetic tip and a sample, is widely used these days. This technique offers relatively good accessibility and connectivity with other measurement modalities, because most of the setup, excepting the probe is identical to atomic force microscopy. In magnetic force microscopy, the spatial resolution can be as good as 20 nm by reducing the tip radii (see Fig. 4.1). Meanwhile, these techniques have a limitation in that they do not directly depend on the magnetic domain structures but on the stray fields from the sample.

Another approach to observation of magnetic structures is to use magnetic optical activity based on the a weak dependence of optical constants on the magnetization direction [61]. As a result of the difference in refractive indices of left and right circularly polarized light in medium (which is due to the external magnetic fields), a light rotates its polarization angle. The activities of a transparent and reflective beam are referred to, respectively, as Faraday and Kerr effects. In most cases the medium is not transparent, and thus magnetic imaging using the Kerr effect is more widely used (see Fig. 4.2). Another magnetic optical activity is magnetic circular dichroism (MCD),

which arises from the different absorption coefficients of the two circularly polarized lights. MCD only occurs in absorbing spectral regions. These magneto-optical techniques using visible light are non-destructive and relatively fast, whereas their spatial resolution is limited due to the wavelength of visible light in a conventional setup. On the other hand, a technique for observation of the dynamic behaviors of the magnetic vortex in submicron-size patterned structures should provide a time resolution of sub-nanoseconds and a spatial resolution of several nanometers. This technique is discussed in the following section.

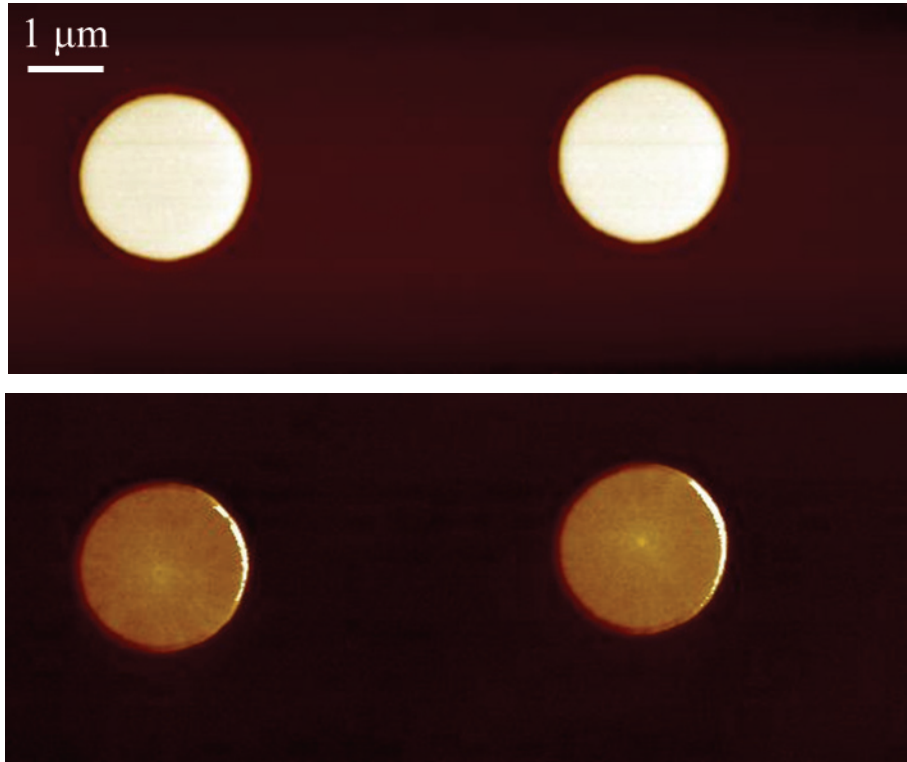


**FIG. 4.1** Topography (top) and magnetic contrast (bottom) images for 2  $\mu\text{m}$  diameter 50 nm thick Py disks obtained by scanning probe microscopy. The relatively bright spot in the right disk corresponds to the upward vortex core, whereas the dark spot in the left disk indicates the downward direction.

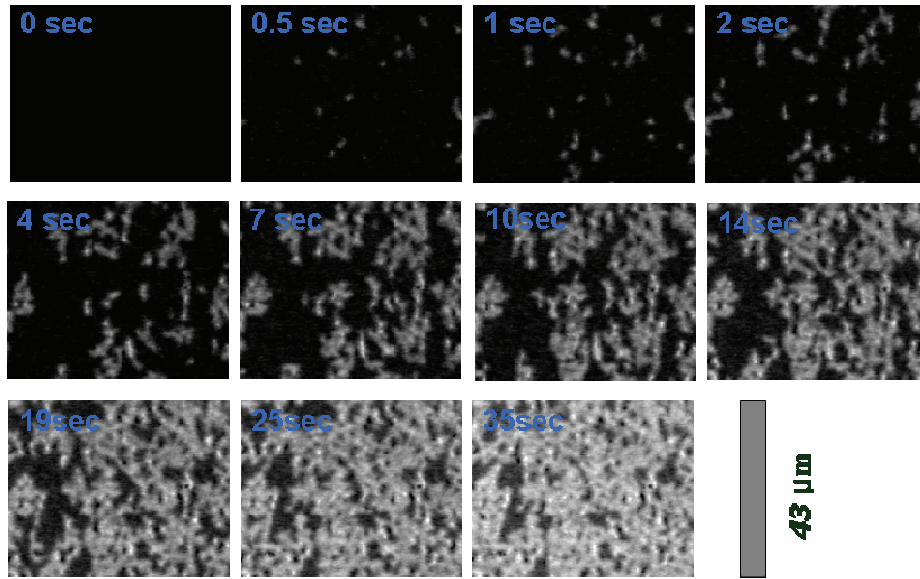


**FIG. 4.2** Magnetic-domain nucleation and growth during magnetization reversal of  $\text{Pd}(5 \text{ nm})/[\text{Co}(0.4 \text{ nm})/\text{Pd}(2.2 \text{ nm})]_5$  observed by Kerr microscopy under perpendicular magnetic field of 350 Oe. The relatively white and black regions represent the upward and downward magnetization directions, respectively.

## 4.2 X-ray magnetic circular dichroism

In the X-ray region, effects analogous to the conventional magneto-optical effects also exist. Due to the lack of suitable instruments for measurement of the polarization rotation of X-rays, the dichroic effect for circularly polarized light is used instead. The effect is called X-ray magnetic circular dichroism (XMCD) [62]. The advantages of XMCD spectroscopy are the element-specific, quantitative analysis of spin and orbit moments, good spatial resolution [63], and high chemical sensitivity. In ferromagnetic  $3d$  transition materials, the photo absorption for circularly polarized X-rays depends strongly on the relative orientation between the projection of the magnetization onto the photon propagation direction and the helicity of the photons, especially in the vicinity of the binding energies of the atomic core electrons of the  $L_{2,3}$  absorption edges. As shown in Fig. 4.3, in XMCD spectroscopy it makes no difference whether the X-ray polarization is changed under the fixed magnetization direction or the magnetization direction is changed under fixed X-ray helicity.

The magnetic contrast in imaging as reliant on XMCD [64] is provided by deviation of the absorption coefficient between two circularly polarized rays  $\Delta\mu(E)$  relative to the non-excited (core-level) absorption coefficient  $\mu_{|i>}$  in

$$\frac{\Delta\mu}{\mu_{|i>}}(E) = \frac{\sigma_c}{\sigma_{|i>}}(E)(\mathbf{m} \cdot \hat{\mathbf{z}})P_c \quad (4.2.1)$$

where  $\sigma_c$  is the magnetic absorption cross section,  $\sigma_{|i>}$  is the polarization

averaged atomic cross-section, and  $\mathbf{m} \cdot \hat{\mathbf{z}}$  is the projection of the normalized magnetic moment onto the incident direction of the X-rays. From this relation, the contrast depends on only the perpendicular magnetization when the incident direction of the X-ray is normal to the sample. Thus, for imaging in-plane magnetization components of a sample, the X-ray should be incident to the sample at a certain angle.

In many cases, it is not necessary to change the polarization direction of photons, because contrast sufficiently high to ensure the magnetic domains can be obtained by subtracting the structural contrast from an image.



### X-Ray Magnetic **Circular** Dichroism

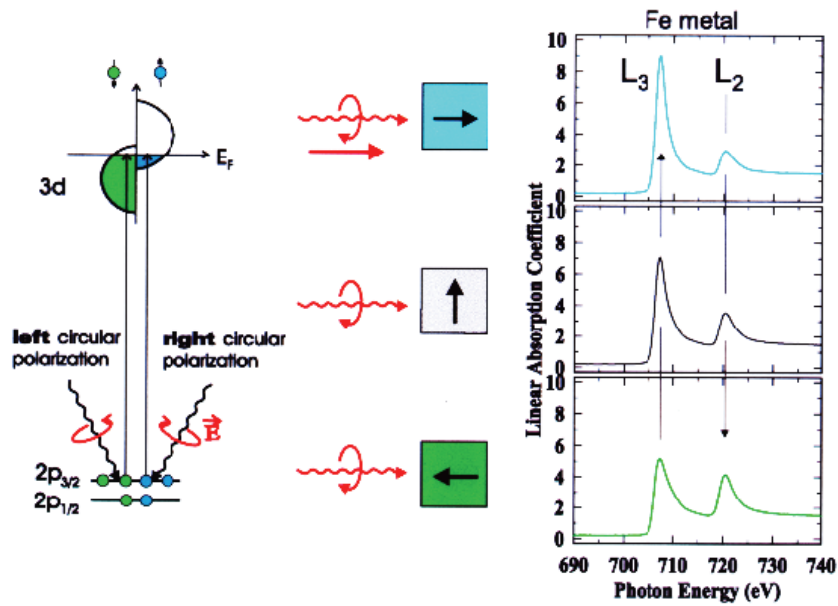


**FIG. 4.3** (from [65]) Illustration of X-ray magnetic circular dichroism. (left) Split of  $d$  valence band of magnetic material. The left circularly polarized X-ray mainly excites spin-down photoelectrons, whereas the right circularly polarized X-ray excites spin-up photoelectrons. (right) Fe  $L$  edge absorption spectra of right circularly polarized X-ray for different magnetization directions.

### 4.3 Full-field magnetic transmission soft X-ray microscopy (MTXM)

On the basis of the principle discussed in section 4.2, element specific and energy-dispersive magnetic imaging can be achieved with X-ray transmission geometry [65, 66]. In this work, we utilized the full-field soft X-ray microscope located on Beamline (BL) 6.1.2 at the Advanced Light Source (ALS) in Berkeley, CA [67] (see Fig 4.4). The optical setup of the X-ray microscope, (see Fig. 4.5) consists of the bending magnet source providing elliptically polarized soft X-rays, a monochromator and illuminating assembly (comprising the first Fresnel zone plate [the condenser zone plate] and a pinhole close to the sample), a high-resolution imaging objective lens, the micro zone plate, and a two-dimensional CCD detector (PIXIS 2048). Polychromatic X-rays from the bending magnet of the storage ring were focused onto the sample through a condenser zone plate and a pinhole. The energy can be tuned within the 500 - 1300 eV range at a spectral resolution of  $E/\Delta E$  500~700 by altering the focal length of the monochromator. The X-ray passing through the transparent sample is projected through the micro zone plate onto an X-ray-sensitive CCD camera. The spatial resolution is mainly determined by the outermost zone width of the micro zone plate [68]. For a small numerical aperture, the Rayleigh limitation of the zone plate is given by

$$\Delta r_{\text{Rayl.}} = 1.22 F^{\#} \lambda = 1.22 \Delta r \quad (4.3.1)$$

where  $\lambda$  is the wavelength of the incident x-ray,  $F^{\#}$  is the lens F-number, and  $\Delta r$  is the outermost zone width of the zone plate lens. The resolution

limit can be as good as 15 nm with an advance in the Fresnel zone plate [63]. The micro zone plate generates a typically 2000-fold magnified image onto the CCD camera, which consists of  $2048 \times 2048$  pixels. The field of view is typically 10  $\mu\text{m}$  in diameter. For sensitivity to the in-plane component of the magnetization, the sample surface was positioned at a  $60^\circ$  orientation to the propagation direction of the incident X-rays. The estimated degree of circular polarization was about 50-60% at a bending magnet [67]. In this work, the structural contrast was normalized using an image obtained under a static saturation field.

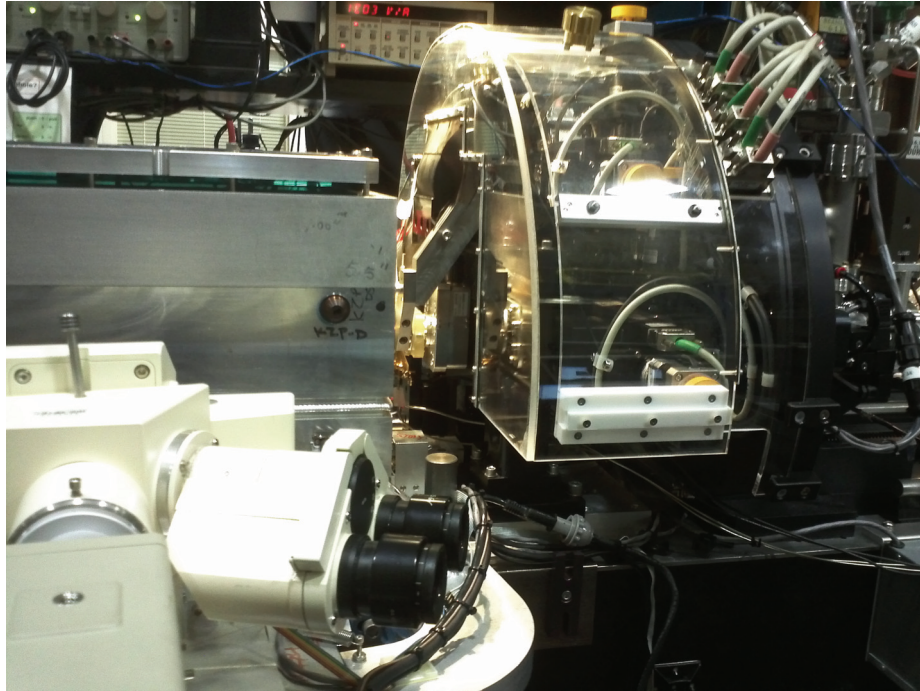


**FIG. 4.4** Magnetic X-ray transmission microscope on BL 6.1.2 at the ALS.

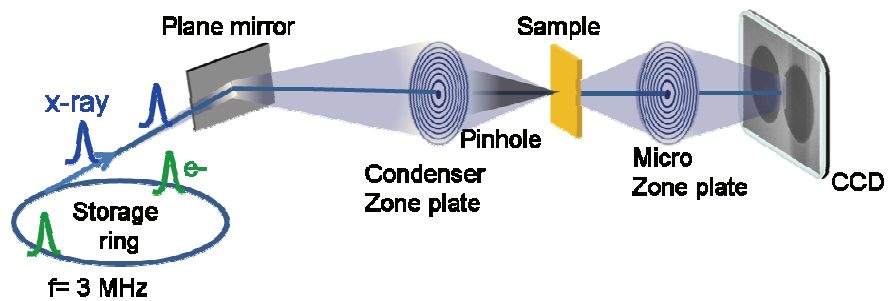


**FIG. 4.5** Schematic illustrations of optical setup for full-field magnetic transmission soft x-ray microscope at ALS BL 6.1.2 used for magnetic imaging.

#### **4.4 Time-resolved imaging using pump-and-probe technique**

The temporal resolution is set by the inherent pulsed time structure of the X-ray source, and is typically about 70 ps in the two-bunch mode operation of the ALS, where two electron bunches of 70 ps length are separated by 328 ns [69, 70]. In order to obtain a sufficient time scale to study the vortex gyration, a stroboscopic pump-and-probe method [71] is used. The clock signal of the synchrotron triggers an arbitrary function generator (Agilent, 81150A), which launches particular pulses (pump) into a stripline of sample so as to create local Oersted fields. In the present study, field pulses were stroboscopically applied, whereas the driving pulses were synchronized with X-ray probe pulses to a frequency of  $\sim 3$  MHz. To measure the temporal evolution of the vortex excitations, the pulses were delayed with respect to the X-ray probe pulses. The arrival time of the X-ray pulses at the sample were monitored by a fast avalanche photo diode. In order to obtain sufficient XMCD contrasts, ten individual images of several million accumulated X-ray flashes measured at the same time delay were integrated. The requirements of the method are that the process should be perfectly repeatable and should be restored to its initial condition before the next pump.

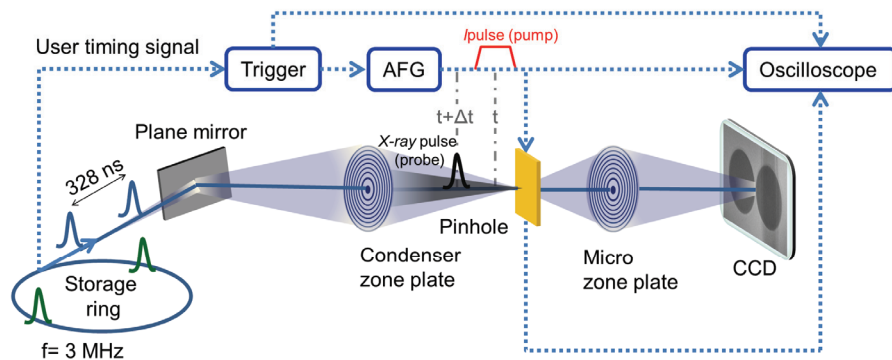


**Fig. 4.6** Schematic illustration of a stroboscopic pump-and-probe scheme used to time-resolved measurements. The clock signal of the synchrotron triggers a pump pulse into a sample. The pump pulse is delayed with respect to the probe X-ray pulse.

## **Chapter 5**

### **Coupled Vortex Cores Oscillation**

As noted in the previous chapter, vortex-core oscillations in micrometer-size (or less) magnetic elements have been intensively studied for their promising applications as microwave emission sources [27, 31-41]. Vortex-core oscillators provide high power output and narrow line widths. Most studies have focused on electrical measurements using isolated single disks [33, 38-40]. However, the needs for high-power signals and high packing density have spurred further studies, not only on coupled vortex-state disks but also on multiple-disk arrays. Vortex random access memory has been suggested as another application of the magnetic vortex [17, 20, 22-25]. The device utilizes resonant excitation of vortex translational modes for information recording. In cases of sufficiently short distances between nearest neighbouring disks, dipolar interaction alters their dynamics [28, 42, 72]. Thus, the determination of the influence of dipolar interaction on vortex dynamics is very important. To characterize the interaction between individual elements, a time- and space-resolving measurement technique is mandatory.

Recent advances in time-resolved microscopy enable imaging of the spin dynamics of nano-scale magnetic elements at a time resolution of

less than 100 ps [73, 74]. Time-resolved full-field imaging is required for simultaneous measurement of different local areas. In the present work, we performed, for the first time, real-time and real-space imaging of vortex gyrations in physically disconnected vortex-state dots, driven directly by field pulses as well as driven indirectly by the dipolar interaction, using a 70-ps-time- and 20-nm-space-resolved magnetic transmission soft x-ray microscope (MTXM) on BL 6.1.2 at ALS, Berkeley.



## 5.1 Sample preparation and experimental setup

The sample studied in this chapter is made by the Meier's group in University of Hamburg. The two-disk system studied was prepared on a 100 nm-thick silicon nitride membrane by electron-beam lithography, thermal evaporation, and lift-off processing. Each Py disk has a diameter of  $2R = 2.4 \mu\text{m}$  and a thickness of  $L = 50 \text{ nm}$ . The disks are arranged in a pair with a center-to-center distance of  $d_{\text{int}} = 2.52 \mu\text{m}$  (see Fig. 5.1). In order to locally excite one vortex, a  $1.5 \mu\text{m}$ -wide and  $75 \text{ nm}$ -thick Cu strip covers the top of the right Py disk, as can be seen in Fig. 5.1. To determine eigenfrequency of the vortex in the isolated Py disks, a broadband-ferromagnetic resonance measurement [72] is utilized. For the measurement, an array of Py disk pairs was placed under a  $7 \mu\text{m}$ -wide stripline. The disks were of the same dimensions ( $2R = 2.4 \mu\text{m}$ ,  $L = 50 \text{ nm}$ ), but a larger value of  $d_{\text{int}} = 3.74 \mu\text{m}$  was used to prevent interaction. The measured resonant frequency was around  $157 \text{ MHz}$ . Measurements of the dynamic evolution of vortex-core gyrations were carried out by full-field MTXM at BL 6.1.2, ALS (Berkeley, CA), utilizing a stroboscopic pump-and-probe technique.

Field pulses of  $5 \text{ mT}$  strength,  $30 \text{ ns}$  length and  $2.5 \text{ ns}$  rise and fall time were stroboscopically applied along the  $x$  axis on which the two disks were placed (see Fig. 5.1a). The driving pulses were synchronized with X-ray probe pulses to a frequency of  $\sim 3 \text{ MHz}$ . To measure the temporal evolution of the vortex excitations, the pulses were delayed with respect to

the X-ray probe pulse. The arrival time of the X-ray pulses at the sample were monitored by a fast avalanche photo diode. In order to obtain sufficient XMCD contrasts, ten individual images of several million accumulated X-ray flashes measured at the same time delay were integrated. The X-ray images were recorded every 1.67 ns.

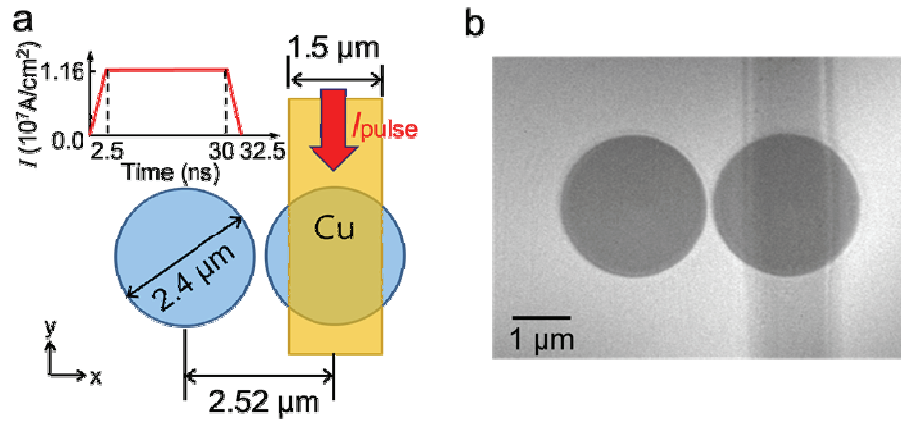


**FIG. 5.1** (a) Schematic illustration of two-disk system and (b) structural transmission soft X-ray image. Inset of (a) shows shape of the current pulse.

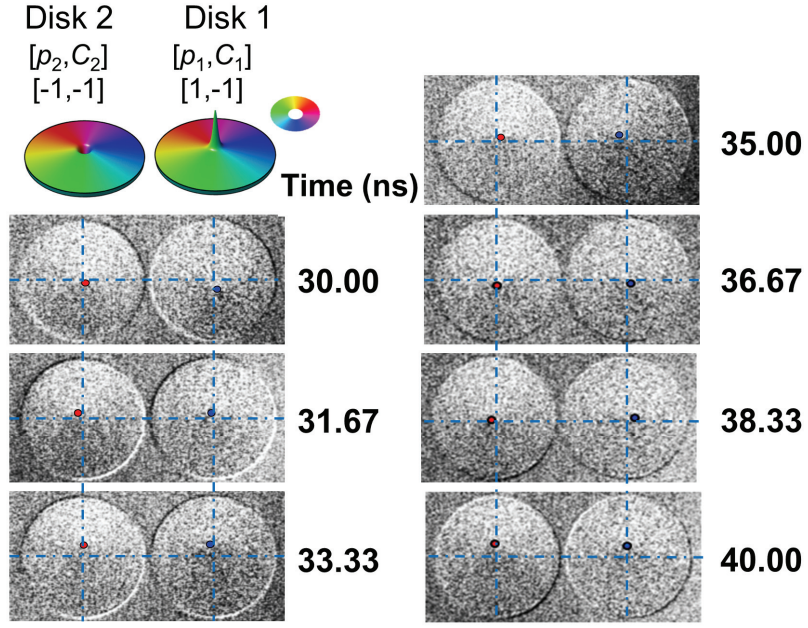
## 5.2 Imaging of vortex core oscillation

Figure 5.2 shows the resultant plane-view data for both disks as measured after a perturbation of the right disk by the pulse field. In the images, the structural contrast is normalized by an image obtained at a static saturation field. The relatively bright region in the disks represents magnetizations that point in the +x direction, whereas the relatively dark area corresponds to opposite-direction magnetizations. Both disks' initial configuration show the same chirality of clockwise in-plane curling magnetization,  $C_1 = C_2 = -1$ . The core polarization can be determined from the sense of rotation of the cores after excitation [27, 34]. The upward core in disk 1 gyrates counterclockwise, indicating  $p_1 = +1$ , whereas the downward core in disk 2 gyrates clockwise, corresponding to  $p_2 = -1$ .

In the serial images, the core positions of both disks can be determined by the variations of the in-plane curling magnetizations. The vortex-core oscillation around its center position in disk 1 (right disk) is excited by the local field of the strip line at the beginning of perturbation. The vortex gyration in disk 2, also shown in Fig. 5.2, is not excited by the local field, but is induced by the dipolar interaction between the two disks. Local fields produced through the Cu strip did not excite the neighboring disk, proven by experimental confirmation with a reference sample that contained only the disk beside the strip. As shown in Fig. 5.3, calculations confirm that the local fields emanating from the strip line can be neglected at

the position of the left disk. The in-plane component of the local fields is effective only in the one disk on which the Cu electrode is placed; the out-of-plane field component is too weak to affect vortex excitations.

The stray field from vortex state disk during gyrotropic motion is shown in Fig. 5.4. The stray field also rotates at same frequency with the vortex core but the rotation sense is opposite. The field strength is enough to excite the vortex motion in neighboring disk. The core positions varying in time and in in-plane space over a relatively large area are resolved in both disks. Correlations of the amplitudes and phases of both vortex-core positions can be easily identified with reference to the serial images.



**FIG. 5.2** Transmission XMCD images of dynamic evolution of vortex gyrotropic motions in both disks, and corresponding vortex states represented by color and height of the surface:  $p_1 = +1, p_2 = -1$  and  $C_1 = C_2 = -1$ . The dotted vertical and horizontal lines indicate the center position of each disk.

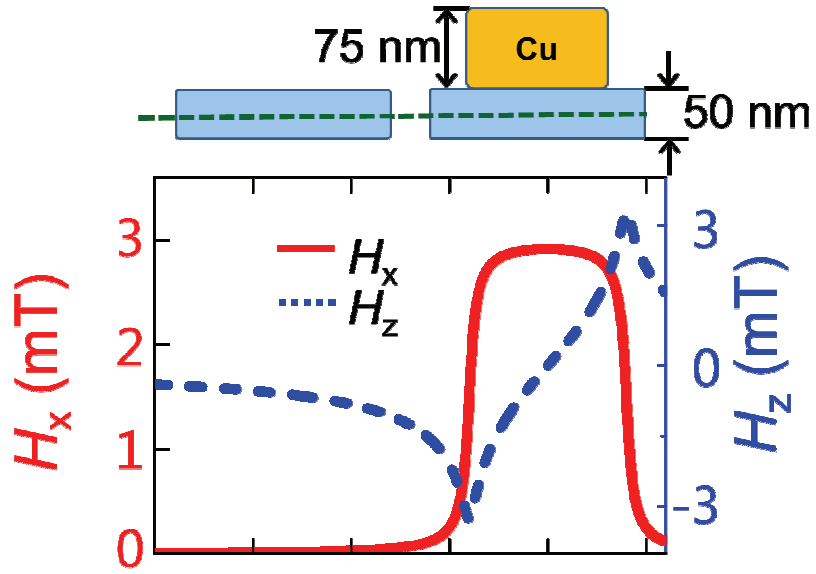


**FIG.5.3** Spatial distribution of the magnitude of magnetic fields generated from the Cu stripline. The profiles of the Oersted field were calculated for the center of the Py disk height using  $I = 8$  mA (current density =  $7.0 \times 10^6$  A/cm<sup>2</sup>).

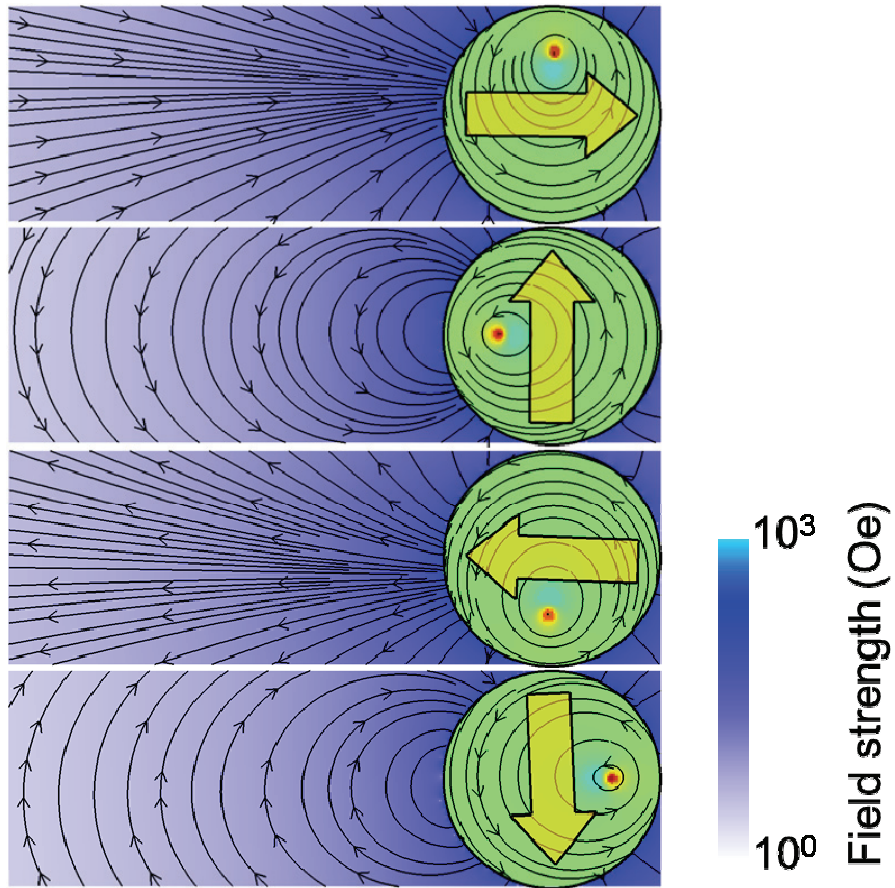


**FIG.5.4** Distribution of stray field emitted from a Py disk during gyration of upward vortex core. The results are obtained from micromagnetic simulation.



### 5.3 Dipolar induced vortex core oscillation

According to the vortex-core positions that evolve over time, the  $x$  and  $y$  components are plotted as functions of time in Fig. 5.5a. The components provide information about the correlations of the core orbit amplitudes and phases between the two gyrations. The  $x$  components in both disks show out-of-phase oscillations whereas the  $y$  components show in-phase ones, during the relaxation process after the short pulse field is turned off. The amplitudes of both core oscillations decrease due to their damping. The anti-phase relation along the  $x$  axis and the in-phase relation along the  $y$  axis reflect the core polarizations and the chiralities of both disks. The initial motion of the vortex core under the strip line is caused by the field pulse and depending on the chirality the vortex core moves in positive or negative  $y$  direction. The sense of core rotation is determined by the polarization  $p$ . The relative core positions change the effective stray field of each disk. The experimental results were confirmed to be in quantitative agreement with the simulation results for the same geometry and pulse parameters (shown in Fig. 5.5b). For micromagnetic simulation the OOMMF code was used [75]. The material parameters of the Py disks were as follows: the exchange stiffness  $A_{\text{ex}} = 13$  pJ/m, the saturation magnetization  $M_s = 7.2 \times 10^5$  A/m, with a zero magnetic anisotropy constant. The cell size was  $4 \times 4 \times 50$  nm<sup>3</sup> with the damping constant  $\alpha = 0.01$ . The estimated eigenfrequency from the vortex-core oscillations shown in Fig. 5.5a is about

143 MHz  $\pm$  14 MHz, which equals to the value obtained from the simulation. The uncertainty of the core position in Fig. 5.5a was about 33 nm, considering both the spatial and time resolutions of the measurement.

In summary, we employed 70-ps-time- and 20-nm-space-resolved, full-field magnetic transmission soft x-ray microscopy to simultaneously measure vortex-core positions in separated disks. The unique capabilities of time resolved full field magnetic soft X-ray microscopy allowed us to unambiguously resolve the individual vortex gyrations in both disks and to directly study their interaction. It was found that the vortex gyration of one disk affects that of the other through dipolar interaction. We investigated coupled vortex-state disks of the same clockwise in-plane curling magnetization and antiparallel core orientations. For this configuration, we observed out-of-phase (in-phase) oscillations of the vortex-core positions along the  $x$  axis ( $y$  axis). This work provides a robust and direct method of studying the dynamics of vortex gyrations and dipolar interaction in spatially separated disks.

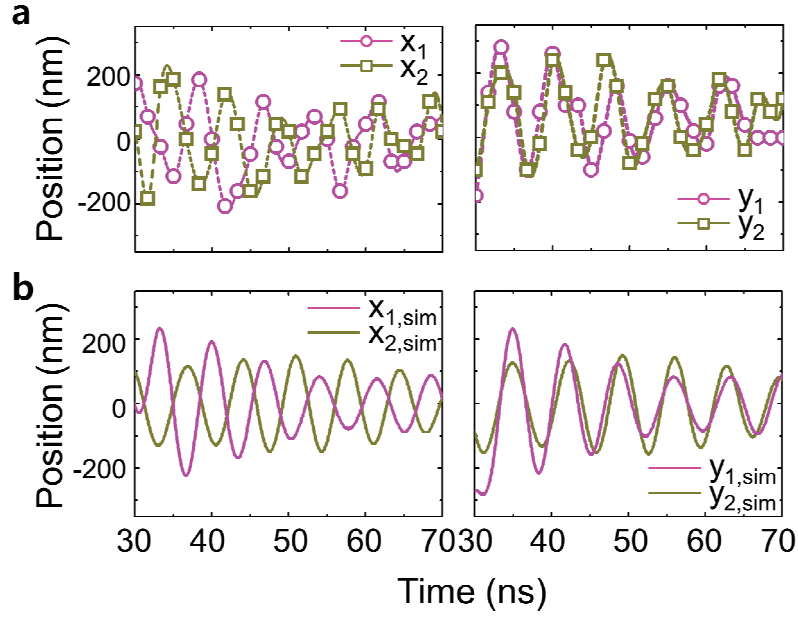


**FIG. 5.5** Oscillations of the  $x$  and  $y$  components of both vortex-core positions as function of time. (a) MTXM measurement results. The dashed lines were drawn using spline interpolation. (b) Micromagnetic simulation results for the same geometry and pulse parameters as those in the experiment.

## Chapter 6

### Energy Transfer through Vortex Core Gyration

In the previous chapter, coupled oscillation in two physically separated magnetic disks was directly observed. Various studies also showed vortex state elements can be coupled via magnetostatic interaction [76-81]. A displaced vortex core and its motion in one disk generate dynamically rotating stray fields, consequently affecting the potential energy of the other disk, in which vortex gyration can be stimulated resonantly. The relative vortex-core displacements in both disks as well as the disk-to-disk interdistance modify the interaction strength. This behaviour is analogous to coupled harmonic oscillators such as coupled pendulums or capacitively-coupled inductor-capacitor resonators [82]. Under the free-relaxation condition of such coupled oscillators, the kinetic and potential energy of one oscillator can be transferred to the other.

In the present chapter, we identify reliably controllable dipolar-coupled vortex-core oscillators by a direct experimental observation of a complete energy transfer and all of the collective normal modes. This mechanism is a robust means of tunable energy transfer and information-signal transport between physically separated magnetic disks, and provides for the advantages of negligible-loss energy transfer and low-power input signals using resonant vortex gyration.

## 6.1 Coupled oscillator

Before looking into the body of this chapter, it is necessary to consider the behaviour of coupled harmonic oscillators such as coupled pendulums or capacitively-coupled inductor-capacitor resonators. In one-dimensional (1D) coupled harmonic oscillators as shown in Fig 6.1 with the corresponding linear restoring force, the coupled motions of both oscillators can be expressed by a force balance equation,

$$m_i d^2 x_i / dt^2 = -\kappa x_i + k(x_j - x_i) \quad (6.1.1)$$

where  $m$ ,  $\kappa$ , and  $k$  are the mass, restoring force constant, and coupling force constant, respectively. The general solutions for the oscillators' displacements are given as

$$x_1(t) = A \cos(\omega_{low} t) + B \cos(\omega_{high} t), \quad (6.1.2a)$$

$$x_2(t) = A \cos(\omega_{low} t) - B \cos(\omega_{high} t), \quad (6.1.2b)$$

where A and B are constants that depend on the initial conditions. The frequencies of the in-phase and antiphase modes are given by  $\omega_{low} = \sqrt{\kappa / m}$  and  $\omega_{high} = \sqrt{(\kappa + 2k) / m}$ , respectively.

Under the free-relaxation condition of such coupled oscillators, the kinetic and potential energy of one oscillator can be transferred to the other. In the case of weak coupling, the displacements can be rewritten as

$$x_1(t) = A_0 \cos(\bar{\omega} t) \cos(\Delta \omega t / 2), \quad (6.1.3a)$$

$$x_2(t) = A_0 \sin(\bar{\omega} t) \sin(\Delta \omega t / 2) \quad (6.1.3b)$$

with the average frequency  $\bar{\omega} = (\omega_{high} + \omega_{low}) / 2$  and the frequency splitting  $\Delta\omega = \omega_{high} - \omega_{low}$  [83, 84]. These analytical expressions correspond to the beating pattern of simple harmonic coupled oscillators with no damping, as shown in Figs. 6.2.a-c. In Fig. 6.2.b, the total energy of the system is constant and the energy of each oscillator is transferred repeatedly between the two oscillators for the case of no damping. For the case of damped oscillation, the force balance equation can be rewritten as

$$m_i d^2 x_i / dt^2 + b dx_i / dt = -\kappa x_i + k(x_j - x_i) \quad (6.2.4)$$

with the damping term  $-b dx_i / dt$ . Thus, the displacements are given as

$$x_1(t) = A_0 \exp[-bt/(2m)] \cos(\bar{\omega}t) \cos(\Delta\omega t / 2), \quad (6.2.5a)$$

$$x_2(t) = A_0 \exp[-bt/(2m)] \sin(\bar{\omega}t) \sin(\Delta\omega t / 2). \quad (6.2.5b)$$

Calculations of the energy and displacement of the oscillators with damping are shown in Fig. 6.2.d. Comparing the cases of no damping with certain levels of damping (see Figs. 6.2.b and 6.2.d), it was found that some damping intrinsically results in mismatch between the nodes of one oscillator and the anti-nodes of the other. In many ways the coupling between vortex-state structures is analogous to discussed coupled harmonic oscillator.

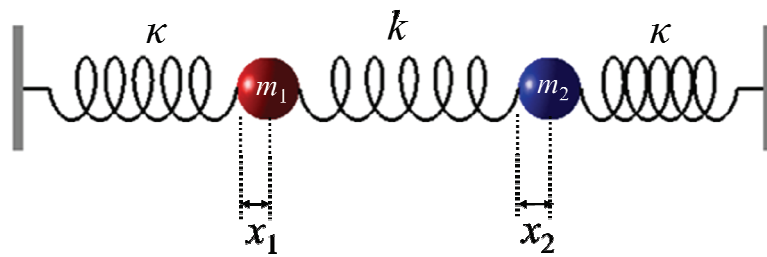


**FIG. 6.1** A system of coupled mass oscillators in one dimension. Two masses are connected by a spring to each other and by springs to fixed positions.

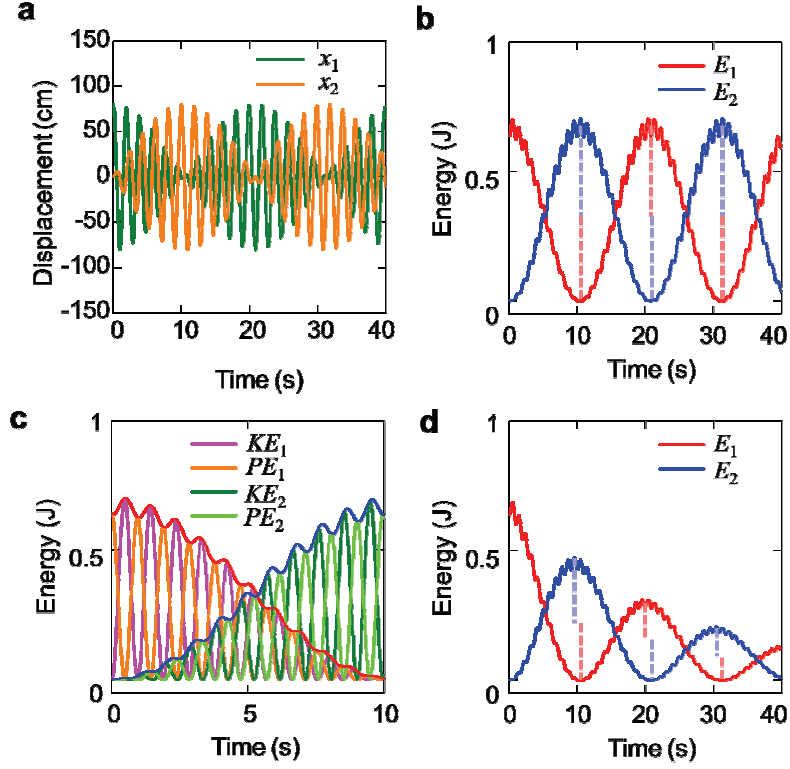


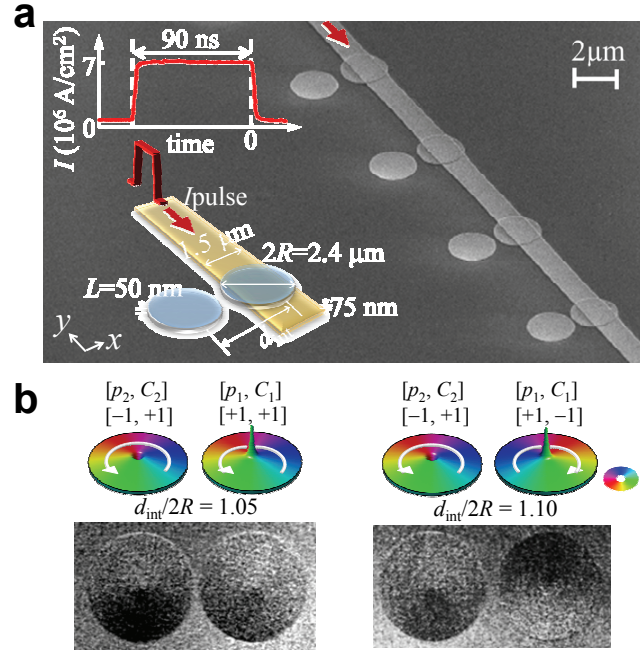
**FIG. 6.2** One-dimensional two coupled harmonic oscillators. The oscillators have an identical mass  $m = 0.2$  kg, restoring force constant  $\kappa = 2$  N/m, and coupling force constant  $k = 0.2$  N/m. The initial displacements of both oscillators are  $x_{1,0} = 80$  cm,  $x_{2,0} = 0$  cm. (a) Displacements of the oscillator positions. (b) Total energies of oscillators 1 and 2 as a function of time without damping. (c) Kinetic and potential energy oscillations of both oscillators. (d) Total energies of oscillators 1 and 2 as a function of time for a case of intrinsic damping,  $b/(2m) = 0.02$  Hz. In (b) and (d), the dashed vertical lines represent the nodes and anti-nodes of vortex-core oscillations.



## 6.2 Experimental observation of dipolar induced vortex gyrations

Figure 6.3 shows the sample, which contains several two-disk pairs, each of which consists of two Py disks of the same dimensions. Note that both disks are positioned on the  $x$  axis, which is referred to as the bonding axis. The dipolar interaction between the two disks along this axis breaks the radial symmetry of the potential well of both isolated disks. The procedure is similar to the experiment in previous chapter except for a different pulse field of 90 ns width and 30 Oe field, by which field, a different physical state was desired for the displacement of a vortex core only in disk 1 by a quasi-static field. Applying the pulse current along a single-strip Cu electrode (along the  $y$  axis) placed on only one disk (here denoted as disk 1), we shifted the core position in disk 1 to  $\sim 165$  nm in the  $+y$  direction from the center position  $(x_1, y_1) = (0,0)$ , and then allowed it to relax after turning off the field generated by the current pulse. During this free relaxation, the dynamics of the vortex gyrations in both disks of each pair were observed simultaneously, using spatiotemporal-resolved full-field MTXM. The magnetic contrast was provided via XMCD at the Fe  $L_3$  edge ( $\sim 707$  eV). Measurements were made on the basis of a stroboscopic pump-and-probe as described section 4.4 and 5.2. In previous chapter, the microscope of 70 ps temporal and 20 nm spatial resolution was used to resolve the phases and amplitudes of both vortex-core positions, for the purpose of a feasibility test of such a state-of-the-art experiment. Figure

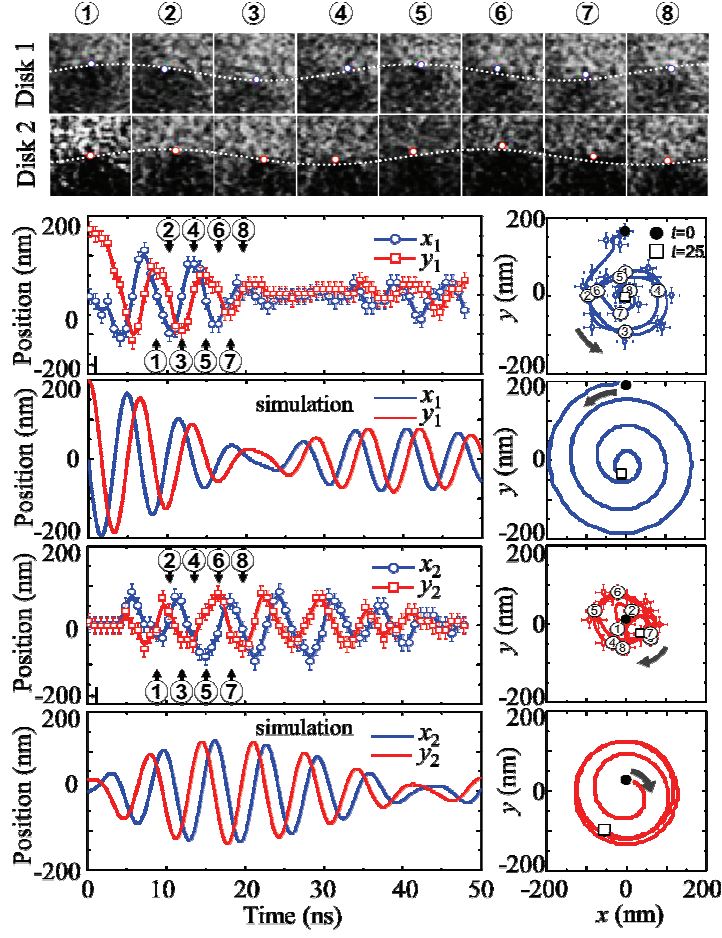
6.3.b shows the two pairs studied, that is,  $d_{\text{int}}/(2R) = 1.05$  and  $1.10$ , and includes simulation-perspective images of the initial vortex ground states in both disks. For the other pairs having larger  $d_{\text{int}}/(2R)$  values, the gyrations in disk 2 were difficult to observe, due to the small deviation of the vortex core from the center position, caused by the rapidly reduced interaction strength.



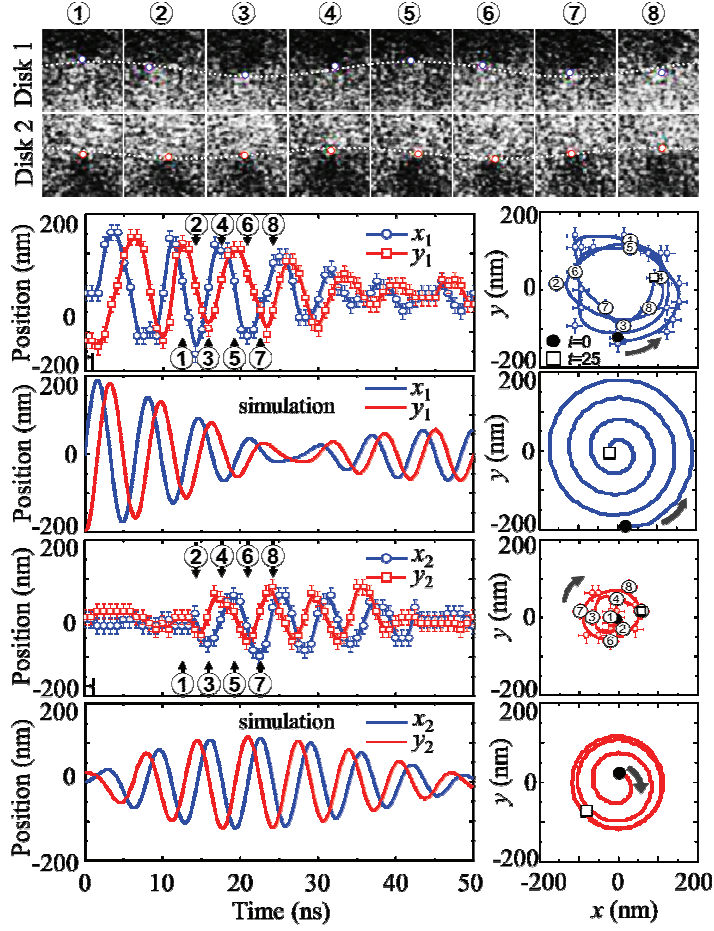
**FIG. 6.3** Sample geometry of pairs of two vortex-state disks and initial ground states. (a) Scanning electron microscopy image of sample containing several two-disk pairs. Each pair contains two Py disks of the same dimensions, as indicated in the inset. The center-to-center distance normalized by diameter  $d_{\text{int}}/(2R)$  varies, such that  $d_{\text{int}}/(2R) = 1.05, 1.1, 1.15, 1.2$ . Each pair is separated  $5.6$   $\mu$ m from the neighbouring pairs. The insets show schematic illustrations of the sample with the indicated dimensions and the employed current pulse of  $90$  ns width,  $2.5$  ns fall-and-rise time, and  $7.0 \times 10^6$  A/cm<sup>2</sup> current density. (b) Fe  $L_3$  edge XMCD images of both disks for two pairs,  $d_{\text{int}}/(2R) = 1.05$  and  $1.10$ , where initial ground states are represented by perspective-view simulation results, as indicated.

Figure 6.4 and 6.5 show the experimental data on the vortex gyrations in the two disks in both pairs:  $d_{\text{int}}/(2R) = 1.05$  and  $1.10$ , respectively. Representative serial snapshot images of the XMCD contrasts are shown in each top panel. The trajectory curves of the motions of both vortex-core position vectors,  $\mathbf{X}_1 = (x_1, y_1)$  and  $\mathbf{X}_2 = (x_2, y_2)$ , are plotted in the lower-right panels together with, in the lower-left panels, their oscillatory  $x$  and  $y$  components. Since a quasi-static local magnetic field (a pulse of sufficient length: here, 90 ns) was applied only to disk 1, the core position in that disk was shifted to  $(x_1, y_1) = (0, +165 \text{ nm})$  for  $[p_1, C_1] = [+1, +1]$  and to  $(x_1, y_1) = (0, -165 \text{ nm})$  for  $[p_1, C_1] = [+1, -1]$ . The opposite sign of the  $y$  displacement in disk 1 between  $d_{\text{int}}/(2R) = 1.05$  and  $1.10$  is attributable to the opposite chirality of disk 1 in the two pairs. Once the pulse field was turned off (at  $t = 0$ , the reference), the vortex core in disk 1 began to gyrate with decreasing oscillation amplitude starting from  $(x_1, y_1) = (0, +165 \text{ nm})$ , whereas the vortex core in disk 2 began to gyrate with increasing oscillation amplitude starting from  $(x_2, y_2) = (0, 0)$ . The vortex core in disk 1 gyrated counter-clockwise, indicating the upward core ( $p_1 = +1$ ) orientation, whereas the vortex core in disk 2 gyrated clockwise, corresponding to the downward core ( $p_1 = -1$ ) orientation (see Fig. 6.4). Figure 6.5 shows similar characteristic oscillations of the given vortex state configuration. We performed micromagnetic simulations of coupled vortex gyrations under free relaxation for two Py disks of the same dimensions as those of the sample

for  $d_{\text{int}}/(2R) = 1.05$  and  $1.10$ . To mimic the experimental conditions, we used the same initial vortex-state configurations as those of the real sample. The material parameters for Py are as follows: the exchange stiffness  $A_{\text{ex}} = 13$  pJ/m, the saturation magnetization  $M_s = 7.2 \times 10^5$  A/m, and a zero magnetic anisotropy constant. The cell size was  $4 \times 4 \times 50$  nm<sup>3</sup> with the damping constant  $\alpha = 0.01$ . We used the OOMMF code that utilizes the Landau-Lifshitz-Gilbert equation of motion. Micromagnetic simulation results are in excellent agreements with the experimental one, except for small discrepancies of their frequencies and absolute amplitudes. Experimental results show smaller oscillation amplitudes and frequencies, which might be attributed to the imperfection of the sample and weaker interaction between both disks due to a possible reduction in the saturation magnetization of the sample.



**FIG. 6.4** MTXM observation of vortex-core gyrations in dipolar-coupled Py disks for  $d_{\text{int}}/(2R) = 1.05$ , compared with the corresponding simulation results. The first row, are serial snapshot XMCD images of temporal evolution of vortex-core gyrations, starting from  $t = 8.8$  ns (①) and ending at  $t = 19.7$  ns (⑧). The second (disk 1) and fourth (disk 2) row are experimental results of the  $x$  and  $y$  components of vortex-core positions (left) from center position  $(x, y) = (0, 0)$ , and constructed vortex-core trajectories (right). The third and fifth rows indicate the corresponding simulation results.



**FIG. 6.5** MTXM observation of vortex-core gyrations in dipolar-coupled Py disks for  $d_{\text{int}}/(2R) = 1.10$ , compared with the corresponding simulation results. The first row, are serial snapshot XMCD images of temporal evolution of vortex-core gyrations, starting from  $t = 12.5$  ns (①) and ending at  $t = 24.2$  ns (⑧). The second (disk 1) and fourth (disk 2) row are experimental results of the  $x$  and  $y$  components of vortex-core positions (left) from center position  $(x, y) = (0, 0)$ , and constructed vortex-core trajectories (right). The third and fifth rows indicate the corresponding simulation results.

### 6.3 Energy transfer between two dipolar-coupled vortex oscillators

The most important finding here is that the vortex-core gyration in disk 2 is stimulated by the vortex-core gyration in disk 1, not by any external driving force or pulse field, but rather through the magnetostatic interaction between the two disks. For the case of  $d_{\text{int}}/(2R) = 1.05$ , the decreasing amplitude in disk 1 started to increase again at the time  $t = 26$  ns, whereas the increasing amplitude in disk 2 began to decrease (see Fig. 6.4). For  $d_{\text{int}}/(2R) = 1.10$ , the amplitude decay in disk 1 occurs at a longer time,  $t = \sim 45$  ns (see Fig. 6.5). Since the magnetic potential energy of a vortex depends on the displacement of the vortex core from the disk center, a complete energy transfer between dipolar-coupled vortex-state disks can be observed directly, via the variations of the displacements of both vortex cores, that is,  $|\mathbf{X}_1|$  and  $|\mathbf{X}_2|$ , as shown in Fig. 6.6. Such a crossover in the vortex-core gyration modulation envelope between disks 1 and 2 confirms that the energy stored via the displaced core by an input-signal pulse field is transferred from disk 1 to disk 2 through the robust mechanism of stimulated vortex gyration in dipolar-coupled vortex oscillators. The high efficiency of this energy transfer mechanism is evidenced by the low (almost zero) amplitudes at the nodes of the beating pattern of the coupled vortex oscillators. Note that the mismatch between the nodes of the vortex-gyration amplitude in one disk and the anti-nodes in the other disk results from the intrinsic damping of a given material as discussed in Section 6.1.



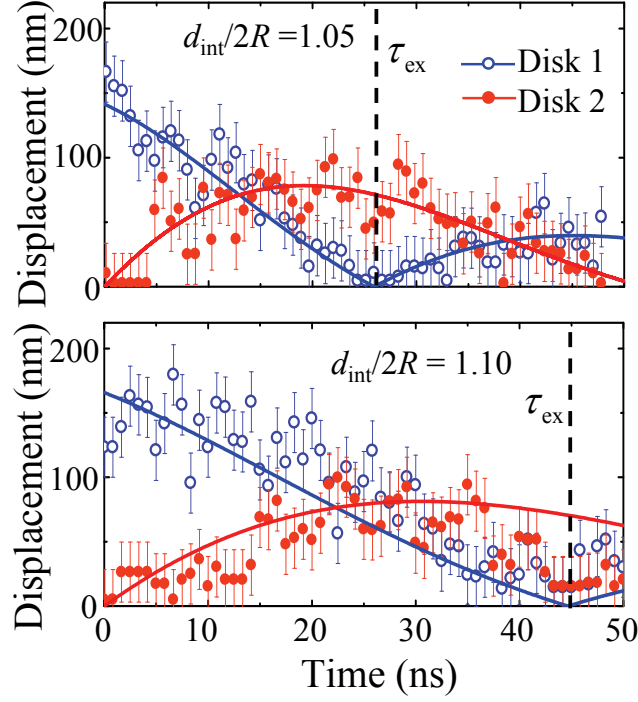


**FIG. 6.6** Comparison of vortex-core displacement variations versus time in both disks for  $d_{\text{int}}/(2R) = 1.05$  and  $1.10$ . The open and closed circles represent the experimental results for disks 1 and 2, respectively. The thick solid curves are the results of the fits to  $|\mathbf{X}_1| = |A \cos(\Delta\omega t/2)| \exp(-\beta t)$  and  $|\mathbf{X}_2| = |A \sin(\Delta\omega t/2)| \exp(-\beta t)$ , where amplitude  $A = 141 \pm 12$  nm, damping coefficient  $\beta = 2\pi \times (4.2 \pm 0.7)$  MHz,  $\Delta\omega = 2\pi \times (19.3 \pm 2)$  MHz for  $d_{\text{int}}/(2R) = 1.05$  and  $A = 166 \pm 15$  nm,  $\beta = 2\pi \times (3 \pm 0.7)$  MHz, and  $\Delta\omega = 2\pi \times (11.2 \pm 1.5)$  MHz for  $d_{\text{int}}/(2R) = 1.10$ . The vertical lines correspond to the rate of energy transfer between the two disks:  $\tau_{\text{ex}} = \frac{1}{2}(2\pi / \Delta\omega)$ .

The total energy of undamped coupled oscillators, which is the sum of the first and second oscillator energies and the interaction energy between the oscillators, is constant. Magnetic vortices typically reside in potentials, which give rise to corresponding eigenfrequencies up to  $\sim 1$  GHz. However, in principle these frequencies can be modified in virtually any desired frequency range, which is an important and advantageous aspect of the application of coupled vortex oscillators. As in every coupled harmonic oscillator system, the original resonance frequency of the non-interacting oscillator is either enhanced or reduced by the coupling [82]. Generally a symmetric and an antisymmetric mode having a lower and a higher frequency compared with the original eigenfrequency in uncoupled disks, respectively, appear. The frequency splitting between the symmetric and antisymmetric modes have a direct correlation with the interaction energy, and can be deduced from the beating pattern of coupled oscillations (see section 6.1). It is clear that such a modulation envelope crossover between disks 1 and 2, as demonstrated in Figs. 6.4-6.6, is the result of the superposition of two equally weighted normal modes of different frequencies excited in a given dipolar-coupled oscillator system. The beating frequency  $\Delta\omega$  of the modulation envelope functions in disk 1 and disk 2 can be obtained by fitting the data of  $|\mathbf{X}_1|$  and  $|\mathbf{X}_2|$  to two orthogonal sinusoidal functions with a damping term,  $|\mathbf{X}_1| = |A \cos(\Delta\omega t/2)| \exp(-\beta t)$  and

$|\mathbf{X}_2| = A \sin(\Delta\omega t/2) \exp(-\beta t)$ :  $\Delta\omega/2\pi = 20$  MHz and 12 MHz for  $d_{\text{int}}/(2R) = 1.05$  and 1.10, respectively. These results agree well on the fact that this angular frequency splitting  $\Delta\omega$  takes place according to interaction between oscillators in a coupled system and the magnitude of  $\Delta\omega$  varies with the interdistance between neighboring oscillators. The fit function can be derived analytically from simultaneous Thiele's equations of motion of magnetization [85]. The energy exchange time  $\tau_{\text{ex}}$  between oscillators is technologically important from the information-signal transport point of view. It is determined by the coupling strength. Let  $\tau_{\text{ex}}$  be the time period required for transferring the potential energy stored in disk 1 (here, due to the initial vortex-core shift) completely to disk 2.  $\tau_{\text{ex}}$  can be estimated from the frequency splitting determined from the modulation envelopes of  $|\mathbf{X}_1|$  and  $|\mathbf{X}_2|$ , and consequently, is given as half of the modulation envelope period,  $\frac{1}{2}(2\pi / \Delta\omega)$ , so that  $\tau_{\text{ex}} = 26 \pm 3$  ns and  $45 \pm 6$  ns for  $d_{\text{int}}/(2R) = 1.05$  and 1.10, respectively. Since the strength of the interaction between two vortices determines the frequency splitting of dipolar-coupled vortices, a smaller value of  $\tau_{\text{ex}}$  can be obtained by increasing the strength of the dipolar interaction. For any given material and vortex state, it is known that the dipolar interaction between two vortices depends very strongly on the interdistance between them [42, 72]. This was confirmed by the present experiments. Accordingly, the energy transfer rate between vortex-state disks

is tunable varying their interdistance.

Another important parameter is  $\beta$ , which represents the energy loss during vortex-gyration-mediated signal propagation through next-neighbouring disks. Based on Thiele's equation of vortex-core motion, the attenuation parameter is expressed analytically as  $\beta = -(D/G)\omega_0$  in an isolated disk with the gyrovector constant  $G$  and the damping constant  $D$  [27]. This parameter can be rewritten as  $\beta = \frac{1}{2}\alpha[2 + \ln(R/R_c)]\omega_0$  with the intrinsic damping constant  $\alpha$  and the vortex-core radius  $R_c = 0.68L_{ex}(L/L_{ex})^{1/3}$  where the dot thickness  $L$  and the exchange length  $L_{ex} = (2A_{ex}/M_s^2)^{1/2}$  with the exchange stiffness  $A_{ex}$  and the saturation magnetization  $M_s$ . For the case of experimentally obtained value of  $\alpha = 0.01 \pm 0.002$  [86-88] for a given material Py and the eigenfrequency  $\omega_0 = 2\pi \times (157 \pm 3)$  MHz for isolated Py disks of  $R = 1.2 \mu\text{m}$  and  $L = 50$  nm, the value of  $\beta = 2\pi \times (4.81 \pm 1.05)$  MHz is found to be in good agreement with the values of  $\beta$ ,  $2\pi \times (4.2 \pm 0.7)$  MHz and  $2\pi \times (3.0 \pm 0.7)$  MHz for  $d_{\text{int}}/(2R) = 1.05$  and  $1.10$ , respectively, which are obtained from fits to the experimental data shown in Fig. 6.6. Such good agreements are strong proof that energy loss through vortex-gyration-mediated signal transfer is determined by the intrinsic damping constant and dimensions of a given material. This means that further reduction of attenuation can be achieved by

material engineering. The energy attenuation will be discussed in following Section 6.9.

#### 6.4 Normal modes representation of coupled vortex oscillations

To directly obtain the value of  $\Delta\omega$  from the experimentally observed vortex gyrations in the coupled system, we transformed the  $x$  and  $y$  component oscillations in each disk into two normal-mode oscillations on the basis of normal-mode coordinates  $(NI_X, NI_Y) = (x_1+x_2, y_1-y_2)$  and  $(N2_X, N2_Y) = (x_1-x_2, y_1+y_2)$  for the case of  $p_1 p_2 = -1$ . In the normal-mode representation, the experimentally observed vortex gyrations in real coordinates  $(x, y)$  were decoupled into two normal modes having corresponding single dominant frequencies, as shown in Fig. 6.7 and 6.8. Figures 6.7a reveals that the two normal modes were excited almost equally and that their amplitudes were damped monotonically, as in free-relaxation vortex-core gyrations in uncoupled disks. According to their FFT spectra in Fig. 6.7b, the lower and higher eigenfrequencies for the two normal modes were  $145 \pm 10$  and  $165 \pm 10$  MHz, and thus, their frequency splitting was  $\Delta\omega/2\pi = 20$  MHz for  $d_{int}/2R = 1.05$ , which is in excellent agreement with the values obtained from the fit to the modulation envelope functions of  $|\mathbf{X}_1|$  and  $|\mathbf{X}_2|$  with the corresponding damping (Fig. 6.6).

Moreover, we can decompose coupled vortex gyrations into the two normal modes of each disk with respect to the ordinary coordinates according to the relations of  $(x_1, y_1)_{NI} = \frac{1}{2}(NI_X, NI_Y)$ ,  $(x_1, y_1)_{N2} = \frac{1}{2}(N2_X, N2_Y)$ ,  $(x_2, y_2)_{NI} = \frac{1}{2}(NI_X, -NI_Y)$ , and  $(x_2, y_2)_{N2} = \frac{1}{2}(-N2_X, N2_Y)$ . Figure 6.7c shows results showing that for the higher-frequency  $N$

$I$  mode, the  $x$  positions of the vortex-core motions in both disks oscillate in-phase but their  $y$  positions do so out-of-phase, and vice-versa for the lower-frequency  $N2$  mode. Since the vortex-core motion in one disk in the direction normal to the bonding axis (i.e., along the  $y$  axis) results in stronger stray fields (exciting vortex motion in the other disk) than it does along the bonding axis (the  $x$  axis), the dipolar interaction is dominated by the relative  $y$  position of vortex-core motions between the two disks. Thus, the interaction energy of the  $N1$  mode having out-of-phase oscillation at the  $y$  positions is higher than that of the  $N2$  mode having in-phase oscillation at the  $y$  positions. Analogous to a general coupled harmonic oscillator, the  $N1$  mode with the antisymmetric  $y$  component oscillation *works harder* than the  $N2$  mode with the symmetric one. As the result, the frequency of the  $N1$  mode is higher than that of the  $N2$  mode, as noted earlier. More generally in two dipolar coupled disks with an arbitrary relative state of the  $p$  and  $C$  configuration, the mode with out-of-phase oscillation between  $C_1y_1$  and  $C_2y_2$  is the antisymmetric mode with the higher frequency and the mode with their in-phase relation is the symmetric one with the lower frequency. This is because the direction of the stray fields induced by vortex-core shifts depends on  $C$  and thus, the interaction energy of each mode is determined by the relative chirality configuration between the two coupled vortices. Figure 6.8 is a normal-mode representation

of the experimentally observed coupled vortex gyrations under free relaxation for the case  $d_{\text{int}}/(2R) = 1.10$ . Compared with the case of  $d_{\text{int}}/(2R) = 1.05$ , the interaction, as discussed in the main text, is relatively weak. Thus, the frequency splitting for  $d_{\text{int}}/(2R) = 1.10$  is smaller than that for 1.05. In the frequency spectra, the frequencies for both normal modes are close to each other, and thus, due to the limited experimental resolution in the present case, were not resolved.



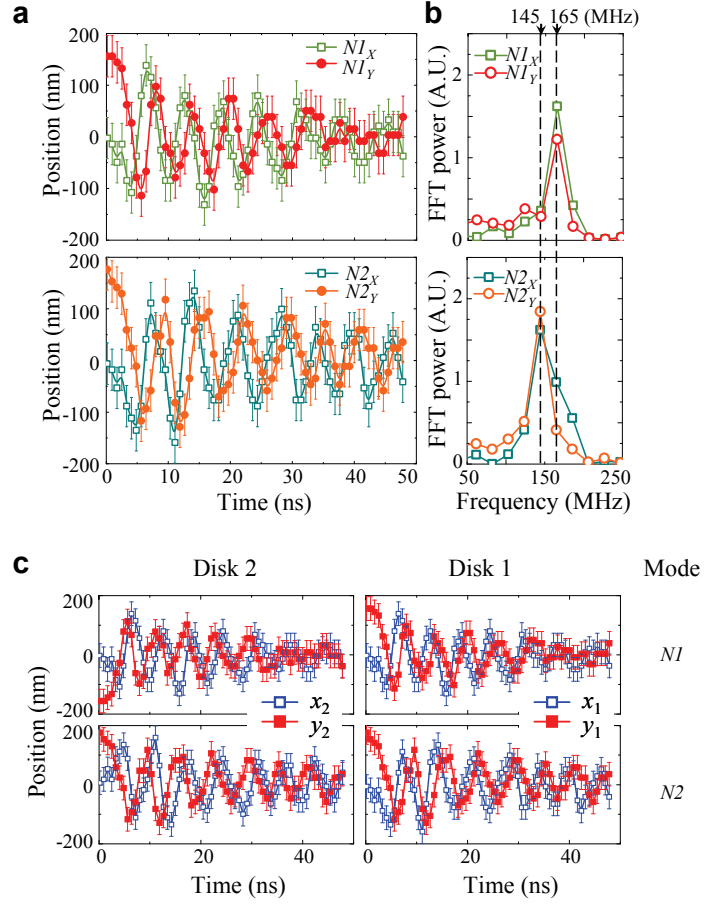


**FIG. 6.7** Normal-mode representations of vortex-core gyrations in dipolar-coupled oscillators for  $d_{\text{int}}/(2R) = 1.05$ . (a) Oscillatory core motions and (b) dominant frequency spectra. The two normal-mode coordinates are represented as ( $N1_x = x_1 + x_2$ ,  $N1_y = y_1 - y_2$ ) and ( $N2_x = x_1 - x_2$ ,  $N2_y = y_1 + y_2$ ), corresponding to their trajectory curves and FFT spectra. **c.** The  $x$  and  $y$  positions of vortex-core oscillations in each disk for each normal mode (see the text).

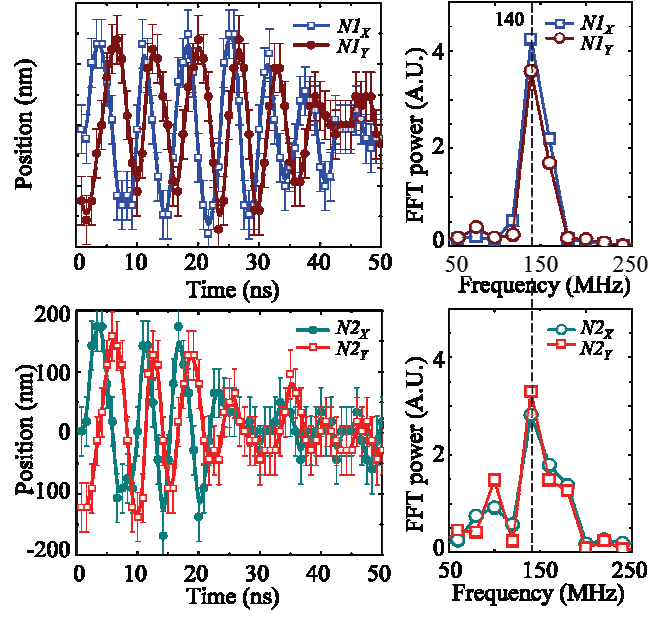


**FIG. 6.8** Normal-mode representation of vortex-core gyrations in a real sample of  $d_{\text{int}}/(2R) = 1.10$ . Oscillations of both components with respect to the normal-mode coordinates (left) and frequency spectra (right). The normal-mode coordinates used were ( $NI_x = x_1 + x_2$ ,  $NI_y = y_1 - y_2$ ) and ( $N2_x = x_1 - x_2$ ,  $N2_y = y_1 + y_2$ ).

## 6.5 Micromagnetic simulation procedure and results

Micromagnetic simulations of coupled vortex gyrations was performed under free relaxation for several pairs of Py disks of different center-to-center distances  $d_{\text{int}}/(2R)$ . We used the OOMMF code that utilizes the Landau-Lifshitz-Gilbert (LLG) equation of motion. The dimensions of the Py disks were  $2R = 300$  nm,  $L = 20$  nm. Various  $d_{\text{int}}/(2R)$  values ranging from 1.01 to 2.5 have been chosen. The diameter chosen was smaller than that of the real sample so as to reduce the computational time.

Figure 6.9a depicts the initial vortex states, which are the same as those of the real sample ( $p_1 = +1, p_2 = -1, C_1 = C_2 = -1$ ). To mimic the experimental conditions, we displaced the initial vortex-core position of disk 1 to  $-37.5$  nm in the  $y$  axis, by applying a static field of  $+15$  mT along the  $x$  axis and then allowing it to relax. This displaced vortex core showed a CCW spiral motion with decreasing amplitude (Fig. 6.9b, right). In contrast, the vortex core initially positioned at the center of disk 2 gyrated in a CW sense with increasing amplitude (Fig. 6.9b, left). Figure 6.9c plots the oscillatory  $x$  and  $y$  components of the vortex-core positions in both disks under free relaxation, indicating not only higher- but also lower-frequency oscillations, along with modulation envelopes, in analogy to the beating patterns that result from the superposition of two modes of slightly differing frequencies in classical coupled harmonic oscillators with damping. The higher ( $\omega_{\text{high}}/2\pi = 620$  MHz) and lower ( $\omega_{\text{low}}/2\pi = 535$  MHz) frequencies of the

coupled vortex gyrations in both disks, as obtained from fast Fourier transforms (FFTs) of the oscillatory core position vectors, were clearly evident, as shown in Fig. 6.9d. The angular frequency splitting  $\Delta\omega = \omega_{high} - \omega_{low}$  is known to be caused by dipolar interaction between the two separated vortex oscillators. In isolated single-vortex-state disks, the eigenfrequency is calculated to be 580 MHz, which is close to the average over those higher and lower frequencies.

In the plots of the modulation envelopes (open symbols) of the displacements of the vortex-core position vectors,  $|\mathbf{X}_1|$  and  $|\mathbf{X}_2|$  (Fig. 6.9e), their local minima and maxima in both disks exhibit the anti-phase relation. The potential energies for the displaced vortex-core positions, as a function of time, are plotted in Fig. 6.9f. The potential energy for the vortex core initially displaced to 37.5 nm in disk 1 is transferred by the vortex gyration which stimulates disk 2's gyration through dipolar coupling. This energy transfer takes place repetitively, as evidenced by the repeated emergences of the local maxima and minima of the potential energies as well as the core position oscillations in both disks.

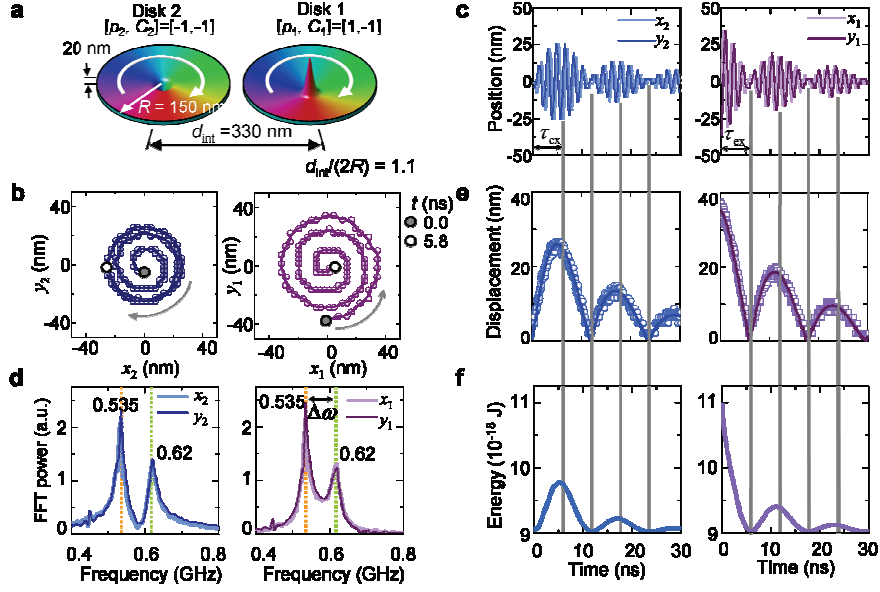


**FIG. 6.9** Simulation results of vortex gyrations in dipolar-coupled vortex-state disks during the free relaxation from the indicated initial state. The dimensions of both Py disks are as follows: normalized center-to-center interdistance  $d_{\text{int}}/(2R) = 1.10$ , diameter  $2R = 300$ , and thickness  $L = 20$  nm. The vortex core in disk 1 is displaced to  $(x_1, y_1) = (0, -37.5$  nm) by a static field  $H_x = +15$  mT. (a) The initial vortex states of both disks are represented by  $[p_1, C_1] = [1, -1]$  and  $[p_2, C_2] = [-1, -1]$ . (b) Trajectories of vortex-core motions. The initial vortex-core positions in both disks are indicated by closed dots. (c) Oscillatory  $x$  and  $y$  components of vortex-core position vectors, (d) FFT power spectra as a function of frequency obtained from the oscillatory  $x$  and  $y$  components up to  $t = 200$  ns. (e) Displacement modulations. (f) Potential energy variation versus time in both disks.

## 6.6 Frequency splitting and energy transfer rate

A beating pattern in a simple coupled harmonic oscillator contains information on the frequency splitting caused by coupling between the individual oscillators. Thus, the frequency splitting can be determined by fitting the modulation envelopes of the vortex-core displacements in both disks (Fig. 6.9e) to the corresponding envelope functions, here  $\cos(\Omega t/2)$  and  $\sin(\Omega t/2)$  in disks 1 and 2, respectively, with the attenuation term,  $\exp(-\beta t)$ . The solid lines in Fig. 6.9e are the fitting results. Accordingly, the value of  $\Delta\omega$  is equal to that of  $\Omega$  obtained from the fitting result.  $\Delta\omega = \Omega$  is directly related to the exchange time  $\tau_{ex}$  of energy transfer, which is defined as the time period required for transferring the stored energy in one oscillator completely to the other one:  $\tau_{ex} = \pi / \Delta\omega$ . For the case, the value was estimated to be  $\tau_{ex} = \pi / \Omega = 5.9$  ns.

## 6.7 Dependence on interdistance

Since a dipolar interaction between separated magnetic disks changes with their interdistance, the frequency splitting caused by the interaction also varies with  $d_{\text{int}}/(2R)$ . Figure 6.10a shows the frequency spectra obtained from the FFTs of the oscillatory vortex-core motions for different values of  $d_{\text{int}}/(2R)$  ranging between 1.01 and 2.5. For the cases of  $d_{\text{int}}/(2R) > 2.5$ , owing to the negligible dipolar interaction between the two disks, there exists a single eigenfrequency  $\omega_0$  for isolated disks. However, as  $d_{\text{int}}/(2R)$  decreases, the single peak is separated into two dominant peaks, higher and lower frequencies, both of which appear in each disk. The higher frequency increases (blue shift), whereas the lower one decreases (red shift); consequently as a result of the stronger dipolar interaction,  $\Delta\omega$  increases with decreasing interdistance,

From the fits of the modulation envelopes,  $|\mathbf{X}_1|$  and  $|\mathbf{X}_2|$ , the beating frequency as a function of interdistance also can be determined, as shown in Fig. 6.10b. As the value of  $d_{\text{int}}/2R$  decreases, the  $\Omega$  increases, thus  $\tau_{\text{ex}} = \pi/\Omega$  becomes shorter. Figure 6.11 shows a comparison of  $\Delta\omega/2\pi$  and  $\Omega/2\pi$ , where, as a function of  $d_{\text{int}}/(2R)$ , they agree well. The result clearly show that the value of  $\tau_{\text{ex}}$  varies with the interdistance as

$$\tau_{\text{ex}} \sim (d_{\text{int}}/2R)^{3.91 \pm 0.07}.$$

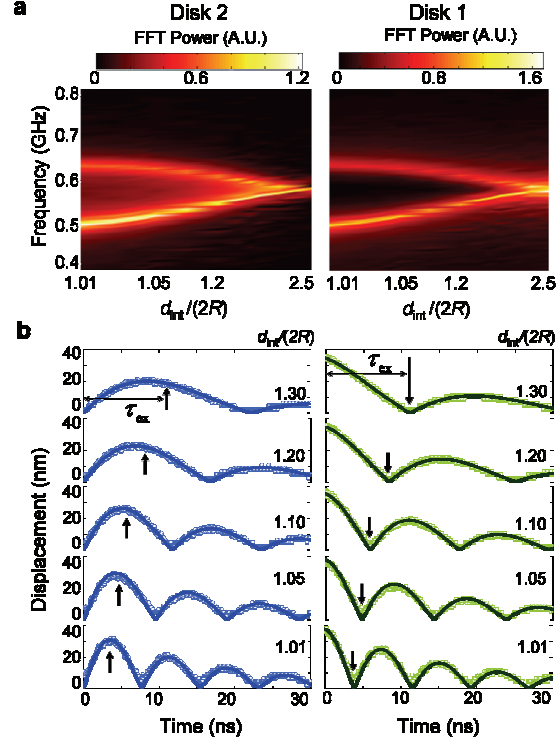


**FIG. 6.10** Frequency splitting and modulation envelopes for different  $d_{\text{int}}/(2R)$  values. (a) Frequency splitting directly obtained from the oscillatory x and y components of vortex-core positions via FFTs. (b) Modulation envelopes of vortex-core displacements versus time for indicated different values of  $d_{\text{int}}/(2R)$ . The thick solid curves are the results of fits to the simulation data (open circles) using  $|\mathbf{X}_1| = |A \cos(\Omega t/2)| \exp(-\beta t)$  for disk 1 and  $|\mathbf{X}_2| = |A \sin(\Omega t/2)| \exp(-\beta t)$  for disk 2, where  $A$  is the initial displacement of the vortex-core in disk 1, the oscillating frequency  $\Omega$ , and the attenuation parameter  $\beta = 2\pi \times 9$  MHz. The vertical arrows represent the exchange time of energy transfer between the two disks,  $\tau_{\text{ex}} = \pi/\Omega$ .



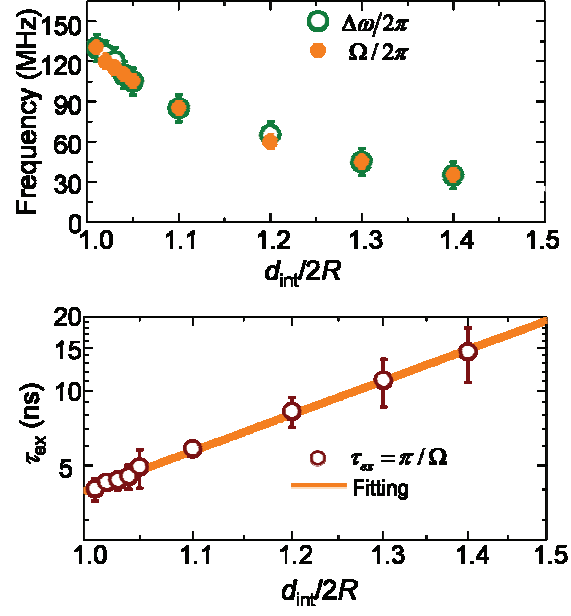


**FIG. 6.11** Frequency splitting and exchange time of energy transfer versus  $d_{\text{int}}/2R$ . For the calculation of  $\tau_{\text{ex}}$ , the relation of  $\tau_{\text{ex}} = \pi / \Omega$  was used. The orange solid line is the result of a fit to the simulation data using  $\tau_{\text{ex}} \sim (d_{\text{int}}/2R)^m$ , where  $m = 3.91 \pm 0.07$ .

## 6.8 Dependence on relative vortex polarization

It is worth noting that the relative motion of the vortex-core gyration of two vortices also affects the strength of their interactions: the dipolar interaction of vortex-core gyrations having opposite rotation senses due to opposite polarities is much stronger than that of gyrations having the same rotation sense due to the same polarity.

As shown in Fig. 6.12, the vortex-core gyrations were distinctly different; the energy transfer rate for the same polarization was two times slower ( $\tau_{ex} = 10.6$  ns) than that ( $\tau_{ex} = 4.9$  ns) for the opposite polarization. When the cores gyrate at their own  $\omega_D$ , the stray fields also rotate at the same frequency as  $\omega_D$ . For the case of upward core with the counter-clockwise (CCW) rotational sense, the net resulting stray field is a clockwise (CW) rotating field. As reported earlier [24, 34, 89], the application of CW rotating fields of  $\omega_H = \omega_D$  leads to resonant excitations for the down core but no-excitations for the up core. In here, even though the amplitude is small, the motion of down core can be also excited because the resulting stray field is not perfectly circularly rotating fields.

Because the polarity of a given vortex can be manipulated in a controllable manner by applying rotating or pulse fields locally to that vortex state using specially designed electrodes, as reported in Refs. [90, 91], the polarities of vortices can be one of the crucial parameters for governing the interaction strength of energy transfer, and hence the exchange time.

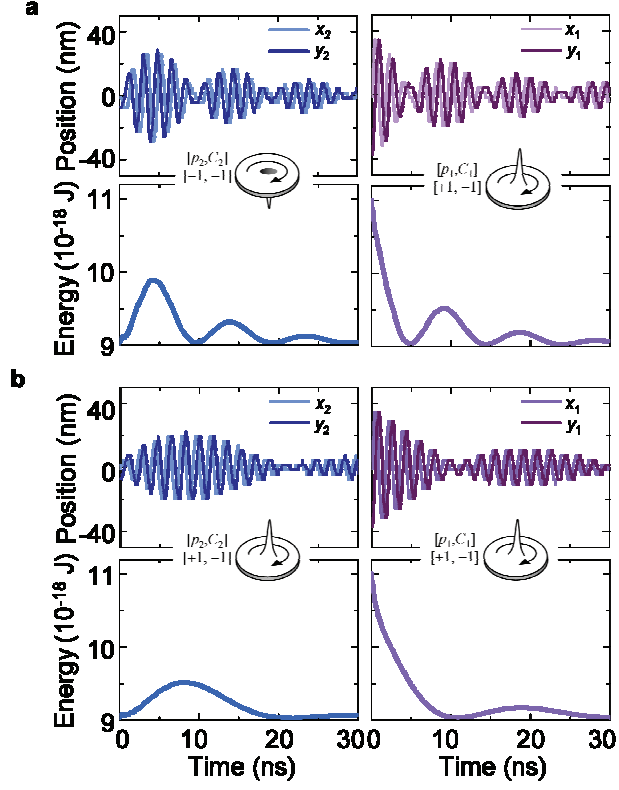


**FIG. 6.12** Comparisons of coupled vortex gyrations between different polarization configurations,  $p_1 p_2 = -1$  in (a) and  $+1$  in (b). Simulation results of oscillations of the  $x$  and  $y$  components of vortex-core motions and the modulations of potential energies in both Py disks of  $2R = 300$  nm,  $L = 20$  nm, and  $d_{\text{int}}/(2R) = 1.05$ .

## 6.9 Energy attenuation

The energy attenuation during vortex-gyration-mediated signal transfer can be represented by the ratio of the maximum amplitude of oscillation of disk 2 to that of disk 1. On the basis of the analytical forms of  $|\mathbf{X}_1| = |A \cos(\Omega t/2)| \exp(-\beta t)$  and  $|\mathbf{X}_2| = |A \sin(\Omega t/2)| \exp(-\beta t)$  with the values of  $[\Omega, \beta] = 2\pi \times [19.3 \pm 2, 4.2 \pm 0.7]$  MHz for  $d_{\text{int}}/(2R) = 1.05$  obtained from fits of the modulation envelopes to the experimental data as a function of time, we determined  $|\mathbf{X}_2|_{t=\tau_{\text{ex}}} / |\mathbf{X}_1|_{t=0} = \exp(-\pi\beta / \Omega) = 0.5$  with  $\pi\beta / \Omega = 0.68$ . The result shows a relatively high attenuation of energy.

To achieve lossless energy transfer using negligible damping materials, we conducted simulations on two-disk pairs of different materials, Py and NiMnSb, and of much smaller dimensions,  $2R = 201$  nm,  $L = 6$  nm, and  $d_{\text{int}}/(2R) \sim 1.04$ . The material, NiMnSb, has a relatively low damping constant,  $\alpha = 0.0023$ , compared with  $\alpha = 0.01$  for Py. For the material parameters of NiMnSb, we used the exchange stiffness  $A_{\text{ex}} = 10$  pJ/m, the anisotropy constant  $K = -1 \times 10^5$  J/m<sup>3</sup>, and the saturation magnetization  $M_s = 549 \times 10^3$  A/m. As can be seen in Fig. 6.12, the fitting results for such reduced dimensions are  $[\Omega, \beta] = 2\pi \times [60 \pm 1, 5 \pm 0.1]$  MHz for Py and  $[\Omega, \beta] = 2\pi \times [46 \pm 1, 0.8 \pm 0.1]$  MHz for NiMnSb. From those values, we can estimate the value of  $|\mathbf{X}_2|_{t=\tau_{\text{ex}}} / |\mathbf{X}_1|_{t=0} = \exp(-\pi\beta / \Omega)$ , here, 0.77 for Py and 0.95 for NiMnSb. The high value for NiMnSb allows for a sufficiently

low attenuation of energy transfer by stimulated vortex gyration. As explained in Section 6.3, this reduction is due only to the intrinsic magnetic damping of a given material. The degree of the attenuation varies remarkably with the dimensions of the model system and with the material used. This fact allows for a significant reduction of energy attenuation to be achieved by means of low-damping-constant, smaller-dimension material and shorter interdistances between neighboring disks. Some Heusler alloys are reported to have extremely small values of  $\alpha$ , for instance,  $\alpha = 0.00006$  for  $\text{Co}_2\text{MnSi}$  as found from an *ab initio* calculation [92] and  $\alpha = 0.001$  for  $\text{Co}_2\text{FeAl}$  as obtained from ferromagnetic resonance measurement [93]. Dependence of controllable indexes  $\tau_{ex}$  and  $\beta$  on variables (e.g. polarization of vortices, interdistance between disks, and damping constant of materials) is summarized in Table 6.1.

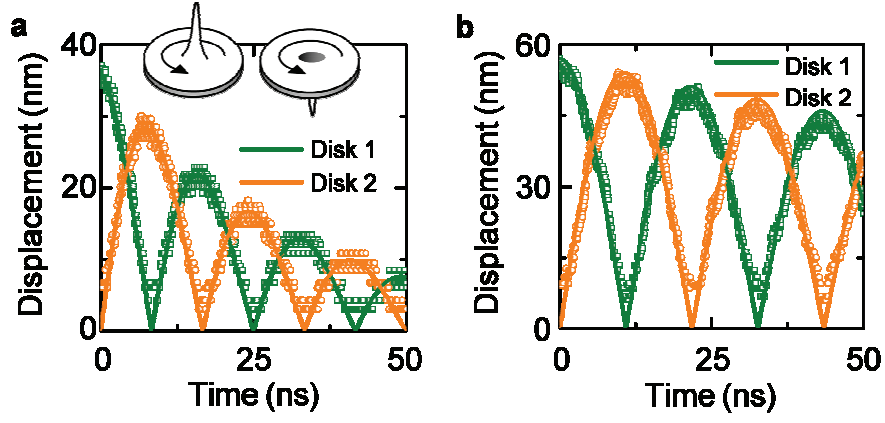


**FIG. 6.13** Modulation envelopes of vortex-core displacements versus time for Py in (a) and NiMnSb in (b). The open dots indicate the simulation results, which are compared with the analytical equations (solid lines)

$$|X_1| = |A \cos(\Omega t/2)| \exp(-\beta t) \quad \text{for disk 1 and}$$

$$|X_2| = |A \sin(\Omega t/2)| \exp(-\beta t) \quad \text{for disk 2, where } A \text{ is the initial}$$

displacement of the vortex core in disk 1. The best fit values of  $[\Omega, \beta]$  are

$2\pi \times [60 \pm 1, 5 \pm 0.1]$  MHz for Py and  $[46 \pm 1, 0.8 \pm 0.1]$  for NiMnSb.

Variables	Exchange time $\tau_{\text{ex}}$	Attenuation parameter $\beta$
Polarization ( $p_1, p_2$ )	$p_1 p_2 = -1 < p_1 p_2 = 1$	Independent
Interdistance ( $d_{\text{int}}$ )	$\tau_{\text{ex}} \sim (d_{\text{int}}/2R)^{3.9 \pm 0.07}$	Independent
Damping ( $\alpha$ )	Independent	$\beta = \frac{1}{2}\alpha [2 + \ln(R/R_c)] \omega_0$

**Table. 6.1** Dependence of exchange time and attenuation on variables such as polarization of each vortex, interdistance between elements, and damping constant of material.

### 6.10 Propagation of gyration in longer chain

We additionally examined the propagation of stimulated vortex gyrations in 1D arrays consisting of two more disks (i.e. ten disks) made of Py and NiMnSb, during free relaxation. In the simulations, we used the same means of first-disk excitation as in the previous simulation, but employed much smaller disks [ $2R = 201$ ,  $L = 6$  nm and  $d_{\text{int}}/(2R) \sim 1.04$ ] to reduce the computation time. Figure 6.14 shows the model geometry as well as the displacements of the vortex-core position vectors of the individual disks (up to the 5th disk) in the chains as a function of time. For such longer chains, the attenuation of energy transfer cannot be estimated simply by the parameter  $\beta/\Omega$ , as explained above. Further study is necessary. Here, we sought to interpret the attenuation of energy transfer through chains qualitatively. As can be seen, from the first to the second disk, the ratio of the maximum amplitude  $|X_i|$  of the oscillation of disk ( $i$ ) to  $|X_{i-1}|$  of disk ( $i-1$ ) was relatively low, that is,  $|X_2|/|X_1| \sim 0.61$  (0.69) for Py (NiMnSb). However, from the second disk to the third, and from the third to the fourth, and so on, the values of  $|X_i|/|X_{i-1}|$  for Py (NiMnSb) increased to the 0.87~0.88 (0.93~0.97) range. The relatively small value of  $|X_2|/|X_1|$  compared with those of  $|X_i|/|X_{i-1}|$  resulted from the fact that the stored energy in the first disk, upon the commencement of free relaxation, dissipates through not only the second disk but also the third one. Comparing the Py and NiMnSb chains, the smaller damping constant resulted in a more significantly reduced



attenuation effect. All of the above results confirm that information signal transfer by stimulated vortex gyration exhibits low attenuation; further, they show that low energy dissipation can be achieved with low-damping-constant materials such as NiMnSb. The results suggest also that logic functions based on stimulated gyrations in coupled disks can be conducted with signal transfer only through the nearest (first) and second-nearest neighboring disks.

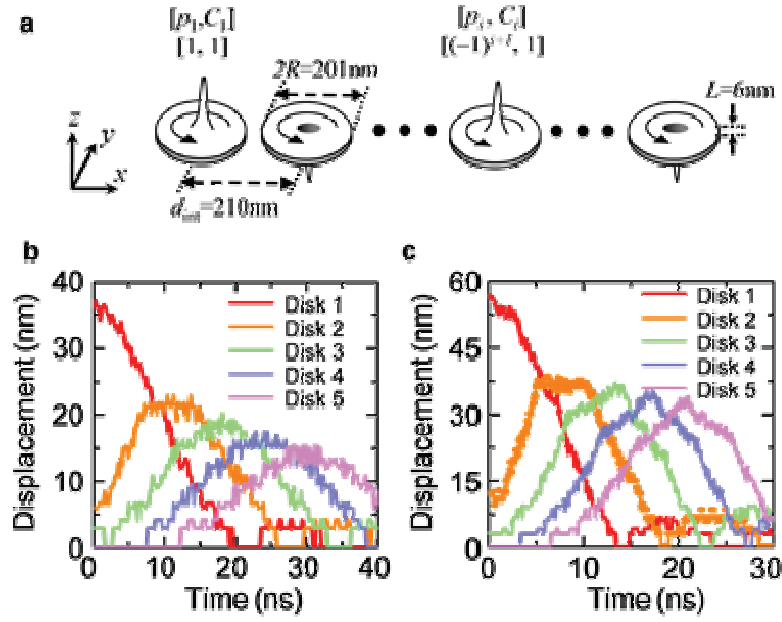


**FIG. 6.14** Propagation of stimulated vortex gyrations in 1D disk arrays during free relaxation. (a) Model geometry of chain of ten disks, each disk of  $2R = 201$ ,  $L = 6 \text{ nm}$  and  $d_{\text{int}}/(2R) \sim 1.04$ . The chiralities of all of the disks were set to  $C = +1$ , but for the  $i$ -th disks, the polarities were set to  $p = +1$  for  $i = \text{odd}$  and  $p = -1$  for  $i = \text{even}$ . The modulation envelopes of the vortex-core displacements versus time are shown in (b) for Py and in (c) for NiMnSb.

To conclude, we experimentally observed, by time-resolved MTXM, energy and information-signal transfer via stimulated vortex gyration through dipolar interaction between separate magnetic disks. This robust new mechanism for energy transfer provides the advantages of a fast and tunable energy transfer rate that is a function of disk interdistance and interaction strength. Control of energy loss during gyration-mediated signal transfer is possible with material engineering; in fact, almost lossless energy transfer can be achieved by employment of a material having negligible damping. Vortex gyration also can be achieved with low-power consumption through the resonant vortex excitation. This finding opens a new avenue to the development of novel fast, small, versatile and energy efficient information processing devices based on magnetic nanodots.

## Chapter 7

### Logic Operation using Vortex State Structures

In current semiconductor technology, the electron charge is the basic operational unit in information-processing devices. The major limitation of that technology in cases of nanoscale electron channels is the significant electron leakage and inevitable energy loss [94, 95]. This demands additional research into new practical alternatives. One such alternative is to use switchable magnetization states. For examples, some earlier works [96-98] report on magnetic quantum-dot cellular automata that consist of single-domain magnets. Possible logic operations using closed-flux states in ring-type magnets have also been reported [99]. Barman *et al.* proposed a new type of signal transfer mechanism based on vortex-state disk chains and coupled gyrations, as studied by micromagnetic simulations [79]. These alternatives promise to significantly reduce the energy dissipation and avoid the electron leakage problem. Having extended the concept, we propose logic operations based on magnetic-vortex-state networks and report an experimental demonstration of a simple, archetypal XOR logic operation achieved *via* a vortex-gyration-mediated information-signal transfer mechanism [27, 77, 79-81, 100]. The advantages are signal transfer endurance, low energy dissipation, and low-power signal inputs *via* resonant vortex excitation. This work paves the way for a new type of logic operation

based on magnetic-vortex-state networks.

## 7.1 Design of archetypal XOR logic by simulations

As mentioned in previous chapter, it is known that magnetic-vortex gyration in a confined potential is the low-frequency eigenmode of the translational orbital motion of a single vortex core, around its equilibrium position, at a characteristic eigenfrequency  $\omega_D$  [27]. If the frequency  $\omega_H$  of any driving force is tuned to  $\omega_D$ , the vortex gyration can readily be excited resonantly, even with extremely low power consumption, as already demonstrated in earlier works [20, 24, 31, 101]. The gyration's rotational sense is determined by the vortex-core orientation, that is, counter-clockwise for the up core (polarization,  $p = +1$ ), and clockwise for the down core ( $p = -1$ ). When isolated vortex-state thin-film disks are sufficiently close to each other, the vortex gyrations of the neighboring individual disks are coupled *via* their respective dynamically rotating stray fields [52, 55, 70], which coupling provides the opportunity for mutual energy transfer and frequency splitting, as found in a variety of coupled oscillators existing in nature [83].

Based on our recently demonstrated robust mechanism of vortex-gyration-mediated energy and consequent information-signal transfer between neighboring vortex-state disks, the next milestone towards the realization of vortex-state-network-based logic gates, for example, using three vortex-state Py disks, is here presented. If two electrodes are positioned on both Py end disks (hereafter, disk 1 and disk 3), the “1” logic function input state can be initiated by applying currents to either or both electrodes

and exciting, thereby, vortex gyrations. The gyration of the center disk (hereafter, disk 2), which is stimulated by the gyrations of either disk 1 or disk 3, can be represented as the “1” logical output, and can be monitored. To study our concept, we first conducted micromagnetic simulations of magnetic-vortex-state networks comprising three different Py disks. The Landau-Lifshitz-Gilbert (LLG) equation of motion of the local magnetizations was numerically solved on the model system shown in Fig. 1, using the OOMMF code. The material parameters of the Py disks of the indicated dimensions were set as follows: exchange stiffness  $A_{\text{ex}} = 13$  pJ/m; saturation magnetization  $M_s = 8.6 \times 10^5$  A/m; magnetic anisotropy constant = 0; gyromagnetic ratio  $\gamma = 2.21 \times 10^5$  m/As; damping constant  $\alpha = 0.01$ . The unit cell size was  $3 \times 3 \times 6$  nm<sup>3</sup>. To resonantly excite vortex gyrations, a continuous sinusoidal oscillating magnetic field of 1 mT amplitude and 210 MHz frequency was applied, 210 MHz being the eigenfrequency of the isolated Py disks.

Figure 7.2 illustrates the trajectories of vortex-core gyrations in the individual disks for three different logical inputs: The application of currents to both disk 1 and 3, representing the “11” logical input, yields the excitation of large-amplitude vortex gyrations in disks 1 and 3. For the specific case of  $p_1 p_3 = +1$  (where the numbers in subscripts indicate the disks), the “11” logical input yields the “0” logical output, since the vortex excitation of disk 2 is suppressed. For the cases of applications of currents to either disk 1 or

disk 3, which is referred to as the “10” or “01” logical state, by contrast, these inputs give rise to the “1” logical output, as represented by the sufficiently large gyration amplitude in disk 2. The gyration in disk 2 is stimulated by the gyration of disk 1 or 3 *via* the dipolar interaction between the nearest neighboring disks as described in previous Section. These logical functions represent an XOR gate.



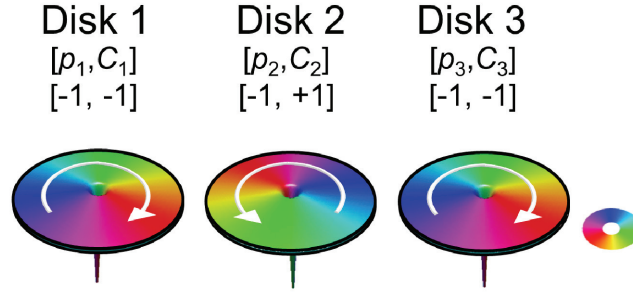


**FIG 7.1** Coupled magnetic-vortex-state network. Model geometry of three Py disks of indicated initial ground states. The local in-plane magnetizations inside each disk are represented by the colors shown in the color wheel (inset) and the curling orientations are indicated by the white arrows (chirality,  $C = +1$  and  $-1$  for CCW and CW rotational sense, respectively). The spike at the center of each disk indicates the out-of-plane component of the core magnetization (polarization,  $p = +1$  and  $-1$  for the up core and down core, respectively). For micromagnetic numerical simulations, equal diameter  $2R = 300$  nm, thickness  $L = 6.0$  nm, and center-to-center distance  $d_{\text{int}} = 330$  nm were used.

In order to elucidate such contrasting behaviors between the “11” and “10” logic inputs, that is, suppressed excitation *versus* large-amplitude-gyration excitation in disk 2, we considered the vector sum of the dynamically rotating stray fields produced by the nonzero net in-plane magnetizations of both end disks (See Fig. 7.2, right panel). When the cores are shifted from their initial center positions and gyrate at their own  $\omega_D$ , the stray fields also rotate at the same frequency as  $\omega_D$  but with a certain ellipticity, which is defined as the ratio of the field strength along the x-axis to that along the y-axis. Therefore, these fields can be referred to as “elliptically rotating dynamic fields.” Here, for the case of parallel polarizations in the end disks ( $p_1 p_3 = +1$ ), the net resulting stray field inside disk 2 is almost zero for the “11” input, as shown in Fig. 7.2 (left, top). Contrastingly, for the case of “10” or “01,” the vortex gyration with the clockwise (CW) rotational sense in either disk 1 or disk 3 results in a counter-clockwise (CCW) elliptically rotating field. As reported earlier, the application of CW rotating fields of  $\omega_H = \omega_D$  leads to large-amplitude resonant excitations for the down core but no-excitations for the up core, whereas the application of CCW rotating fields produces the opposite effect. The CCW elliptically rotating field applied to disk 2, which field results from the vector sum of the CCW and CW circular-rotational fields with a CCW-to-CW amplitude ratio of 2.5, was obtained from a fit to the simulation data. Although the CCW component is 2.5 times larger than that

of the CW, this CW component can still excite the gyration of the down core, as evidenced by the trajectory of the core in disk 2 (see Fig. 7.2, left, bottom). If the core were upward, the gyration amplitude would have been larger than was measured in the present case.

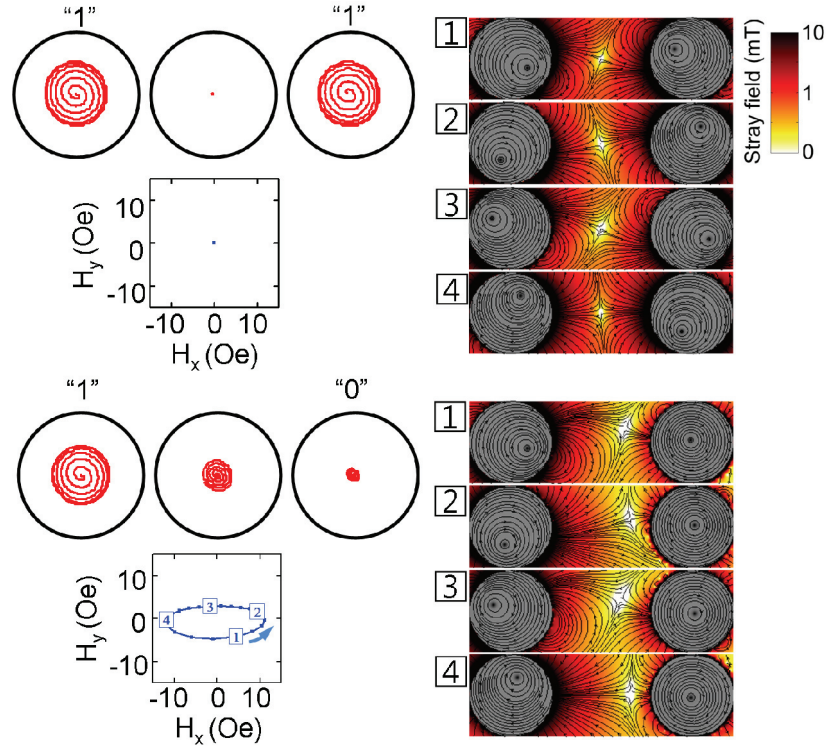


**FIG. 7.2** Simulation results for coupled vortex gyrations. Trajectories of vortex-core gyrations in three disks of initial vortex states indicated in Fig. 1 for two logical inputs “11” and “10” (left top and bottom, respectively). As described in the text, the logical input “1” indicates the presence of resonant vortex gyration excited by the application of input currents. The spatial distributions of the effective local rotating fields in disk 2, which are the results for the sum of the stray fields generated by the shifted core motions of disk 1 and/or disk 3 (right panel). The local fields averaged inside the disk 2 over one cycle gyration are given just below the corresponding disk 2 (left panel), along with the rotational sense of the field indicated by the corresponding arrow.

## 7.2 Experimental verification using soft X-ray microscopy

Next, the XOR gate concept was experimentally confirmed through vortex gyration propagation in an array of vortex-state disks. To experimentally demonstrate the proposed logic gate of a coupled vortex-state network, we used three Py disk samples, each of radius  $R = 1.2 \mu\text{m}$ , thickness  $L = 50 \text{ nm}$ , and center-to-center distance  $d_{\text{int}} = 2.46 \mu\text{m}$ , which were deposited onto a 200 nm-thick silicon nitride membrane by DC magnetron sputtering. To generate magnetic fields, two electrodes of Ti 10 nm / Cu 100 nm / Au 5 nm were deposited directly on top of both of the end disks by DC sputtering without vacuum breaking. Patterning of the samples was carried out by electron beam lithography and lift-off processing. To avoid adjacent-disk excitations due to the applied local field, the width of the electrodes, as designed, was  $1.6 \mu\text{m}$ . The gap between two signal lines is narrow, thus crosstalk between the lines should be considered. In here, the problem is more serious because the coplanar wave guide or backside ground plate is impossible in this type of sample. In order to prevent crosstalk between lines, the parallel part which has shortest interdistance between lines is minimized.

Vortex gyrations in the individual Py disks were directly imaged by full-field MTXM at BL 6.1.2 of ALS in Berkeley, CA, utilizing a stroboscopic pump-and-probe technique providing 70 ps time- and 25 nm spatial resolutions. Details on this time-resolving technique can be found in Chapter

4.4. In-plane magnetization contrast was obtained by monitoring the spatial distribution of the local magnetizations through XMCD at the Fe  $L_3$  absorption edge, where the sample surface was positioned at a  $60^\circ$  orientation to the propagation direction of the incident x-rays. A 10-period sine-wave field of 4.5 Oe ( $\sim 7.14 \times 10^5$  A/cm<sup>2</sup>) amplitude and 160 MHz frequency was used to excite vortex gyrations in disk 1 and/or disk 3, where 160 MHz was the eigenfrequency of the sample disks of the given simulation-obtained dimensions.

Specifically, for the “1” logical input, external driving forces in the form of magnetic fields (or spin-polarized currents) were applied to disk 1 and/or disk 3, and as the “1” logical output, vortex gyrations excited in disk 2 was utilized. We directly measured, as logic output state, the dynamic excitations of the vortex gyrations in disk 2, while simultaneously monitoring those in disks 1 and 3 using the large field of view offered by the time-resolved full-field soft x-ray microscopy and employing XMCD as magnetic contrast. The respective initial ground states of the disks in the real sample are shown in the inset of Fig. 7.3. The chirality of each disk was determined directly by the in-plane magnetization contrast, whereas the polarization was derived from the rotational sense of the vortex gyrations in the three disks, as indicated. Note that we used larger dimensions of samples than those employed in the simulations because of the experimental limitations of detecting gyration signals using soft x-ray microscopy and

since the main dynamic behaviors of coupled gyrations and logic functions between smaller- and larger-dimension samples are not much different, except for the eigenfrequency.

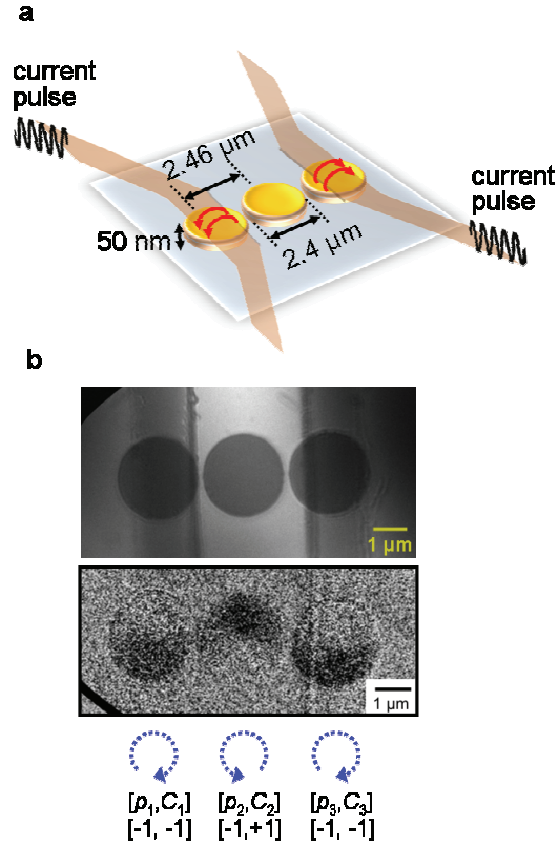


**FIG. 7.3** (a) Schematic layout of sample (chain of three vortex-state Py disks) with electrodes on both end disks for application of input signals. Equal diameter  $2R = 2.4 \mu\text{m}$ , thickness  $L = 50 \text{ nm}$ , and center-to-center distance  $d_{\text{int}} = 2.46 \mu\text{m}$  are used for the experimental sample. (b) Transmission soft X-ray microscopy image of the sample used in the experiment, displaying the chemical contrasts of three different Py disks and two electrodes (top). The initial ground vortex states measured by the microscope through XMCD contrast same as those shown in Fig. 7.1 (bottom). Sinusoidal oscillating magnetic fields of 4.5 Oe amplitude and 160 MHz frequency are applied to disk 1 and/or disk 3.



### 7.3 Differential XMCD images of individual disks' vortex gyrations

Since the contrast of the magnetization dynamics was weak due to the too-small displacements of the individual cores in the snapshot images, a differential imaging technique was used to confirm the gyration. The differential images were obtained by subtracting two images taken with  $\pi$  phase difference of the exciting magnetic field. Differential imaging shows only the dynamic magnetization changes which are synchronized with the excitation, removing all static magnetic and nonmagnetic contrast contributions. Figure 7.4a illustrates the serial magnetization images for every  $\pi/2$  phases of vortex gyration and their differential images with  $\pi$  phase difference in a circular disk. The images are obtained from numerical calculation on basis of side surface charge free model [102]. The dynamic contrast results in characteristic patterns of black or white ellipses or black/white crosses. However, as shown in Fig. 7.4b, there is no pattern in differential images when the vortex core remains stationary.

As shown in Fig. 7.5 and 7.6, a series of differential images of  $\pi$  phase difference which show only the dynamic changes of the individual disks' magnetizations during their vortex-core motions. Given the absence of any core gyration, the static magnetization contrast was removed so that there would be no contrast around the core region [103]. Accordingly, from those differential images, we identified the logical input and output states. For the “10” (top) and “01” (bottom) input states, the logical output is

indicated to be the “1” state. The relatively dark and white contrasts in disk 2 evidence the gyration. For the “11” input state, the “0” output state appears, as represented by the no-gyration (no any contrast) of disk 2 in the differential image (see Figs. 7.5 and 7.6). These functions represent the XOR logic. This experimental demonstration provides a promising foundation for the practical realization of logic devices based on vortex-state networks and readily controllable vortex-gyration dynamics.

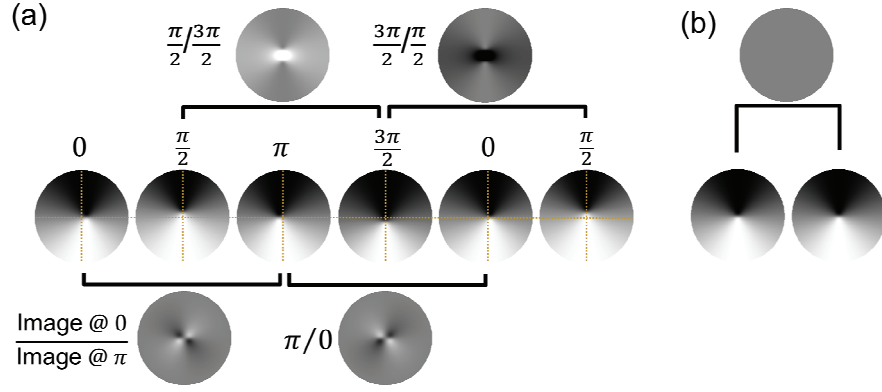


**FIG. 7.4** (a) Snapshot images of vortex gyration taken at every  $\pi/2$  phase variation (middle) and their differential images (top and bottom) obtained by subtracting two different snapshot images of  $\pi$  phase difference, as indicated. These differential images of the  $\pi$  phase difference show only the dynamic changes of magnetizations in the disk during vortex-core motions. Thus, the relatively dark and white contrasts around the core regions represent the occurrence of the vortex gyration. The dynamic contrasts present black or white “dots” (top) or black and white “crosses” (bottom). (b) Same static vortex state (middle) with core positioned at center. Given the absence of any core gyration, the static magnetization contrast was removed so that there would be no contrast around the core region, as shown in the differential image (top).

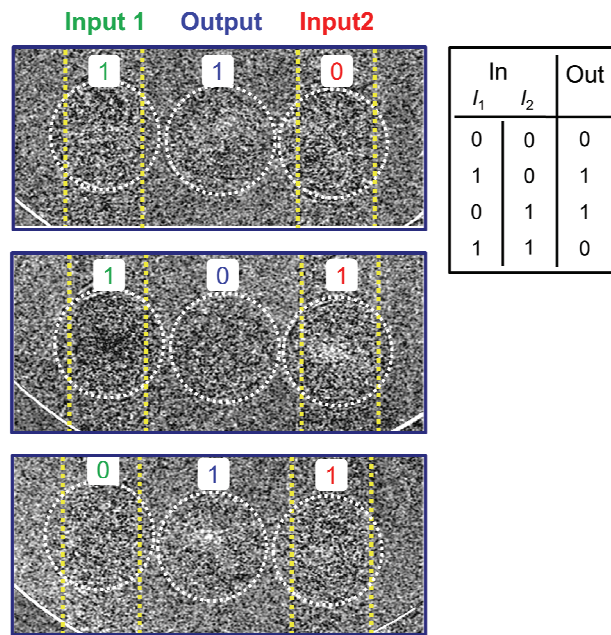


**FIG. 7.5** Differential XMCD images of individual disks' vortex gyrations. Three different logical inputs of “10,” “11,” and “01” are applied. The inset shows the truth table representing the logical input and resultant output operations for the XOR gate.

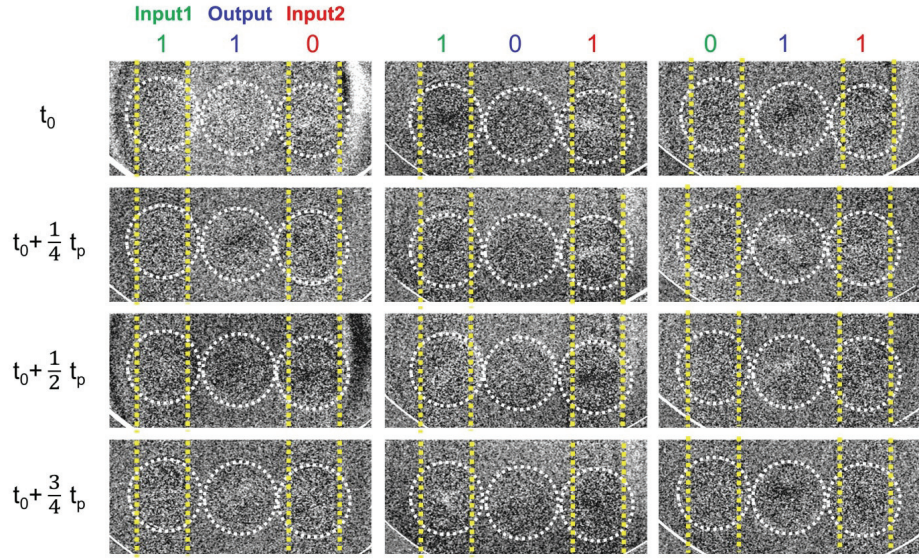


**FIG. 7.6** Differential XMCD images obtained by subtracting two snapshot images taken with  $180^\circ$  phase difference for three different logical inputs of “10,” “11,” and “01”. The individual rows indicate those differential images obtained at every  $1/4$  period of one vortex-gyration cycle. When a shifted core gyrates around its center position, the relatively white and dark regions would be switched for different times.

#### 7.4 Programmable logic operations

It is interesting to note that for the antiparallel polarization  $p_1p_3 = -1$ , unlike the “11” input-signal result for the  $p_1p_3 = +1$  case, vortex gyrations were resonantly excited in disk 2, leading to the “1” logical output (see Fig. 7.7), as found from additional simulations. For the logical input of either “10” or “01,” the vortex gyration remained excited in disk 2, which situation is referred to as the “1” logical state. Therefore, for the  $p_1p_3 = -1$  configuration, the employed logic function is an OR gate, as shown in Table 7.1. The polarization of either disk 1 or disk 3 can be readily reversed by a low-power-consumption oscillating field or pulses, as found earlier [20, 24, 34, 89, 101]. Thus, by manipulating the relative polarization configurations of both end disks with the same electrodes as those for application of logic inputs, the XOR and OR gates can be programmed; the XOR gate for the equal polarization  $p_1p_3 = +1$ , and the OR gate for the antiparallel polarization  $p_1p_3 = -1$ .

Based on simulations considering all relative polarization and chirality configurations, we summarize, in Table 1, the logic outputs in disk 2 for the four input cases “10,” “01,” “11,” and “00”. In all of these cases, only two logic gates, XOR and OR, were initiated for  $p_1p_3 = +1$  and  $-1$ , respectively. We note that neither the relative chirality configurations between disks 1 and 3 nor the polarization or chirality of disk 2 affected the overall logic functions. In order to identify either the logical output “0” or

“1,” in the present work, we monitored, by soft X-ray microscopy, the occurrence of vortex gyrations in disk 2.

$p_1$	1	1	-1	-1	-1	1	1	-1
$p_2$	1	-1	1	-1	1	1	-1	-1
$p_3$	1	1	-1	-1	1	-1	-1	1
Input		Output (Disk 2)						
Disk1	Disk3	$p_1 p_3 = 1$			$p_1 p_3 = -1$			
0	0	0	<b>XOR</b>		0	<b>OR</b>		
1	0	1			1			
0	1	1			1			
1	1	0			1			

**TABLE 7.1.** Truth table for possible logical inputs and resultant outputs for all relative polarization configurations in a chain of three vortex-state disks.

The resultant logic operation is an XOR gate for  $p_1 p_3 = +1$  (parallel polarization) or an OR gate for  $p_1 p_3 = -1$  (antiparallel polarization).



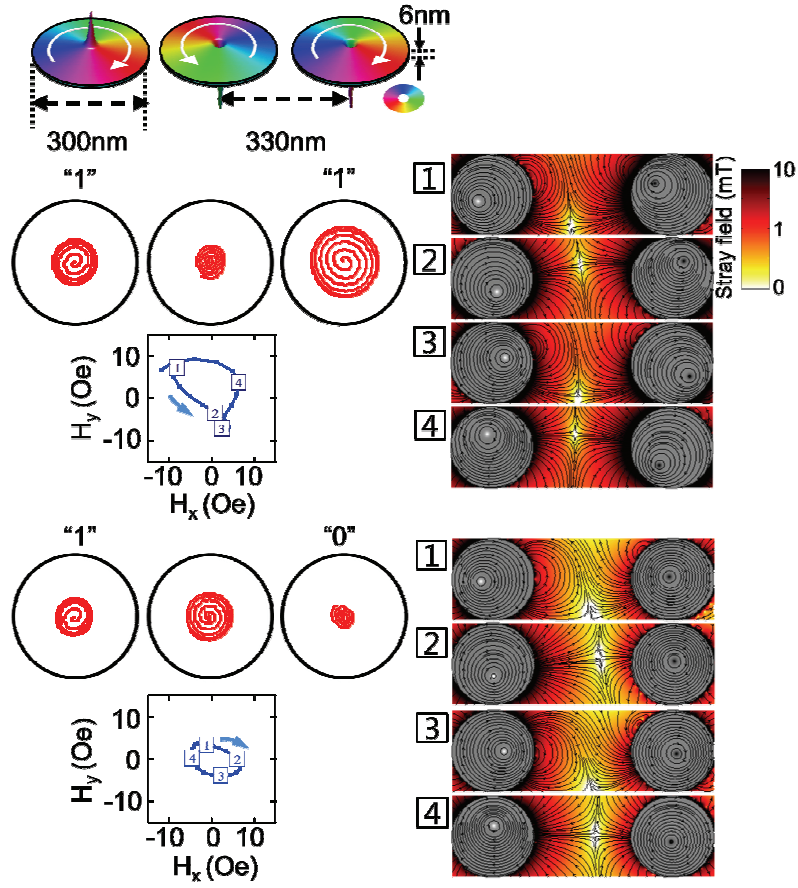


**FIG. 7.7** Same model geometry and dimensions as those in Fig. 7.1, but with different ground state, whereby polarization of disk 1 is upward,  $p_1 = 1$ , which state results in antiparallel polarization ( $p_1 p_3 = -1$ ) between disks 1 and 3. From the simulation results for the case of  $p_1 p_3 = -1$ , we plotted the trajectories of vortex-core gyrations in three disks for the two logical inputs “11” and “10” (left top and bottom, respectively).

## 7.5 Limitation

We note that the phase control of vortex-gyration excitations as input signals is very essential to the realization of logic devices using coupled vortex gyration propagation. We further conducted numerical calculations using Thiele's equation of motion of magnetizations [85]. From the additional simulation results (see Fig. 7.8), the gyration amplitude in the middle disk (disk 2) varies considerably with the phase difference  $\Delta$  of the frequencies between two magnetic fields applied to disks 1 and 3. The phase differences of less than 30 degrees nonetheless results in the gyration amplitude of disk 2, which is as small as 25 % of those of disks 1 and 3. The fact of the dependence of the gyration amplitude of disk 2 on  $\Delta$  is rather promising as regards control of the signal gain of vortex gyration and different logic functions by manipulation of the phase difference of the two input signals.

As for the readout of logical output signals in real devices, vortex gyrations excited in the middle disk can be detected by electrical measurements based on the fact that shifted cores result in asymmetry of in-plane curling magnetizations with respect to the ground vortex state. Therefore, tunneling magnetoresistance in spin-valve structures including vortex-state disks would be markedly variable depending on the amplitude of gyrations excited in the middle disk. For more details of possible detecting mechanisms experimentally demonstrated, see Refs [104-106].

Since this work is the first to experimentally demonstrate logic operations using the coupled gyrations of vortex-state disks, several technical issues for the implementations into real devices should be solved in future works; the readout mechanism of vortex excitations and signal-to-noise ratio through electrical measurements of output signals, amplification of the signal for fan-out; the threshold value for detection of reliable logical output signals, the asymmetries of the frequency, phase, amplitude of two different input signals, and the delay time and density of integrated logic gates will be clarified.

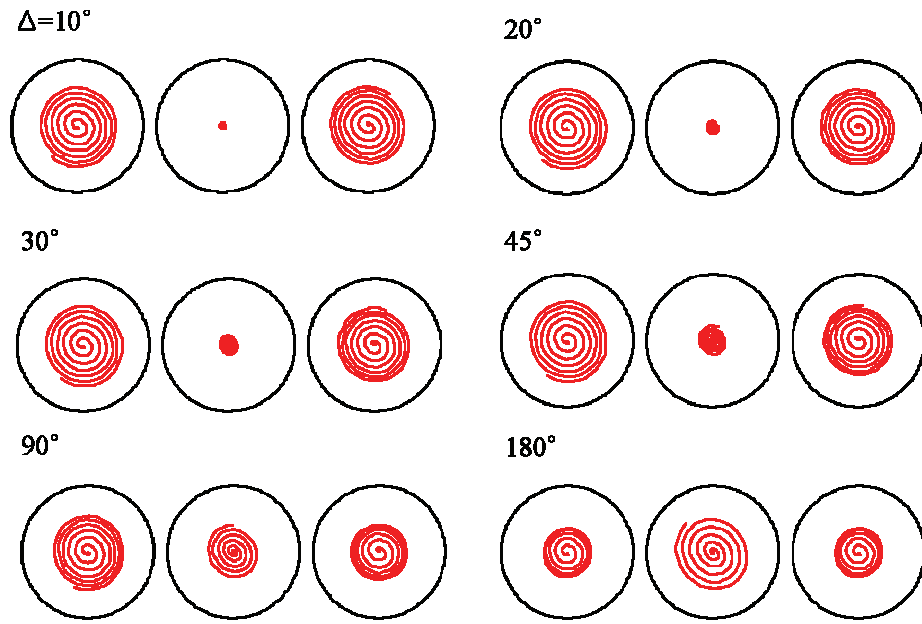


**FIG. 7.8** Trajectories of vortex-core gyrations for logical input “11” with indicated phase differences  $\Delta$ . The trajectories are obtained from numerical calculations using Thiele’s equation of motion of magnetizations.

Our work demonstrates low energy-loss, low-power signal-input logic gates that operate at room temperature on the principle that vortex gyrations are resonantly excited and strongly networked *via* coupling between neighboring vortex-state disks. Notably, the excitation of vortex gyrations and signal transfer between neighboring disks via the robust vortex-gyration-mediated mechanism are as fast as a few ns to a few tens of ns, depending on the disk dimensions, the separation distance, and the constituent-material parameters. Thus, such logic functions can be operated at up to 1 GHz levels by appropriate engineering of materials and disk dimensions. Moreover, by combining different vortex-state networks, a NOR gate can be formed, thereby establishing what is known as universal logic. The advantages are unlimited signal transfer endurance, low energy dissipation, and low-power signal inputs via resonant vortex excitation. All in all, the present work provides a solid foundation for implementation of the static and dynamic properties of coupled magnetic-vortex-state networks into spin-based information processing devices.

## Chapter 8

### Summary

In this thesis, we attempted to investigate dynamic interaction mediated by the vortex core's gyrotropic motion between magnetic vortex-state elements. For the study of such sub-micrometer and nanosecond-scale dynamics, we employed micromagnetic simulations, analytical calculations on the basis of Thiele's approach, and stroboscopic observation using X-ray microscopy.

In the first part, we experimentally observed oscillation of dipolar coupled vortices. The vortices had opposite polarizations and the same chirality; accordingly, they oscillated out-of-phase along the  $x$  axis and in-phase along the  $y$  axis. In this experiment, it was found that the vortex gyration of one disk affects that of the other through dipolar interaction.

In the second part, energy and information-signal transfer via stimulated vortex gyration through dipolar interaction between separate magnetic disks was investigated. This robust energy-transfer mechanism provides the advantages of a fast and tunable energy transfer rate that is a function of disk interdistance and interaction strength. Control of energy loss during gyration-mediated signal transfer is possible with material engineering. Vortex gyration also can be achieved with low-power consumption through resonant excitation.

Finally, on the principle established earlier in this thesis, low-energy-loss, low-power signal-input logic gates were demonstrated. Notably, the excitation of vortex gyrations and signal transfer between neighboring disks via the robust vortex-gyration-mediated mechanism are as fast as a few ns to a few tens of ns, depending on the disk dimensions, the separation distance, and the constituent-material parameters.

## Bibliography

- [1] S.D. Bader and S.S.P. Parkin, *Spintronics*, Annual Review of Condensed Matter Physics **1**, 71 (2010).
- [2] A. Fert, *The present and the future of spintronics*, Thin Solid Films **517**, 2 (2008).
- [3] H. Ohno, *Spintronics - A Renaissance in magnetism*, Journal of the Physical Society of Japan **77**, IV (2008).
- [4] R.P. Cowburn, *Spintronics - Change of direction*, Nat Mater **6**, 255 (2007).
- [5] C. Chappert, A. Fert, and F.N. Van Dau, *The emergence of spin electronics in data storage*, Nat Mater **6**, 813 (2007).
- [6] M. Hayashi, L. Thomas, R. Moriya, C. Rettner, and S.S.P. Parkin, *Current-controlled magnetic domain-wall nanowire shift register*, Science **320**, 209 (2008).
- [7] S.S.P. Parkin, M. Hayashi, and L. Thomas, *Magnetic domain-wall racetrack memory*, Science **320**, 190 (2008).



- [8] S. Kaka, M.R. Pufall, W.H. Rippard, T.J. Silva, S.E. Russek, and J.A. Katine, *Mutual phase-locking of microwave spin torque nano-oscillators*, Nature **437**, 389 (2005).
- [9] F.B. Mancoff, N.D. Rizzo, B.N. Engel, and S. Tehrani, *Phase-locking in double-point-contact spin-transfer devices*, Nature **437**, 393 (2005).
- [10] C.-Y. You and S.D. Bader, *Voltage controlled spintronic devices for logic applications*, Journal of Applied Physics **87**, 5215 (2000).
- [11] J. William C. Black and B. Das, *Programmable logic using giant-magnetoresistance and spin-dependent tunneling devices (invited)*, Journal of Applied Physics **87**, 6674 (2000).
- [12] R. Richter, L. Bar, J. Wecker, and G. Reiss, *Nonvolatile field programmable spin-logic for reconfigurable computing*, Applied Physics Letters **80**, 1291 (2002).
- [13] A. Ney, C. Pampuch, R. Koch, and K.H. Ploog, *Programmable computing with a single magnetoresistive element*, Nature **425**, 485 (2003).
- [14] S. Matsunaga, J. Hayakawa, S. Ikeda, K. Miura, H. Hasegawa, T. Endoh, H. Ohno, and T. Hanyu, *Fabrication of a nonvolatile full adder based on logic-in-memory architecture using magnetic tunnel junctions*, Applied

Physics Express **1**, 091301 (2008).

[15] S.A. Wolf, J.W. Lu, M.R. Stan, E. Chen, and D.M. Treger, *The Promise of Nanomagnetism and Spintronics for Future Logic and Universal Memory*, Proceedings of the Ieee **98**, 2155 (2010).

[16] T. Shinjo, T. Okuno, R. Hassdorf, K. Shigeto, and T. Ono, *Magnetic vortex core observation in circular dots of permalloy*, Science **289**, 930 (2000).

[17] A. Wachowiak, J. Wiebe, M. Bode, O. Pietzsch, M. Morgenstern, and R. Wiesendanger, *Direct observation of internal spin structure of magnetic vortex cores*, Science **298**, 577 (2002).

[18] J.P. Park, P. Eames, D.M. Engebretson, J. Berezovsky, and P.A. Crowell, *Imaging of spin dynamics in closure domain and vortex structures*, Physical Review B **67**, 020403 (2003).

[19] S.B. Choe, Y. Acremann, A. Scholl, A. Bauer, A. Doran, J. Stohr, and H.A. Padmore, *Vortex core-driven magnetization dynamics*, Science **304**, 420 (2004).

[20] B. Van Waeyenberge, A. Puzic, H. Stoll, K.W. Chou, T. Tyliczszak, R. Hertel, M. Fahnle, H. Bruckl, K. Rott, G. Reiss, I. Neudecker, D. Weiss, C.H.

Back, and G. Schutz, *Magnetic vortex core reversal by excitation with short bursts of an alternating field*, Nature **444**, 461 (2006).

[21] M. Bolte, G. Meier, B. Kruger, A. Drews, R. Eiselt, L. Bocklage, S. Bohlens, T. Tylliszczak, A. Vansteenkiste, B. Van Waeyenberge, K.W. Chou, A. Puzic, and H. Stoll, *Time-resolved x-ray microscopy of spin-torque-induced magnetic vortex gyration*, Physical Review Letters **100**, 176601 (2008).

[22] N. Kikuchi, S. Okamoto, O. Kitakami, Y. Shimada, S.G. Kim, Y. Otani, and K. Fukamichi, *Vertical bistable switching of spin vortex in a circular magnetic dot*, Journal of Applied Physics **90**, 6548 (2001).

[23] K. Yamada, S. Kasai, Y. Nakatani, K. Kobayashi, H. Kohno, A. Thiaville, and T. Ono, *Electrical switching of the vortex core in a magnetic disk*, Nat Mater **6**, 269 (2007).

[24] S.K. Kim, K.S. Lee, Y.S. Yu, and Y.S. Choi, *Reliable low-power control of ultrafast vortex-core switching with the selectivity in an array of vortex states by in-plane circular-rotational magnetic fields and spin-polarized currents*, Applied Physics Letters **92**, 022509 (2008).

[25] S. Bohlens, B. Kruger, A. Drews, M. Bolte, G. Meier, and D. Pfannkuche, *Current controlled random-access memory based on magnetic*

*vortex handedness*, Applied Physics Letters **93**, 142508 (2008).

[26] B.C. Choi, J. Rudge, E. Girgis, J. Kolthammer, Y.K. Hong, and A. Lyle, *Spin-current pulse induced switching of vortex chirality in permalloy/Cu/Co nanopillars*, Applied Physics Letters **91**, 022501 (2007).

[27] K.Y. Guslienko, B.A. Ivanov, V. Novosad, Y. Otani, H. Shima, and K. Fukamichi, *Eigenfrequencies of vortex state excitations in magnetic submicron-size disks*, Journal of Applied Physics **91**, 8037 (2002).

[28] Y.W. Liu, Z.W. Hou, S. Gliga, and R. Hertel, *Influence of the dynamic dipolar interaction on the current-induced core switch in vortex pairs*, Physical Review B **79**, 104435 (2009).

[29] K.Y. Guslienko, *Magnetostatic interdot coupling in two-dimensional magnetic dot arrays*, Applied Physics Letters **75**, 394 (1999).

[30] T. Pokhil, D.A. Song, and J. Nowak, *Spin vortex states and hysteretic properties of submicron size NiFe elements*, Journal of Applied Physics **87**, 6319 (2000).

[31] S. Kasai, Y. Nakatani, K. Kobayashi, H. Kohno, and T. Ono, *Current-driven resonant excitation of magnetic vortices*, Physical Review Letters **97**, 107204 (2006).

- [32] K.S. Lee and S.K. Kim, *Gyrotropic linear and nonlinear motions of a magnetic vortex in soft magnetic nanodots*, Applied Physics Letters **91**, 132511 (2007).
- [33] V.S. Pribiag, I.N. Krivorotov, G.D. Fuchs, P.M. Braganca, O. Ozatay, J.C. Sankey, D.C. Ralph, and R.A. Buhrman, *Magnetic vortex oscillator driven by d.c. spin-polarized current*, Nature Physics **3**, 498 (2007).
- [34] K.S. Lee and S.K. Kim, *Two circular-rotational eigenmodes and their giant resonance asymmetry in vortex gyrotropic motions in soft magnetic nanodots*, Physical Review B **78**, 014405 (2008).
- [35] Y.-S. Choi, S.-K. Kim, K.-S. Lee, and Y.-S. Yu, *Understanding eigenfrequency shifts observed in vortex gyrotropic motions in a magnetic nanodot driven by spin-polarized out-of-plane dc current*, Applied Physics Letters **93**, 182508 (2008).
- [36] Q. Mistral, M. van Kampen, G. Hrkac, J.V. Kim, T. Devolder, P. Crozat, C. Chappert, L. Lagae, and T. Schrefl, *Current-driven vortex oscillations in metallic nanocontacts*, Physical Review Letters **100**, 257201 (2008).
- [37] Y.S. Choi, K.S. Lee, and S.K. Kim, *Quantitative understanding of magnetic vortex oscillations driven by spin-polarized out-of-plane dc current: Analytical and micromagnetic numerical study*, Physical Review B

79, 184424 (2009).

[38] A. Ruotolo, V. Cros, B. Georges, A. Dussaux, J. Grollier, C. Deranlot, R. Guillemet, K. Bouzehouane, S. Fusil, and A. Fert, *Phase-locking of magnetic vortices mediated by antivortices*, Nature Nanotechnology **4**, 528 (2009).

[39] R. Lehdorff, D.E. Burgler, S. Gliga, R. Hertel, P. Grunberg, C.M. Schneider, and Z. Celinski, *Magnetization dynamics in spin torque nano-oscillators: Vortex state versus uniform state*, Physical Review B **80**, 054412 (2009).

[40] G. Finocchio, V.S. Pribiag, L. Torres, R.A. Buhrman, and B. Azzerboni, *Spin-torque driven magnetic vortex self-oscillations in perpendicular magnetic fields*, Applied Physics Letters **96**, 102508 (2010).

[41] A. Dussaux, B. Georges, J. Grollier, V. Cros, A.V. Khvalkovskiy, A. Fukushima, M. Konoto, H. Kubota, K. Yakushiji, S. Yuasa, K.A. Zvezdin, K. Ando, and A. Fert, *Large microwave generation from current-driven magnetic vortex oscillators in magnetic tunnel junctions*, Nat Commun **1**, 8 (2010).

[42] J. Shibata, K. Shigeto, and Y. Otani, *Dynamics of magnetostatically coupled vortices in magnetic nanodisks*, Physical Review B **67**, 224404 (2003).

- [43] A. Slavin, *MICROWAVE SOURCES Spin-torque oscillators get in phase*, Nature Nanotechnology **4**, 479 (2009).
- [44] W.F. Brown, *Micromagnetics*, Interscience Publishers, New York,, 1963.
- [45] A. Aharoni, *Introduction to the theory of ferromagnetism*, 2nd ed., Oxford University Press, Oxford ; New York, 2000.
- [46] L.D. Landau and E.M. Lifshitz, *On the theory of the dispersion of magnetic permeability in ferromagnetic bodies*, Ukrainian Journal of Physics **53**, 14 (2008).
- [47] T.L. Gilbert, *A phenomenological theory of damping in ferromagnetic materials*, Ieee Transactions on Magnetics **40**, 3443 (2004).
- [48] A.A. Thiele, *Steady-State Motion of Magnetic Domains*, Physical Review Letters **30**, 230 (1973).
- [49] D.L. Huber, *Dynamics of Spin Vortices in Two-Dimensional Planar Magnets*, Physical Review B **26**, 3758 (1982).
- [50] K.Y. Guslienko, V. Novosad, Y. Otani, H. Shima, and K. Fukamichi, *Field evolution of magnetic vortex state in ferromagnetic disks*, Applied Physics Letters **78**, 3848 (2001).

- [51] B.E. Argyle, E. Terrenzio, and J.C. Slonczewski, *Magnetic Vortex Dynamics Using the Optical Cotton-Mouton Effect*, Physical Review Letters **53**, 190 (1984).
- [52] H. Shima, V. Novosad, Y. Otani, K. Fukamichi, N. Kikuchi, O. Kitakamai, and Y. Shimada, *Pinning of magnetic vortices in microfabricated permalloy dot arrays*, Journal of Applied Physics **92**, 1473 (2002).
- [53] Y. Otani, H. Shima, K. Guslienko, V. Novosad, and K. Fukamichi, *Magnetic properties of nano-structured ferromagnetic dot arrays*, Physica Status Solidi a-Applied Research **189**, 521 (2002).
- [54] V. Novosad, K.Y. Guslienko, H. Shima, Y. Otani, S.G. Kim, K. Fukamichi, N. Kikuchi, O. Kitakami, and Y. Shimada, *Effect of interdot magnetostatic interaction on magnetization reversal in circular dot arrays*, Physical Review B **65**, 060402 (2002).
- [55] V. Novosad, K.Y. Guslienko, Y. Otani, H. Shima, and K. Fukamichi, *Magnetostatic interdot coupling in arrays of circular ferromagnetic dots*, Journal of Magnetism and Magnetic Materials **239**, 234 (2002).
- [56] K.S. Buchanan, P.E. Roy, M. Grimsditch, F.Y. Fradin, K.Y. Guslienko, S.D. Bader, and V. Novosad, *Soliton-pair dynamics in patterned ferromagnetic ellipses*, Nature Physics **1**, 172 (2005).



- [57] K.S. Buchanan, P.E. Roy, F.Y. Fradin, K.Y. Guslienko, M. Grimsditch, S.D. Bader, and V. Novosad, *Vortex dynamics in patterned ferromagnetic ellipses*, Journal of Applied Physics **99**, 08C707 (2006).
- [58] K.Y. Guslienko, K.S. Buchanan, S.D. Bader, and V. Novosad, *Dynamics of coupled vortices in layered magnetic nanodots*, Applied Physics Letters **86**, 223112 (2005).
- [59] D. Chumakov, J. McCord, R. Schafer, L. Schultz, H. Vinzelberg, R. Kaltofen, and I. Monch, *Nanosecond time-scale switching of permalloy thin film elements studied by wide-field time-resolved Kerr microscopy*, Physical Review B **71**, 014410 (2005).
- [60] F. Bitter, *Experiments on the nature of ferromagnetism*, Physical Review **41**, 507 (1932).
- [61] P.J. Stephens, *Magnetic Circular-Dichroism*, Annual Review of Physical Chemistry **25**, 201 (1974).
- [62] J.L. Erskine and E.A. Stern, *Calculation of M23 Magneto-Optical Absorption-Spectrum of Ferromagnetic Nickel*, Physical Review B **12**, 5016 (1975).
- [63] W.L. Chao, B.D. Harteneck, J.A. Liddle, E.H. Anderson, and D.T.

Attwood, *Soft X-ray microscopy at a spatial resolution better than 15nm*, Nature **435**, 1210 (2005).

[64] P. Fischer, T. Eimuller, G. Schutz, P. Guttman, G. Schmahl, K. Pruegl, and G. Bayreuther, *Imaging of magnetic domains by transmission x-ray microscopy*, Journal of Physics D-Applied Physics **31**, 649 (1998).

[65] J. Stohr, H.A. Padmore, S. Anders, T. Stammler, and M.R. Scheinfein, *Principles of X-ray magnetic dichroism spectromicroscopy*, Surface Review and Letters **5**, 1297 (1998).

[66] P. Fischer, G. Schutz, G. Schmahl, P. Guttman, and D. Raasch, *Imaging of magnetic domains with the X-ray microscope at BESSY using X-ray magnetic circular dichroism*, Zeitschrift Fur Physik B-Condensed Matter **101**, 313 (1996).

[67] P. Fischer, D.H. Kim, B. Kang, W. Chao, and E.H. Anderson, *Magnetic microstructures and their dynamics studied by X-ray microscopy*, Micron **37**, 296 (2006).

[68] D.T. Attwood, *Soft x-rays and extreme ultraviolet radiation : principles and applications*, Cambridge University Press, Cambridge ; New York, 2000.

[69] B.L. Mesler, P. Fischer, W. Chao, E.H. Anderson, and D.H. Kim, *Soft x-*

*ray imaging of spin dynamics at high spatial and temporal resolution*,  
Journal of Vacuum Science & Technology B **25**, 2598 (2007).

[70] P. Fischer, *Studying nanoscale magnetism and its dynamics with soft X-ray microscopy*, Ieee Transactions on Magnetism **44**, 1900 (2008).

[71] J. Vogel, W. Kuch, M. Bonfim, J. Camarero, Y. Pennec, F. Offi, K. Fukumoto, J. Kirschner, A. Fontaine, and S. Pizzini, *Time-resolved magnetic domain imaging by x-ray photoemission electron microscopy*, Applied Physics Letters **82**, 2299 (2003).

[72] A. Vogel, A. Drews, T. Kamionka, M. Bolte, and G. Meier, *Influence of Dipolar Interaction on Vortex Dynamics in Arrays of Ferromagnetic Disks*, Physical Review Letters **105**, 037201 (2010).

[73] A. Puzic, B. Van Waeyenberge, K.W. Chou, P. Fischer, H. Stoll, G. Schutz, T. Tylliszczak, K. Rott, H. Bruckl, G. Reiss, I. Neudecker, T. Haug, M. Buess, and C.H. Back, *Spatially resolved ferromagnetic resonance: Imaging of ferromagnetic eigenmodes*, Journal of Applied Physics **97**, 10E704 (2005).

[74] L. Bocklage, B. Kruger, R. Eiselt, M. Bolte, P. Fischer, and G. Meier, *Time-resolved imaging of current-induced domain-wall oscillations*, Physical Review B **78**, 180405 (2008).

- [75] M. Donahue and D. Porter, OOMMF User's Guide, in: Interagency Report, National Institute of Standards and Technology, 1999.
- [76] S. Barman, A. Barman, and Y. Otani, *Controlled propagation of locally excited vortex dynamics in linear nanomagnet arrays*, Journal of Physics D-Applied Physics **43**, 335001 (2010).
- [77] S. Sugimoto, Y. Fukuma, S. Kasai, T. Kimura, A. Barman, and Y. Otani, *Dynamics of Coupled Vortices in a Pair of Ferromagnetic Disks*, Physical Review Letters **106**, 197203 (2011).
- [78] A. Barman, S. Barman, T. Kimura, Y. Fukuma, and Y. Otani, *Gyration mode splitting in magnetostatically coupled magnetic vortices in an array*, Journal of Physics D-Applied Physics **43**, 422001 (2010).
- [79] S. Barman, A. Barman, and Y. Otani, *Dynamics of 1-D Chains of Magnetic Vortices in Response to Local and Global Excitations*, Ieee Transactions on Magnetism **46**, 1342 (2010).
- [80] A. Vogel, T. Kamionka, M. Martens, A. Drews, K.W. Chou, T. Tyliczszak, H. Stoll, B. Van Waeyenberge, and G. Meier, *Coupled Vortex Oscillations in Spatially Separated Permalloy Squares*, Physical Review Letters **106**, 137201 (2011).

- [81] H. Jung, Y.-S. Yu, K.-S. Lee, M.-Y. Im, P. Fischer, L. Bocklage, A. Vogel, M. Bolte, G. Meier, and S.-K. Kim, *Observation of coupled vortex gyrations by 70-ps-time- and 20-nm-space-resolved full-field magnetic transmission soft x-ray microscopy*, Applied Physics Letters **97**, 222502 (2010).
- [82] S.T. Thornton and J.B. Marion, Classical dynamics of particles and systems, 5th ed., Brooks/Cole, Belmont, CA, 2004.
- [83] I.G. Main, Vibrations and waves in physics, 3rd ed., Cambridge University Press, Cambridge England ; New York, NY, USA, 1993.
- [84] S.C. Bloch, Introduction to classical and quantum harmonic oscillators, Wiley, New York, 1997.
- [85] K.-S. Lee, H. Jung, D.-S. Han, and S.-K. Kim, *Normal modes of coupled vortex gyration in two spatially separated magnetic nanodisks*, Journal of Applied Physics **110**, 113903 (2011).
- [86] W.K. Hiebert, A. Stankiewicz, and M.R. Freeman, *Direct observation of magnetic relaxation in a small permalloy disk by time-resolved scanning Kerr microscopy*, Physical Review Letters **79**, 1134 (1997).
- [87] T. Gerrits, J. Hohlfeld, O. Gielkens, K.J. Veenstra, K. Bal, T. Rasing,

and H.A.M. van den Berg, *Magnetization dynamics in NiFe thin films induced by short in-plane magnetic field pulses*, Journal of Applied Physics **89**, 7648 (2001).

[88] G.M. Sandler, H.N. Bertram, T.J. Silva, and T.M. Crawford, *Determination of the magnetic damping constant in NiFe films*, Journal of Applied Physics **85**, 5080 (1999).

[89] M. Curcic, B. Van Waeyenberge, A. Vansteenkiste, M. Weigand, V. Sackmann, H. Stoll, M. Fähnle, T. Tyliczszak, G. Woltersdorf, C.H. Back, and G. Schütz, *Polarization Selective Magnetic Vortex Dynamics and Core Reversal in Rotating Magnetic Fields*, Physical Review Letters **101**, 197204 (2008).

[90] Y.S. Yu, H. Jung, K.S. Lee, P. Fischer, and S.K. Kim, *Memory-bit selection and recording by rotating fields in vortex-core cross-point architecture*, Applied Physics Letters **98**, 052507 (2011).

[91] M. Weigand, B. Van Waeyenberge, A. Vansteenkiste, M. Curcic, V. Sackmann, H. Stoll, T. Tyliczszak, K. Kaznatcheev, D. Bertwistle, G. Woltersdorf, C.H. Back, and G. Schutz, *Vortex Core Switching by Coherent Excitation with Single In-Plane Magnetic Field Pulses*, Physical Review Letters **102**, 077201 (2009).

- [92] C.S. Liu, C.K.A. Mewes, M. Chshiev, T. Mewes, and W.H. Butler, *Origin of low Gilbert damping in half metals*, Applied Physics Letters **95**, 022509 (2009).
- [93] S. Mizukami, D. Watanabe, M. Oogane, Y. Ando, Y. Miura, M. Shirai, and T. Miyazaki, *Low damping constant for Co<sub>2</sub>FeAl Heusler alloy films and its correlation with density of states*, Journal of Applied Physics **105**, 07D306 (2009).
- [94] International Technology Roadmap for Semiconductors, 2009 edition, in, Semiconductor Industry Assoc., <http://public.itrs.net>, 2009.
- [95] R.W. Keyes, *Physical Limits in Semiconductor Electronics*, Science **195**, 1230 (1977).
- [96] R.P. Cowburn and M.E. Welland, *Room temperature magnetic quantum cellular automata*, Science **287**, 1466 (2000).
- [97] A. Imre, G. Csaba, L. Ji, A. Orlov, G.H. Bernstein, and W. Porod, *Majority logic gate for magnetic quantum-dot cellular automata*, Science **311**, 205 (2006).
- [98] G. Csaba, A. Imre, G.H. Bernstein, W. Porod, and V. Metlushko, *Nanocomputing by field-coupled nanomagnets*, Ieee Transactions on

Nanotechnology **1**, 209 (2002).

[99] S.R. Bowden and U.J. Gibson, *Optical Characterization of All-Magnetic NOT Gate Operation in Vortex Rings*, Ieee Transactions on Magnetism **45**, 5326 (2009).

[100] H. Jung, K.S. Lee, D.E. Jeong, Y.S. Choi, Y.S. Yu, D.S. Han, A. Vogel, L. Bocklage, G. Meier, M.Y. Im, P. Fischer, and S.K. Kim, *Tunable negligible-loss energy transfer between dipolar-coupled magnetic disks by stimulated vortex gyration*, Scientific Reports **1**, 59 (2011).

[101] K.-S. Lee, K. Guslienko, J.-Y. Lee, and S.-K. Kim, *Ultrafast vortex-core reversal dynamics in ferromagnetic nanodots*, Physical Review B **76**, 174410 (2007).

[102] K.L. Metlov and K.Y. Guslienko, *Stability of magnetic vortex in soft magnetic nano-sized circular cylinder*, Journal of Magnetism and Magnetic Materials **242–245, Part 2**, 1015 (2002).

[103] K.W. Chou, A. Puzic, H. Stoll, G. Schutz, B. Van Waeyenberge, T. Tylliszczak, K. Rott, G. Reiss, H. Bruckl, I. Neudecker, D. Weiss, and C.H. Back, *Vortex dynamics in coupled ferromagnetic multilayer structures*, Journal of Applied Physics **99**, 08F305 (2006).



- [104] K. Nakano, D. Chiba, K. Sekiguchi, S. Kasai, N. Ohshima, K. Kobayashi, and T. Ono, *Electrical Detection of Vortex Core Polarity in Ferromagnetic Disk*, Applied Physics Express **3**, 053001 (2010).
- [105] K. Nakano, D. Chiba, N. Ohshima, S. Kasai, T. Sato, Y. Nakatani, K. Sekiguchi, K. Kobayashi, and T. Ono, *All-electrical operation of magnetic vortex core memory cell*, Applied Physics Letters **99**, 262505 (2011).
- [106] J. Ohe, S.E. Barnes, H.W. Lee, and S. Maekawa, *Electrical measurements of the polarization in a moving magnetic vortex*, Applied Physics Letters **95**, 123110 (2009).

## Publication List

1	<p><b><u>H. Jung</u></b>, K.-S. Lee, D.-E. Jeong, Y.-S. Choi, Y.-S. Yu, D.-S. Han, A. Vogel, L. Bocklage, G. Meier, M.-Y. Im, P. Fischer and S.-K. Kim, Scientific Reports (Nature Publishing Group) <b>1</b>, 59; DOI:10.1038/srep00059 (2011).</p> <p>“Tunable negligible-loss energy transfer between dipolar-coupled magnetic disks by stimulated vortex gyration”</p>
2	<p><b><u>H. Jung</u></b>, Y.-S. Choi, K.-S. Lee, D.-S. Han, Y.-S. Yu, M.-Y. Im, P. Fischer, ACS Nano, <b>6</b>, 3712 (2012).</p> <p>“Logic Operations Based on Magnetic-Vortex-State Networks”</p>
3	<p><b><u>H. Jung</u></b>, Y.-S. Yu, K.-S. Lee, M.-Y. Im, P. Fischer, L. Bocklage, A. Vogel, M. Bolte, G. Meier, and S.-K. Kim, Appl. Phys. Lett. <b>97</b>, 222502 (2010).</p> <p>“Observation of coupled vortex gyrations by 70-ps-time- and 20-nm-spaceresolved full-field magnetic transmission soft x-ray microscopy”</p>
4	<p>K.-S. Lee, <b><u>H. Jung</u></b>, D.-S. Han, S.-K. Kim, J. Appl. Phys. <b>110</b>, 113903 (2011).</p> <p>“Normal modes of coupled vortex gyration in two spatially separated magnetic nanodisks”</p>
5	<p>Y.-S. Yu, K.-S. Lee, <b><u>H. Jung</u></b>, Y.-S. Choi, M.-W. Yoo, D.-S. Han, M.-Y. Im, P. Fischer, and S.-K. Kim, Phys. Rev. B. <b>83</b>, 174429 (2011).</p> <p>“Polarization-selective vortex-core switching by tailored orthogonal Gaussian-pulse currents”</p>

6	<p>Y.-S. Yu, <b>H. Jung</b>, K.-S. Lee, P. Fischer, and S.-K. Kim, Appl. Phys. Lett. <b>98</b>, 052507 (2011).</p> <p>“Memory-bit selection and recording by rotating fields in vortex-core cross-point architecture”</p>
7	<p>Y.-S. Choi, M.-W. Yoo, K.-S. Lee, Y.-S. Yu, <b>H. Jung</b>, and S.-K. Kim, Appl. Phys. Lett. <b>96</b>, 072507 (2010).</p> <p>“Out-of-plane current controlled switching of the fourfold degenerate state of a magnetic vortex in soft magnetic nanodots”</p>
8	<p>K.-S. Lee, S.-K. Kim, Y.-S. Yu, Y.-S. Choi, K. Yu. Guslienko, <b>H. Jung</b>, and P. Fischer, Phys. Rev. Lett. <b>101</b>, 267206 (2008).</p> <p>“Universal criterion and phase diagram for switching a magnetic vortex core in soft magnetic nanodots”</p>

## Patent List

1	<p>S.-K. Kim, <b>H. Jung</b>, Y.-S. Yu, and K.-S. Lee</p> <p>“Magnetic head for magnetic recording medium using magnetic vortex”</p> <p>“자기소용돌이를 이용한 자기기록매체의 자기헤드”</p> <p>Korean Patent No. 10-0931582 (Dec. 4, 2009).</p>
---	--

## Presentations in Conferences

### International Conference

1	<p>[2012] The 19<sup>th</sup> International Conference on Magnetism (ICM 2012), Busan, Korea, July 8-13,2012.</p> <p><b><u>H.Jung</u></b>, Y.-S. Choi, D.-S. Han, Y.-S. Yu, K.-S. Lee, M.-Y. Im, P. Fischer, S.-K. Kim.</p> <p>“Logic Operations Based on Magnetic-Vortex-State Networks”</p>
2	<p>[2011] 55<sup>th</sup> Annual Conference on Magnetism &amp; Magnetic Materials (MMM 2011), Arizona, USA, Oct. 30 – Nov. 3, 2011.</p> <p><b><u>H. Jung</u></b>, K.-S. Lee, D.-E. Jeong, Y.-S. Choi, Y.-S. Yu, D.-S. Han, A. Vogel, L. Bocklage, G. Meier, M.-Y. Im, P. Fisher, and S.-K. Kim</p> <p>“Tunable negligible-loss energy transfer between dipolar-coupled magnetic disks by stimulated vortex”</p>
3	<p>[2011] 2<sup>nd</sup> International Workshop on Magnonics: From Fundamentals to Applications, Recife, Brazil, Aug. 7-10, 2011.</p> <p><b><u>H. Jung</u></b>, K.-S. Lee, D.-E. Jeong, Y.-S. Choi, Y.-S. Yu, D.-S. Han, A. Vogel, L. Bocklage, G. Meier, M.-Y. Im, P. Fisher, and S.-K. Kim</p> <p>"Energy transfer between vortex-state magnetic disks by stimulated vortex gyration"</p>

4	<p>[2010] International Conference of AUMS (ICAUMS 2010), Jeju Island, Korea, Dec. 5-8, 2010.</p> <p><b>H. Jung</b>, Y.-S. Yu, K.-S. Lee, A. Vogel, L. Bocklage, M. Bolte, G. Meier, M.-Y. Im, P. Fischer, and S.-K. Kim,</p> <p>"Time-resolved soft x-ray microscope study of dipolar-induced vortex gyrations in coupled vortex oscillators studied by a time-resolved soft x-ray microscope",</p>
5	<p>[2010] 55<sup>th</sup> Annual Conference on Magnetism &amp; Magnetic Materials (MMM 2010), Atlanta, USA, Nov. 14 - 18, 2010.</p> <p><b>H. Jung</b>, S.-K. Kim, Y.-S. Yu, K.-S. Lee, L. Bocklage, A. Vogel, M. Bolte, G. Meier, M.-Y. Im, P. Fischer</p> <p>"Dipolar-induced vortex gyrations in coupled vortex oscillators studied by a time-resolved soft x-ray microscope"</p>
6	<p>[2010] 10<sup>th</sup> Joint MMM/Intermag Conference, Washington DC, USA, Jan. 18-22, 2010.</p> <p><b>H. Jung</b>, Y.-S. Yu, K.-S. Lee, M.-Y. Im, P. Fischer, M. Bolte, L. Bocklage, A. Vogel, G. Meier, S.-K. Kim</p> <p>"Dipolar-interaction induced vortex gyrations in coupled vortex oscillators"</p>
7	<p>[2008] Asian Magnetism Conference 2008 (AMC 2008), Busan, South Korea, Dec. 10-13, 2008.</p> <p><b>H. Jung</b>, K.-S. Lee, Y.-S. Yu, and S.-K. Kim</p> <p>"Magnetic Vortex Excitations in Dipolar-coupled Magnetic Nanodots",</p>

## Domestic Conference

1	<p>[2012] 한국자기학회 2012년도 임시총회 및 하계학술연구발표회, 대전, May. 24 - 25, 2012.</p> <p><b>정현성</b>, 최윤석, 한동수, 유영상, 이기석, 임미영, Peter Fischer, 김상국</p> <p>“자기소용돌이 배열을 이용한 XOR 논리연산의 실험적 구현”</p>
2	<p>[2011] 한국자기학회 2011년도 임시총회 및 하계학술연구발표회, 천안, Jun. 9 - 11, 2011.</p> <p><b>H. Jung</b>, K.-S. Lee, D.-E. Jeong, Y.-S. Choi, Y.-S. Yu, D.-S. Han, A. Vogel, L. Bocklage, G. Meier, M.-Y. Im, P. Fisher, and S.-K. Kim</p> <p>“Energy transfer between dipolar-coupled magnetic disks by stimulated vortex gyration”</p>
3	<p>[2010] 한국자기학회 2010년도 임시총회 및 하계학술연구발표회, 원주, Jun. 10 - 12, 2010.</p> <p><b>H. Jung</b>, Y.-S. Yu, K.-S. Lee, A. Vogel, L. Bocklage, M. Bolte, G. Meier, M.-Y. Im, P. Fischer, and S.-K. Kim</p> <p>“Soft x-ray microscopy observation of dipolar-interaction induced magnetic-vortex gyration”</p>